CHARACTERIZATION AND REACTION STUDIES OF SILICA SUPPORTED PLATINUM AND RHODIUM MODEL CATALYSTS

A Dissertation

by

MATTHEW JAMES LUNDWALL

Submitted to the Office of Graduate Studies of
Texas A&M University
in partial fulfillment of the requirements for the degree of

DOCTOR OF PHILOSOPHY

December 2010

Major Subject: Chemistry

Characterization and Reaction Studies of Silica Supported Platinum and Rhodium Model Catalysts

CHARACTERIZATION AND REACTION STUDIES OF SILICA SUPPORTED PLATINUM AND RHODIUM MODEL CATALYSTS

A Dissertation

by

MATTHEW JAMES LUNDWALL

Submitted to the Office of Graduate Studies of
Texas A&M University
in partial fulfillment of the requirements for the degree of

DOCTOR OF PHILOSOPHY

Approved by:

Chair of Committee,	D. Wayne Goodman
Committee Members,	James D. Batteas
	Manuel P. Soriaga
	Daniel F. Shantz
Head of Department,	David H. Russell

December 2010

Major Subject: Chemistry

ABSTRACT

Characterization and Reaction Studies of Silica Supported Platinum and Rhodium Model Catalysts. (December 2010)

Matthew James Lundwall, B.S., State University of New York at Stony Brook

Chair of Advisory Committee: Dr. D. Wayne Goodman

The physical and catalytic properties of silica supported platinum or rhodium model catalysts are studied under both ultra high vacuum (UHV) and elevated pressure reaction conditions (>1torr). Platinum or rhodium nanoparticles are vapor deposited onto a SiO_2/Mo(112) surface and characterized using various surface analytical methods. CO chemisorption is utilized as a surface probe to estimate the concentration of various sites on the nanoparticles through thermal desorption spectroscopy (TDS) and infrared reflection absorption spectroscopy (IRAS) along with microscopy techniques to estimate particle size. The results are compared with hard sphere models of face centered cubic metals described as truncated cubo-octahedron. Results demonstrate the excellent agreement between chemisorption and hard sphere models in estimating the concentration of undercoordinated atoms on the nanoparticle surface. Surfaces are then subjected to high pressure reaction conditions to test the efficacy of utilizing the rate of a chemical reaction to obtain structural information about the surface. The surfaces are translated in-situ to a high pressure reaction cell where both structure insensitive and sensitive reactions are performed. Structure insensitive reactions (e.g. CO oxidation)

allow a method to calculate the total active area on a per atom basis for silica supported platinum and rhodium model catalysts under reaction conditions. While structure sensitive reactions allow an estimate of the types of reaction sites, such as step sites ($\leq C_7$) under reaction conditions (e.g. n-heptane dehydrocyclization). High pressure structure sensitive reactions (e.g. ethylene hydroformylation) are also shown to drastically alter the morphology of the surface by dispersing nanoparticles leading to inhibition of catalytic pathways. Moreover, the relationships between high index single crystals, oxide supported nanoparticles, and high surface area technical catalysts are established. Overall, the results demonstrate the utility of model catalysts in understanding the structure-activity relationships in heterogeneous catalytic reactions and the usefulness of high pressure reactions as an analytical probe of surface morphology.

DEDICATION

To my mother, who always wished I would put more effort into my studies.

To my father, who inspired me to question my surroundings.

To my wife, whose love and support have made this dissertation possible.

ACKNOWLEDGEMENTS

Graduate school has been an extremely rewarding experience. I have learned more about chemistry in my first year as a graduate student than in all my years as an undergraduate. I can honestly say I am a different person than I was 5 years ago. I have met many people during this time who have not only provided me guidance but who have also helped me achieve my true potential. I am therefore indebted to them and only hope my future success is enough to satisfy a partial payment.

I first and foremost would like to thank my committee chair and advisor, Dr. D. Wayne Goodman, whose enthusiasm and dedication towards science is unmatched. Dr. Goodman has not only taught me *about* science but has taught me how to *do* science. He has been extremely professional, kind hearted, and sharp as a razors edge; qualities everyone of his student hopes to inherit upon graduation. I would also like to thank my committee members, Dr. James D. Batteas, Dr. Manuel P. Soriaga, and Dr. Daniel F. Shantz, for their guidance throughout the course of my graduate studies.

I would like to thank my research associate, Dr. Sean M. McClure, who has been an integral part of my research experiences. Dr. McClure has worked with me on every aspect of the research presented in this dissertation and has become a good friend of mine during this time.

I would also like to thank fellow co-workers Dr. Ming-shu Chen for his innovative ideas, Dr. Tao Wei for training me, Dr. Zhen Yan for his insight, and Dr. Sungsik Lee, Dr. Kerrie Gath, Dr. Yun Cai, Dr. Fan Yang, Dr. Patrick Han, Dr.

Stephanus Axnanda, Dr. Feng Gao, Zhoujun Wang, Zihao Zhou, and Elad Gross for their help and support.

A special thanks to my mother and father, my brother and sister, and my wife for their love and encouragement. Without them, my journey through graduate school would not have been possible. Finally, thanks to my friends and colleagues and the department faculty and staff for making my time at Texas A&M University a great experience.

TABLE OF CONTENTS

LIST OF FIGURES

FIGURE Page

FIGURE Page

FIGURE Page

LIST OF TABLES

CHAPTER I

INTRODUCTION

Model Heterogeneous Catalysts

Fundamental study of heterogeneous catalysts is important from both an economic and academic standpoint. This is because heterogeneous catalysts are used heavily in the refining industry but their chemistry is not well understood. By definition, a catalyst can be described as a substance that increases the rate at which a chemical reaction approaches equilibrium and does not itself undergo a net chemical change.[1] When a catalyst is in a different phase (e.g. solid) than a reactant mixture it is defined as a heterogeneous catalyst.

Two types of heterogeneous catalysts are real-world and model catalysts. The designation of "real world" is used strictly when referring to high-surface-area catalysts created and used under the influence of economic demand. Real world catalysts utilize porous oxide materials, typically amorphous SiO_2 or Al_2O_3, which have a large surface area (>100 m^2g^{-1}) along with an inherent non-uniform structure.[2] Such materials are necessary from an economical standpoint as they allow the largest chemically active area per gram of catalyst. The active surface is typically comprised of highly dispersed transition metal clusters distributed throughout the internal and external areas of the support. Clusters are non-uniform and often exhibit a large size distribution. These

---

This dissertation follows the style of *Journal of Physical Chemistry C*.

clusters serve as the central point of activation and thus govern the reactivity and selectivity of heterogeneous catalysts.[2]

From an academic standpoint, understanding the structure activity relationships and reaction mechanisms of heterogeneous catalytic systems are necessary for answering the question "why". In general, a real-world-catalyst is prepared and reacted at high throughput, pressure, and temperature; an environment that is arguably far from ideal.[2-5] Most industrial research on high surface area supports has been conducted using a top-down approach, where catalysts are first created and screened in large quantities with various reactants. Catalysts which demonstrate desirable activity are further probed while non-working surfaces are tuned (e.g. catalyst deactivation through graphite (coke) formation at the surface can be controlled by perturbing the electronic structure with the addition of a second metal). Knowledge and experimental evidence of the initial adsorption step of a catalyzed reaction or the chemisorbed state and bonding characteristics which allows formation of an intermediate are difficult to acquire.[2,3,6] Therefore, many questions arise concerning the active-nature of the surface. For what reasons, on an atomic level, are surfaces capable of sustaining a reaction and others deactivate? What effect does particle size/structure have on activity and selectivity? Is this an electronic or geometric effect? In order to answer such questions a fundamental understanding of the gas/surface interface must first be obtained. This becomes especially important for analysis of structure sensitive reactions, reactions whose selectivity and activity depend on the geometric and/or electronic structure of the catalytically active particle. However, fundamental studies of catalytic reactions on real

world catalysts are complicated by mass transfer issues, distribution of particle sizes, and convolution of support effects. Additionally, these surfaces are not amenable to many "traditional" surface spectroscopies (see below). To combat these issues, academic researchers have often focused on developing well-defined model heterogeneous catalysts to allow fundamental insights into the adsorption behavior and structure activity relationships involved in catalytic reactions.[4,7-17]

Fundamental study of real-world catalysts requires the development of model systems in order to evaluate the principles governing their behavior. Model-catalysts are of low-surface-area and are prepared in a highly controlled manner (i.e. monitoring particle deposition and growth, and reacting in an ultra clean environment [4,7-17]). Model catalysts can either be a planar metal-single-crystal with a well defined surface orientation or metal clusters deposited on the surface of a characterized oxide support.[4,5,18,19] These surfaces are amenable to traditional surface characterization such as ion scattering spectroscopy, electron energy loss spectroscopy, scanning tunneling microscopy, etc. Such model surfaces can be prepared by various techniques, such as solution-based methods[20,21] or vapor deposition techniques[22-29]. Model catalyst surfaces prepared by vapor deposition methods under ultra high vacuum (UHV) conditions, allow for creation of planar oxide films decorated by metal nanoparticles in an ultra clean environment as opposed to solution based methods which deposit metal precursor contaminants from preparation (e.g. chlorine). These types of vapor deposited surfaces can then be used to examine surface phenomena under controlled reaction conditions (e.g. vacuum). Indeed, a model-catalyst system allows an

ideal environment for a particular chemical reaction. The goal in examining such systems is to obtain answers to the questions discussed above. Such answers will ultimately help in the *design* of new heterogeneous catalysts.

As we begin to employ such surfaces to study complicated reactions at elevated pressures, it is important to further our understanding as to the extent of quantitative and qualitative agreement between measurements obtained from model systems and measurements obtained on single crystal and technical catalyst (high surface area) samples under similar elevated pressures. A complicating effect of understanding the structure-activity relationships of heterogeneous catalytic reactions at ambient pressures (near 1 atm or above) is the known ability of reactant gas environments to alter the morphology, particle dispersion, and even the types of adsorbates present on certain supported nanoparticle systems.[30-33] Developing an understanding of how such factors can affect the catalytic properties of supported nanoparticles is important from a fundamental surface chemistry perspective. Characterization of catalyst surfaces is an important component of this process and requires a detailed study of system parameters (e.g., particle size, number of active sites). For example, turnover frequency (TOF, product molecules produced/site/sec) is a standard metric used for comparison of reactivity data; its' accurate determination is dependent on an accurate estimation of the total number of reactive sites available for reaction on the catalyst surface.[30] Similarly, it is important to understand whether site characterization methods which are generally conducted under UHV conditions on such samples (e.g. CO TPD, STM), are in general correlation with reactivity measurements under elevated pressure conditions.

In the introductory sections to follow, model catalyst systems of both single crystal and supported nanoparticles are discussed in terms of their structure. These various structures give rise to two different reaction mechanisms (i) structure insensitive and (ii) structure sensitive, during heterogeneous catalytic reactions. Three different reactions which follow one these mechanisms are introduced and a hypothesis is established on the applicability of such reactions for establishing surface properties from quantitative estimates under high pressure reaction conditions.

Single Crystals

The structure of crystals is an important property which governs the behavior of solid state materials. One of the best known techniques for determining this property has been x-ray diffraction (XRD) which utilizes the constructive interference of scattered x-rays to produce a diffraction pattern which is indicative of the bulk crystal structure. The structure of pure metals such as Pt, Rh, Mo used in this thesis have been determined in this manner and their structure can be described by a hard sphere model of the cubic crystal system. Three cubic crystal structures, namely simple cubic (SC), body centered cubic (BCC), and face centered cubic (FCC) are known.[2,3] Here, discussion of only FCC (for Pt, Rh) and BCC (Mo) are necessary. Atoms in these structures can be packed in a few orientations. The two types of FCC closest packing of hard spheres are cubic close packing (c.c.p.) and hexagonal close packed (h.c.p.) while BCC represents and open structure. For example, c.c.p. and h.c.p. occupy a volume element with an atomic packing factor of 0.74 while that of BCC is 0.68(i.e. c.c.p and h.c.p. pack more tightly than BCC). The packing of these three types are listed in **Figure 1**. As can be seen, the

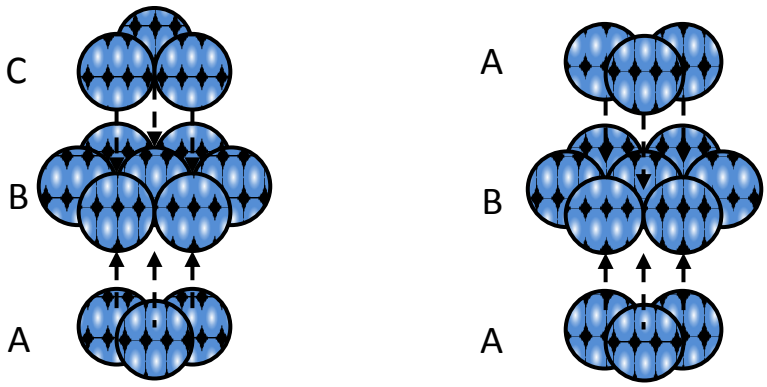

Cubic Close Packing (ccp) Hexagonal Close Packing (hcp)

Figure 1. Cubic and hexagonal close packed structures.

c.c.p crystal packs in ABC, while h.c.p. packs in ABA fashion. Atoms in FCC bulk crystals have 12-fold coordination while BCC has 8-fold coordination.

The surface-orientation of the cubic structures can vary dramatically depending on which crystallographic plane the surface is cut against. After alignment of the bulk structure using XRD the crystal can be polished using a series of abrasive colloid solutions to achieve an atomically flat mirror finish. The orientation of the surface can be determined using low energy electron diffraction (LEED), a technique which uses electrons in the energy range of 100eV and have a wavelength on the order of an atomic lattice spacing (i.e. 0.1nm).[2,3] Surfaces prepared in this manner have a well-defined surface structure and an atomic concentration of approximately 10^{15}atoms/cm^2.[2,3] The crystal is typically described using miller index notation, which describes the bulk or surface in reference to planes and directions in a basis set.[1,2,3] However, surface structure can differ substantially from that predicted by the bulk crystal orientation. For example, silicon cut along the [100] direction can exhibit a (1x2) missing row structure due to minimization of the surface free energy by surface-reconstruction.[34] This effect is also known to occur for many (100) and (110) surface structures.[2,3]

The main surface orientations used for fundamental science on FCC metals has been (111), (100), and (110) as depicted in **Figure 2**. These surfaces are considered low-index surfaces do to their low miller index values. The thermodynamic stability of these surface decrease in the following order: (111), (100), (110).[2,3] Each of these surfaces has a different work function with a trend that decreases in the following order (110), (100), and (111).[2,3] This trend follows the maximum coordination of surface atoms (i.e. atoms

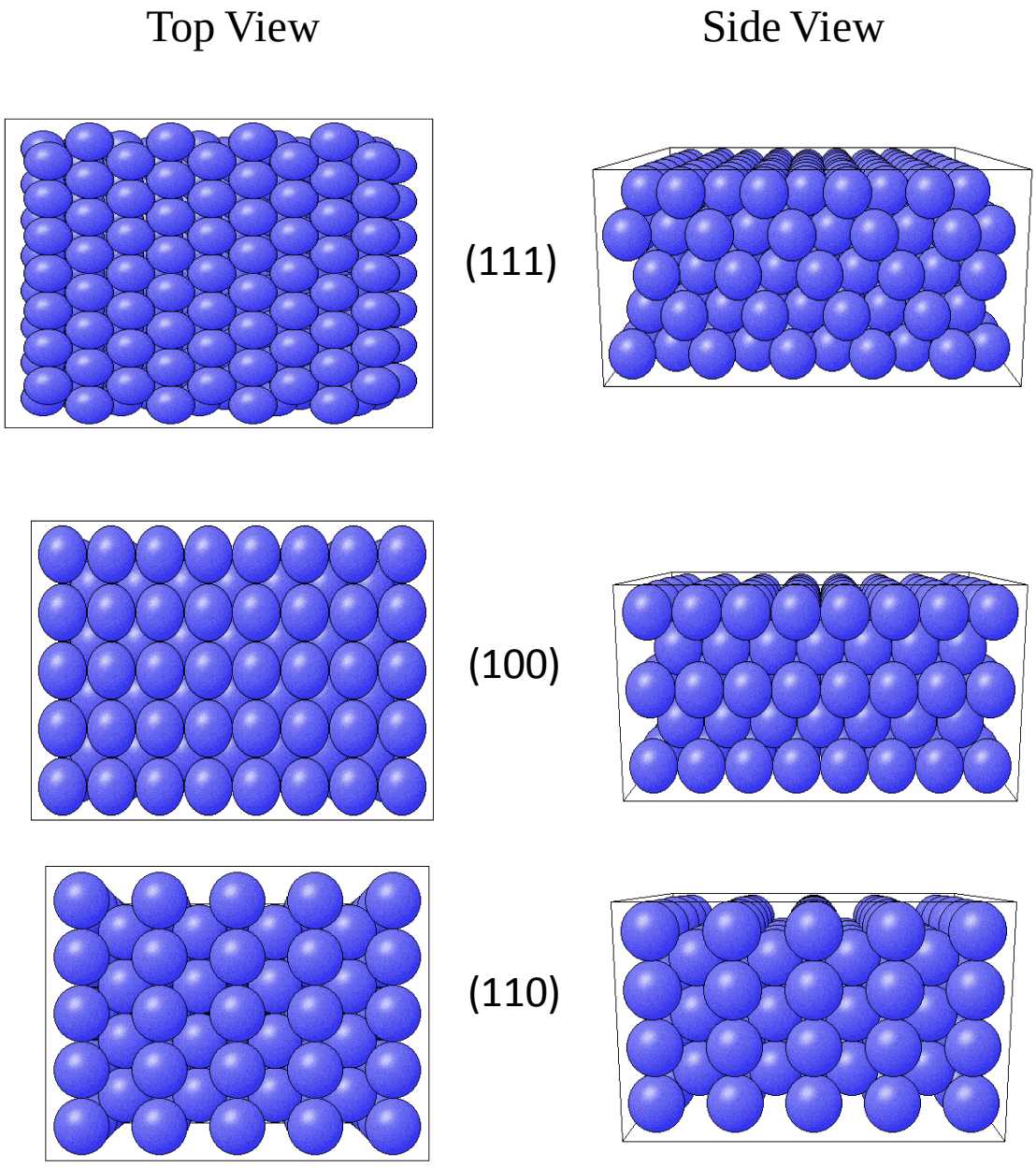

Figure 2. Low index single crystals.

on a FCC(111) surface have 9-fold coordination, an FCC(100) has 8-fold, and FCC(110) has 7-fold).

The differences in electronic structure at the surface of the low index surface results in a different degree of interaction with adsorbate molecules. Photoemission spectroscopy and vibrational spectroscopy measurements on the surface covered with various molecules have been conducted.[6] Depending on the bonding geometry of the adsorbate with the surface or the surface orientation the amount of back donation can be dramatically affected. For example, CO or NO adsorption on Pt-group metals will exhibit vibrational energy shifts depending on the available electron density at the surface.[6] Adsorption at undercoordinated surface atoms tends to reduce the vibrational energy due to an increased back donation of electron density. This result mirrors the change in electron density when comparing with the work function of the various surface orientations. Also, the geometry of a particular adsorption-site-ensemble can also have an effect where matching between the surface lattice spacing and bond length are necessary for dissociating molecules (e.g. ethane on nickel surfaces[35]).

Cutting low-index single crystals such as (111), (110), and (100) greater than one degree off the crystal plane gives rise to highly corrugated surfaces with complex miller indices such as (112), (335) etc. **Figure 3**.[36] These surfaces are deemed vicinal or high-index surfaces. The main change in the surface structure is the concentration of under-coordinated atoms and the width of the terraces. For example, a (112) surface of an FCC metal has both 9-fold and 7-fold coordinated atoms at the surface with a terrace width of 3 atoms wide (see **Figure 3**). These type of surfaces have been paramount in

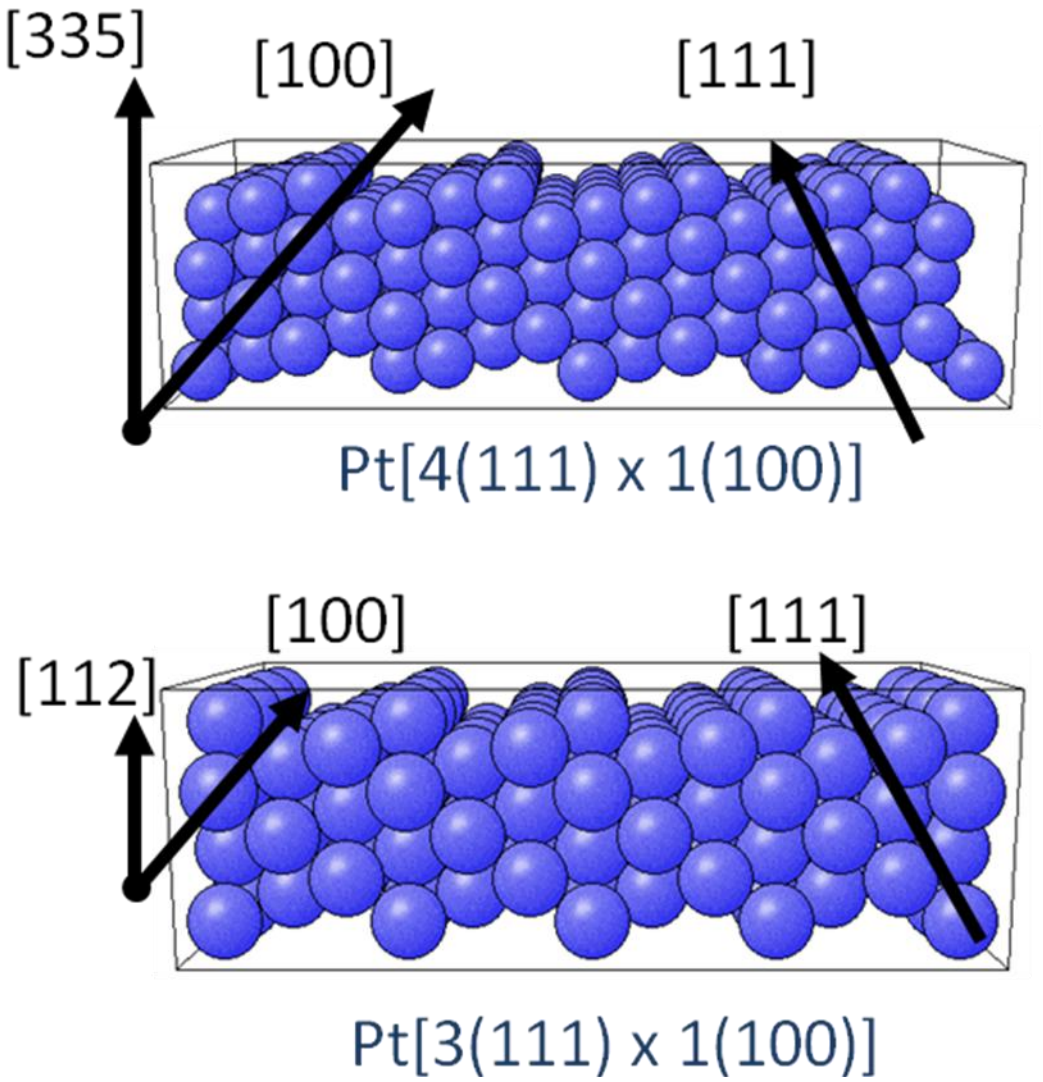

Figure 3. High index single crystals. Structures are also listed in step terrace notation.

fundamental investigations of the influence under-coordinated atoms have in heterogeneous catalysis. For example, hydrogen-deuterium exchange reactions[37], oxygen dissociation[38-41], NO and CO adsorption and dissociation[42,43], nitrogen dissociation[44], and dissociative chemisorption of unsaturated and saturated hydrocarbons[45] to name a few. Such systems have been studied under low and high pressures. A driving force behind studying high index single crystals is their similarity to surface atoms found on nanoparticles typically used in heterogeneous industrial catalysts. High index crystal planes (112, 335, 321, etc.) offer a high density of defects (steps, kinks, and corner atoms)[36], structural features which represent the largest percentage of available sites on dispersed metal catalysts and have therefore been of central importance for fundamental studies.

Insights gained from both low and high index single crystals are numerous, however these systems do not accurately model the electronic/size or substrate effects that may influence adsorption on dispersed-particle catalysts typically used in real world catalysts, the so called "material-gap".[4,9,13] Therefore, well-defined nanoparticle systems must be grown and characterized to help better understand the complex interplay between support-particle interactions.

Supported Nanoparticles

It has been established that the growth mode of nanoparticles is controlled by the inherent properties of its constituents and also by the surrounding environment (e.g metal, support, temp etc.).[46] These parameters govern the size, shape, and therefore the proportions of different facets on their surfaces. For the purpose of preparing metal

nanoparticles for fundamental studies in heterogeneous catalysis, vapor deposition in UHV is clearly at an advantage for three main reasons (i) nanoparticles are created in an ultra-clean environment which eliminates the use of contaminating ligands from metal precursors (ii) the ability to apply the full complement of surface analytical techniques *in-situ* (iii) the ability to avoid mass transfer limitations of reactants through the support as all particles lie on the surface of the substrate.

Vapor deposition of metal atoms on a substrate is typically achieved by heating a pure metal sample until approximately 2/3 of the melting point where atoms then begin to sublime into vacuum with energy kT. Atoms arrive at the surface of the substrate at rate defined by [46, 47]:

$$J = \frac{P}{\sqrt{2\pi mkT}}$$

where P is the pressure defined by the amount of atoms in the vacuum between the sample and source, m is the atomic mass, k is the Boltzmann constant, and T is the absolute temperature of the source. The atoms land on the surface with an adsorption residence time of [46,47]:

$$\tau_a^{-1} = \upsilon_a e^{-E_a/kT}$$

where υ is an atomic vibration on the order of 10^{13}Hz. At modest temperatures the atoms, or more formally, adatoms, will remain on the surface and migrate in two dimensions across the surface with diffusion constant defined by [46,47]:

$$D = \frac{\upsilon_d a^2}{4}\, e^{-E_{d/kT}}$$

where E_d is the diffusion energy, υ_d is the frequency, and {a} is the jump distance (0.2-0.5nm). The rms displacement of the adatom from the site which it lands before evaporation is therefore:

$$x = \sqrt{D\tau_a} \simeq a\sqrt{\frac{\upsilon_d}{\upsilon_a}}e^{(E_a - E_d)/2kT}$$

Since it is assumed that the adsorption energy is much greater than the diffusion energy, (x/a) is large at relatively low temperatures[46]. As the number density of adatoms increases the probability of nucleation increases where the free energy of formation for the bulk condensed phase and critical cluster size are centrally important in defining initial growth.[2,3,46] Three dimensional clusters will grow if the adatom and interfacial energy γ_a and γ_i are greater than the surface free energy of the substrate γ_s.[2,3,46] This type of growth mode is known as Volmer-Weber.[48]

Van Hardeveld and Hartog (V&H)[49] have demonstrated with statistical methods that nanoparticles < 4 nm in diameter have the highest percentage of under-coordinated atoms at their surface as compared to those >4nm. These sites can be defined for numerous three-dimensional geometric structures which can have the FCC structure such as cube, octahedron, rhombic dodecahedron, and cubo-octahedron (see **Figure 4**). The symbol $C_j^{p,q,r,s,\cdots}$ is used where j corresponds to the coordination number and p,q,r,s, etc. to assigned serial numbers which allow one to differentiate between atoms which have the same coordination but differ in arrangement. Numbers p,q,r,s, etc. varies as a value equal to (z-j) where z is the serial number (i.e. 1 through 12) on the atom (see **Figure 5**). For example, atoms in an FCC crystal are12-fold coordinated and labeled 1

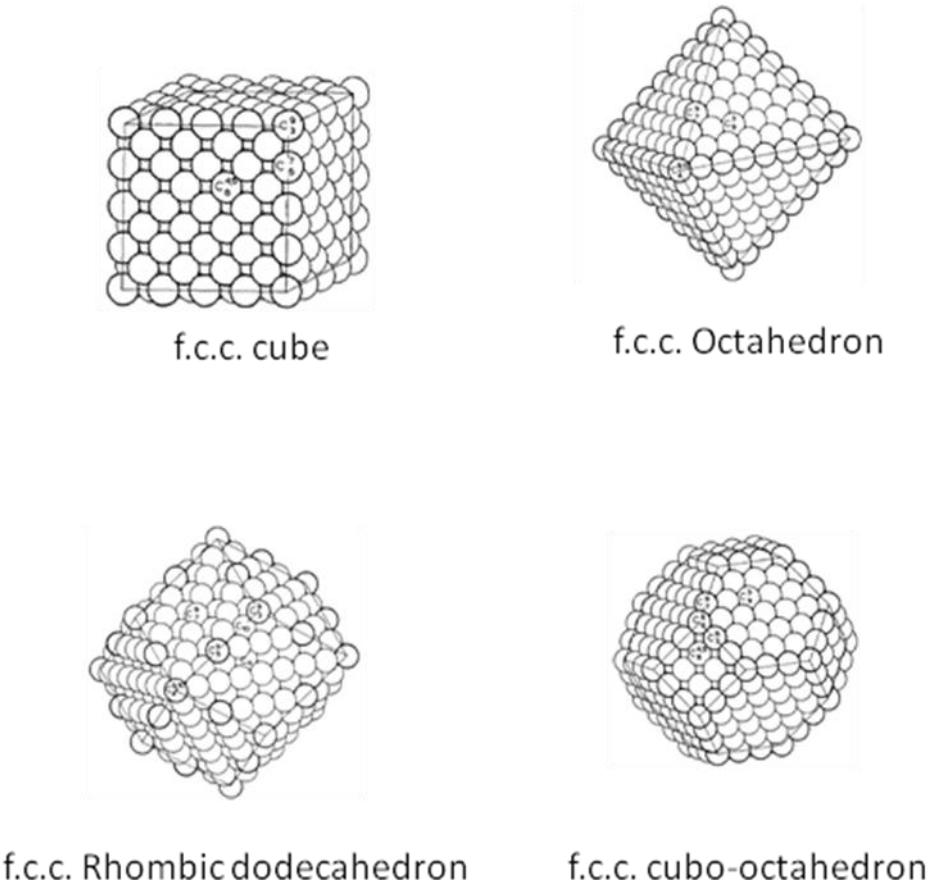

Figure 4. Geometric structures of face centered cubic clusters.[49]

through 12 but on a (111) surface an atom is 9-fold coordinated and therefore has lost atoms with serial numbers 1,2,and 3, so the designation is $C_9^{1,2,3}$, where by, omitting 1 and 2 by convention the designation is C_9^3. The combinations of labeled atoms that the FCC can be cut against to achieve 7-fold coordination is (1,2,3,4,5), (1,2,3,4,9), (1,2,3,5,6), (1,2,3,6,7), (1,2,3,7,8), and (1,2,3,8,9). As defined by V&H[49] the serial numbers, starting with 1, in the longest numerical order are in set (1,2,3,4,5) and (1,2,3,4,9). Here, by convention, only 5 and 9 are used as subscripts while the other sets are discarded as representing an identical result to either (1,2,3,4,5) or (1,2,3,4,9). The designation is therefore C_7^5 and C_7^9 respectively. This can be rationalized when viewing 7-fold coordination by cutting diagonally across either the (111) or the (100) crystal planes and eliminating either atoms (1,2,3,4,5) or (1,2,3,4,9) respectively (see **Figure 5**).

The diameter of the nanocrystal in the various shapes defined by the hard sphere model can be determined for an arbitrary atom size by using the dimensionless quantity d_{rel}, which can be defined as the ratio of the diameter of a sphere with a volume equal to N_T times the volume occupied by an atom in the unit cell, to the atom diameter d_{at}:

$$d_{rel} = \frac{d_{sph}}{d_{at}} = d_{at}^{-1} \sqrt[3]{\frac{6}{\pi} N_T \frac{V_u}{n_u}}$$

where V_u = volume of the unit cell, n_u= number of atoms in the unit cell. V_u is proportional to d_{at}^3, d_{rel} is only dependent on N_T and the lattice structure. For FCC and

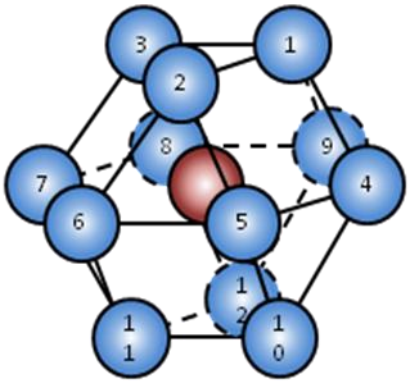

Cubic Close Packing (ccp)

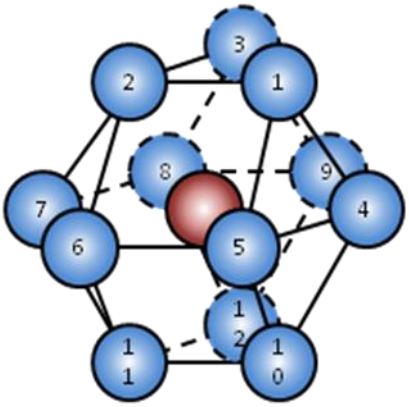

Hexagonal Close Packing(hcp)

Figure 5. Serial number assignment for c.c.p. and h.c.p. structures.

HCP, $d_{rel}= 1.105xN_T^{1/3}$ while for BCC $d_{rel} = 1.137xN_T^{1/3}$ where N_T is total surface atoms.[49]

As discussed in the previous section, high index single crystals have been utilized to mimic the surface structures of nanoparticles. Nanoparticle begin to exhibit macroscopic crystal plane early in their growth (see **Figure 6**). For a comparison, plotted in **Figure 7** is the percentage of terrace features on the surface of numerous stepped crystal planes on platinum. In this figure truncated cross-sections for both Pt(335) and Pt(112) are presented in step-terrace notation.[50-52] Following the designation by V&H[49], the step atoms have C^5_7 coordination in this model and can easily be distinguished (visually) from the C^3_9 and C_{10} sites. The C^5_7 atoms are 7-fold coordinated and terminate the (100) and (111) crystal planes. The C^3_9 surface sites are described as being 9-fold coordinated and exist in the (111) plane while the C_{10} sites have an additional atom, lie below the step edge, and are part of both the (111) and (100) crystal planes. The ratio of terrace-sites to total surface sites for this model is plotted against the terrace width in **Figure 7**. It can be seen as the width of the terrace increases, the total percentage of highly coordinated C^3_9 and C_{10} sites increases. Also presented in **Figure 7** are the approximate total $C^3_9 + C^{4,5}_8$ *terrace-like* sites that can exist on Pt NPs of different diameters; $C^{4,5}_8$ atoms have the highest coordination on a (100) surface. For this plot, a simple hard sphere counting model was used where NPs are described as truncated cubo-octahedron "caps", have a Pt atomic diameter of 0.28nm, and are truncated at a height equal to ½ the diameter (described in experimental section). This model is different from a "perfect" f.c.c cubo-octrahedron model as it bisects the cubo-octrahedron at a point

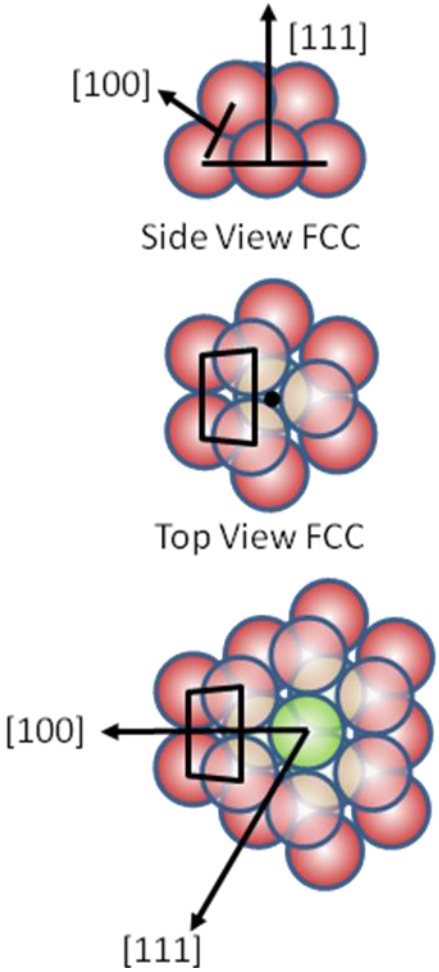

Figure 6. Initial crystal planes on f.c.c. nanoparticles.

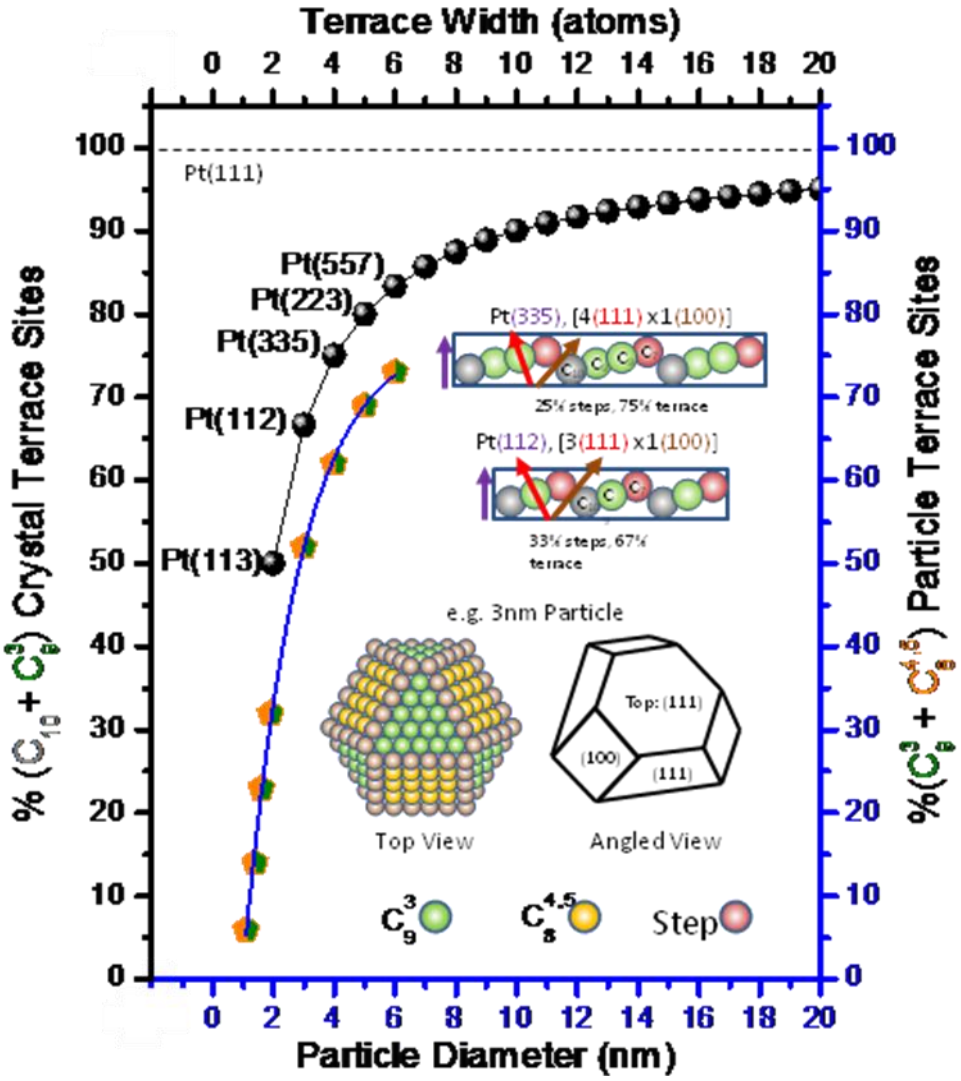

Figure 7. Comparison between high index single crystals and nanoparticles. Percentage of highly coordinated terrace sites (C_9 + C_{10}) on various stepped Pt single crystals plotted against the total terrace width. Insets are the truncated cross sections of Pt(335) and Pt(112), respectively, and indicate the (111) and (100) crystal orientations. Also plotted are the highly coordinated (C_9 + C_8) sites that are present of Pt nanoparticles of varied size. Nanoparticle statistics are obtained from a simple hard sphere counting model assuming Pt particles grow in the (111) orientation and can be described as truncated cubo-octahedron "caps". An example of a 3nm particle is presented in the figure.[53]

which gives 3 (100) facets (side), half of 3 (111) facets (side), and (111) facet (top) (see **Figure** 7). From the plot in **Figure 7** it can be seen that particles >4nm exhibit a percentage of *terrace-like* features (C^{3}_{9},$C^{4,5}_{8}$) that are in accordance with the (112) and (113) crystal planes (i.e. the local structure surrounding the (112) and (113) planes closely resembles that of small particles). CO desorption profiles on the (112) and (335) crystal planes *resemble* that of dispersed Pt catalysts.[51] An ideal unreconstructed (113)[52] crystal plane in this model has a qualitative particle size limit of 3 nm. As particles drop below <3 nm the percentage *terrace-like* features, C_9 and C_8, drop below 50% of the total surface area. As particle size continues to decreases, the *terrace-like* features asymptotically approach 0%. For this reason, it is essential to perform direct measurements on small Pt-particles since geometric arguments have no single crystal analog for particles <3 nm.

In heterogeneous catalysis the particle size is known to have a strong influence on the reactivity and selectivity of a catalyst. Particular features of interest on these systems are the under-coordinated atoms at the surface of the nanoparticle and the rapid change in concentration of these sites when the nanoparticle is varied between 1-4nm; as noted above. It is over this size regime that reaction rates and product distributions can change drastically. This chemical phenomenon has been related to both electronic and geometric changes as particles become smaller and the cooresponding binding energy changes at undercoordinated sites.[36] In many cases the effects are specific to the reactions conditions (temperatures and partial pressures).[54] Characterization studies of these supported nanoparticle systems have typically been achieved through theoretical

methods[55] or experiments performed under ultra-high vacuum conditions[56]. A general belief about applying theses methods is information obtained in this manner may not be relatable to phenomenon under high pressure reaction (>1torr) conditions due to changes in surface morphology (e.g. particle sintering). It is therefore necessary to apply analytical methods under such conditions to allow relationships between UHV and high pressure regimes to be established. However, such investigations in the literature are few due to the lack of inadequate experimental apparatus and resources. In the discussion section, high pressure reactions are conducted on platinum and rhodium nanoparticles in a unique experimental apparatus which allows information about morphology to be obtained from reaction rates and analytical spectroscopies.

Structure Insensitive vs. Sensitive Reactions

Chemical reactions which take place on the surface of solid state materials often exhibit changes in selectivity and activity which are indicative of the changes in surface morphology of the solid. For example, the activity of hydro-cracking catalysts will decrease as a result of carbon formation at the surface which blocks available reaction sites.[35,57-59] Moreover, loss of available reactions sites through sintering of metal nanoparticles at elevated reaction temperatures can also decreases the reaction rate. Product selectivity will concurrently be affected by the change in particular reaction-site-ensembles due to both processes above. It then becomes obvious that if the reaction rate can be accurately monitored one can utilize the results as a quantitative measure of surface properties *under reactions conditions*. The point here, *under reactions conditions*, is emphasized as few analytical techniques are available to study surface

processes under this condition. Typically, surface analysis is performed pre and post reaction which can lead to erroneous assumptions about active phases during reaction.

Two types of reactions which can be used as an analytical probe under reaction conditions are structure in-sensitive and structure sensitive reactions. Structure insensitive reactions are reactions in which the overall activity and selectivity are independent of the underlying crystal structure. Reactions which have demonstrated this effect on low index and high index single crystals of Pt-group metals have been CO oxidation[60] and ethylene hydrogenation.[61] However, structure in-sensitivity is highly specific to the conditions (i.e. temperature, partial pressures, total pressure) for both reactions and care must be taken in analyzing quantitative information achieved in this manner. For example, CO oxidation exhibits structure sensitive behavior at high oxygen partial pressures and temperatures due to oxide formation at the surface.[62] For ethylene hydrogenation, high temperatures and ethylene partial pressures results in polymerization or hydrogenolysis.[63] Therefore, a detailed analysis of conditions by which these reactions can be utilized must be achieved before the reaction rate can be used for quantitative assessment of the surface. In general, it is assumed by many in the surface science community that structure in-sensitive reactions can be applied in this manner but a comprehensive analysis for a particular nanoparticle system has yet to be completed.

Structure sensitive reactions are reaction in which the overall activity and selectivity are dependent on the underlying crystal structure. Most reactions exhibit this type of behavior. As with structure in-sensitive reactions, this type of reaction has also

been determined through the use of low index and high index single crystal samples demonstrating the utility of such surfaces. For example, hexane dehydrogenation on Pt(100) is more active then Pt(111).[64,65] The activity of these crystal faces have been used as a reference point in making assumptions about this type of reaction on Pt nanoparticles. As discussed below, in this type of reaction the orientation and interaction of the adsorbed molecule at the surface has a direct effect on the formation of reaction intermediate. The proposed mechanism can then be extended to Pt nanoparticles which exhibit (100) and (111) crystal planes.

In the following section 3 types of reactions will be discussed as potential probes of surface morphology under reaction conditions. The hypothesis will utilize results obtained on single crystal samples to help clarify results obtained on oxide supported metal nanoparticles (too be discussed). The results of which will demonstrate the applicability and usefulness of such experimental information.

CO Oxidation

Catalytic combustion of carbon monoxide is a well known reaction best recognized for its use in the catalytic converters of automobiles. The reaction is highly exothermic and is known to be structure insensitive on Pt-group metals single crystals and technical supported catalysts under CO dominant conditions (i.e. conditions where CO is in excess of the stoichiometric concentration[10,11,12,60]). Structure insensitive reactions are reactions which have the same rate on a per atom basis between different surface orientations.

Kinetic studies on Pt-group metal single crystal surfaces, under similar reaction conditions, have produced numerous insights into this reaction system.[60] These type of investigations have demonstrated that under elevated pressure conditions (pressures approaching 1 atm and CO-rich reaction conditions) and relevant catalytic temperatures (T = 450 – 625 K), the CO oxidation reaction on Rh (and Pd, Pt) exhibits structure insensitive behavior.[66-68] This view has been further validated by the good agreement of single crystal data with high surface area supported catalyst data.[66-70] Technical catalyst studies employing different size particles in the CO-inhibited regime, have also verified this structure insensitive behavior.[71] The results of which can be explained by the following. When a stoichiometric reaction mixture of CO and O_2 are added into a reactor a room temperature the surface is dominated by CO. Under steady state conditions CO adsorption and desorption are in equilibrium. As the surface temperature is raised CO begins to desorb allowing oxygen the opportunity to adsorb, dissociate, and react with CO to form CO_2. The elementary reaction steps are as follows:

$$CO_{(g)} \rightarrow CO_{(ads)}$$

$$CO_{(ads)} \rightarrow CO_{(g)}$$

$$O_{2(g)} \rightarrow 2O_{(ads)}$$

$$O_{(ads)} + CO_{(ads)} \rightarrow CO_{2(g)}$$

This is validated by the fact the activation energy of the reaction is approximately equal to the CO desorption energy (≈100kJ/mol) from the surface.[66-70] The reaction rate can then be expressed as:

$$r = k\,\theta_{co}\theta_{o}$$

where k is the rate constant and θ_{CO} is the θ_O are the surface coverage's of CO and O_2 respectively. This view agrees with the observed positive order dependence on O_2 pressure in the CO inhibited regime and the similarity of the observed reaction activation energy with the CO desorption activation energy. When the reaction is not under CO dominant conditions the concentration of oxygen at surface and thus the oxygen chemical potential can alter the surface morphology and change the composition of the surface layer; conditions which *may* form an oxide under reaction conditions.[72] This type of surface has been shown to be less active and to deviate from traditional LH kinetics. Under such conditions other mechanisms such as the Mars-van Krevelen have been proposed which discusses the reaction as a reduction of surface lattice oxygen.[73] In any event, if the reaction is truly structure insensitive under CO dominant conditions and obeys LH kinetics one should be able to use CO oxidation as a probe to calculate the surface area of exposed metal atoms on a Pt-group metal oxide supported catalyst; assuming a reference value can be established. However, this effect on supported nanoparticles has not been fully investigated. In the following discussion section, CO oxidation reactions on Pt and Rh single crystals and nanoparticles are run under CO dominant conditions. The results of which demonstrate the structure insensitive behavior of this reaction on Pt and Rh nanoparticles and its use as a probe of surface active sites.

Hydrocarbon Dehydrocyclization

The interaction of hydrocarbons with transition metals typically yields reactions which are structure sensitive. One particular structure sensitive reaction of both fundamental and industrial importance is the dehydrocyclization of aliphatic hydrocarbons by metallic platinum. The process involves reaction of the hydrocarbon on surface-sites which also favor cyclization, hydrogenolysis, and isomerization.[35,57-59] This reaction has roots in the petroleum refining industry where cyclization and branching are key to increasing the RON rating of gasoline.

Two particular dehydrocylization reactions conducted on platinum are n-heptane[59] and n-hexane[57] dehydrocylization. Studies using metallic single crystal have linked the coordination of atoms at steps and kinks sites to various types of reaction pathways in the reforming process. The reaction is conducted under large hydrogen partial pressures (zero order) during dehydrogenation process to rid the surface of carbonaceous build up from the competing hydrogenolysis reaction. Both n-heptane and n-hexane are believed to cyclize (i.e. to toluene and methylcyclopentane respectively) favorably on similar under-coordinated reaction sites, although, both products can also be formed are highly coordinated terrace sites $\geq C_8$. Gillespie et al.[59] has demonstrated the selectivity to be controlled by a combination of both terrace (e.g. C_9 coordination) and steps (e.g. C_7 coordination) sites. The reaction rate on stepped surfaces are shown to be more active by a factor two than flat surfaces with hexagonal structure Pt(111). Moreover, the rate has been shown to depend on terrace width. This is consistent with reactions of cyclohexene on platinum where terrace sites are important for

aromatization.[74] Dehydrocyclization is believed to first proceed through initial dehydrogenation, followed by cyclization, and then further dehydrogenation of the reaction intermediate. This mechanism can be inferred from cyclohexene dehydrogenation reactions known to form a 1,3-cyclohexatriene (MCT) intermediate on Pt(100) and both a 1,2 and 1,4 MCT on Pt(111).[64,65] Pt(111) is shown to be less active on account of the 1,4 CHT which is believed to block sites for the 1,3 CHT pathway. An intermediate for dehydrocyclization of n-heptane has not yet been observed. For dehydrocylization of n-heptane, the concentration of under-coordinated atoms at the surface of the single crystal is shown to increase the rate of toluene formation.[59] High index surfaces such as Pt(557) which has 7 atom wide (111) terraces and one atom high step sites of C_7 have a higher activity by a factor of 2 than a Pt(111).[59] Terrace width is also shown to be an important factor in the reactivity of the surface.

From the information above, it appears the dehydrocyclization reaction has the qualities of a probe reaction (i.e. the reaction can be utilized to obtain analytical information). Since the reaction rate varies as the morphology of the surface is varied, exploiting this effect may offer a way to obtain the concentration of undercoordinated atoms under high pressure reactions conditions on nanoparticle systems. This type of analysis will require accurate characterization of the surface. Such characterization can be obtained from both UHV analysis and high pressure structure insensitive reactions (CO Oxidation) as discussed in the previous section. To test the theory, the dehydrocyclization reaction will be conducted on Pt nanoparticles as a function of nanoparticle size. The data obtained from this type of analytical technique will

demonstrate the applicability of structure sensitive reactions for obtaining information under high pressure conditions.

Ethylene Hydroformylation

CO insertion into adsorbed alkyl groups (R-C_xH_y) to form oxygenates (such as alcohols or aldehydes) is an important reaction step in many heterogeneous catalytic reactions. For example, C_2H_4 hydroformylation (C_2H_4+CO+H_2) is a well-known reaction for the synthesis of aldehydes via the CO insertion reaction.[75] Insightful studies by Chuang and co-workers[76-79] and others[80,81] have investigated C_2H_4 hydroformylation on oxide supported Rh particles to gain information on the reaction mechanism and reactivity of various adsorbed CO surface species. It has been proposed that propionaldehyde production (CO insertion pathway) proceeds via hydrogenation of adsorbed C_2H_4 to form a surface ethyl species (R-C_2H_5), followed by insertion of adsorbed CO to form an acyl intermediate (R-C_2H_5CO), followed by hydrogenation to form propionaldehyde (C_2H_6CO).[76,77] Studies of propionaldehyde decomposition on Rh single crystal surfaces under UHV conditions, which produces H_2, CO, and ethyl species (along with surface C), also supports these general reaction steps.[82] Interestingly, surface coordination of adsorbed CO on Rh also appears to influence its reactivity for CO insertion reactions; for example, linear bound CO appears to be more reactive than CO bound to Rh in a dispersed and/or carbonyl state (e.g. gem-dicarbonyl $Rh(CO)_2$).[78,81]

Elevated pressure CO ambients have been shown to oxidatively disrupt and disperse Rh nanoparticles, creating highly dispersed gem-dicarbonyl species $Rh(CO)_2$ on oxide supports[33,34,83-85] (a process thought to be assisted by surface hydroxyl groups OH

[32,33,86]). Under elevated pressure (CO/H_2) and (CO_2/H_2) hydrogenation reaction conditions, Rh(CO)H carbonyl hydride species can also be formed.[87-90] The creation and stability of such carbonyl species ($Rh(CO)_2$, Rh(CO)H) can depend on particle size, gas pressure, and surface temperature. The cumulative effect of such factors could potentially have an important effect on the overall catalytic properties of the supported Rh NP surface, especially for catalytic reactions involving surface bound CO.

Thus, the C_2H_4+CO+H_2 system presents an interesting probe reaction to investigate a surface reaction (CO insertion into adsorbed R-C_2H_5 alkyl groups) whose surface morphology can all potentially depend on the initial Rh particle size and the reactant gas conditions. In the discussion section, the structure-activity relationships of the CO+C_2H_4+H_2 reaction on oxide supported Rh nanoparticle surfaces are investigated. The primary goal is to understand the structure-activity relationships of the CO insertion pathway during C_2H_4 hydroformylation and the role of elevated pressure reactant gas in altering the morphology and surface adsorbates present on supported Rh NPs.

CHAPTER II

EXPERIMENTAL

Ultra High Vacuum

This dissertation relies heavily on the use of an ultra high vacuum (UHV) chamber. Discussed below are some of the properties of the vacuum chamber to provide the reader adequate knowledge in the subject area and to introduce the terminology discussed throughout the dissertation. A brief description on how to achieve, measure, and maintain vacuum are indicated. However, the details of each component can and has encompassed several books by scientists in the literature. Additional detail beyond that listed below is beyond the scope of this dissertation and the reader should refer to references herein for further insight on the subject matter.

Table 1. Pressure Regimes.

Vaccuum Regime	**Pressure**	**Mean free path**
Low (rough) vacuum	atmospheric – 10^{-1} torr	64nm
Medium vacuum	10^{-1} – 10^{-2}torr	64μm
High vacuum (HV)	10^{-2} –10^{-7}torr	64mm
Ultra high vacuum (UHV)	10^{-7}– 10^{-11}torr	64m
Extreme high vacuum (XHV)	Less than 10^{-11}torr	640km

There are various levels of vacuum where molecules interact differently with the chamber walls and each other. The different flow regimes associated with these interactions can be assigned to a specific dimentionless quantity know as the Knudsen number Kn = λ/D where λ is the mean free path (defined below) and D is the diameter of the pipe which molecules flow through[47,91]:

$$\lambda = \frac{1}{\sqrt{2}n\pi d^2}$$

where n is the number density and d is the radius. Values for Kn >1 describe molecules moving in the molecular flow regime while <0.01 molecules move in a continuum flow regime. As indicated in **Table 1**, UHV can be defined as a pressure regime where molecules are in the molecular flow regime and exhibit ideal gas behavior. Under these conditions the mean free path of molecules are in the range of 64m. There are two purposes for using such a pressure regime (i) to allow the use of analyzers for detection of particles (e.g. electrons or ions) and (ii) allow a clean environment for defining surface properties by essentially eliminating ambient molecules i.e. H_2O , N_2, CO_2 etc.

The vacuum chamber used for experiments was designed and built by D.W. Goodman and co-workers at Texas A&M University back in the early 90's.[92] The vacuum chamber is approximately 60L and is constructed of 304 stainless steel plates where each joint has been welded with a helium arc welder from the inside. This type of material is typically used in UHV because of its usability (i.e. machining, high temperature durability, and non-magnetic behavior). The welding procedure ensures the lowest probability of virtual leaks (i.e. out-gassing from tiny crevices inside the chamber). The design utilizes conflat flanges around the perimeter of the system which

allows interchange and exchange of instrumentation and components for optimization of particular experiments. The conflat flanges are sealed with oxygen free high conductivity (OFHC) copper gaskets which can be replaced for each mounting. This gasket type allows a sharp pressure differential to be achieved at the knife edge of the conflat while maintaining high temperature durability. Systems using this method routinely achieve base pressures $<10^{-10}$torr. Additionally, the chamber consists of a hollow sample probe with copper electrical feed-throughs mounted internally. The probe can be translated vertically through stainless steel bellows using a basic electric motor. Vacuum is maintained under translation by the bellows which contract and expand along the vertical direction. The probe can also be rotated 360degress and translated horizontally several centimeters using a micometer to allow accurate and repeatable sample positioning. Vacuum under rotation is maintained by a differentially pumped telfon sliding seal.

The vacuum chamber utilizes two different types of vacuum pumps. The first pump is a commercial (e.g. Alcatel) rotary vane pump which is a type of positive displacement pump for achieving pressure down to 10^{-3}torr. This pump employs an internal cylindrical mounting chamber with a rotor that is mounted off center from the axis of rotation.[47,91] The rotor contains sliding vanes which push outward by a set of springs. The pump will rotate through a cycle in the following manner: pulling gas inward though induction ($K_n < 0.01$), isolation of the gas, compress of the gas, and finally to expel the gas through an exhaust port. The system is mounted in oil to provide lubrication and heat dissipation. This pump is used independently as a roughing pump

and also in tandem with a turbomolecular pump at the exhaust port (10^{-3}torr) to achieve pressures sufficient for initiating turbo start-up.

A turbo molecular pump is a type of momentum transfer pump that is made by several manufacturers (e.g. Pfeiffer). The turbo utilizes the interaction of gas molecules with high-speed surfaces to direct the molecules into an outlet. It achieves this by operating at speeds which put tip velocity at comparable speeds to molecules (i.e. 418m/s for N_2 at its' most probable velocity). This pump uses an axial compressor where angled blades are positioned radially inward from the edge of a circular disc. These discs are mounted to a shaft and staggered in between stationary stator blades of similar construction.[47,91] Once molecules enter the pump they are compressed in stages. Most gases except hydrogen and helium can be readily pumped and compressed. This inadequacy is a result of the high average velocity of low mass molecules as dictated by the Maxwell Boltzmann velocity distribution.[1,47] There are three different turbos mounted to the chamber which are defined by their pumping speeds: 510 l/s on the main chamber, 60 l/s on the manifold, 170 l/s turbo at the high pressure cell (to be discussed). These values are theoretical and actual pumping speeds are dictated by the conductance of the mounting point. Typical pump down time from atmospheric pressure to 10^{-7}torr is approximately 30min. Base pressures $<10^{-10}$torr can be achieved after high temperature heating of the UHV apparatus ($\approx 150^{o}$C) for 48 hours.

Pressure in the system is measured using an Bayard-Alpert nude ionization gauge. The gauge consists of a concentric open grid, a filament outside the grid along the axial direction, and a collector (electrode) located in the central axis of the grid.[47] This is

a type of hot cathode gauge. The function of this device is the following: by applying a voltage, typically +30V, to the tungsten filament electrons are ejected through thermionic emission. The filament operates at a constant emission current of 1mA but is adjustable. The grid is kept at a potential of +180V and the design creates an inwardly directed radial electric field that accelerates electron through a potential of 150V which is an optimized value to achieve the largest ionization probability. The electrons essentially ionize gas molecules in the surrounding area or collide with the grid itself. The rate of ionization is proportional to the number of molecules and therefore the pressure.[47] The ions are accelerated towards the collector filament (held at 0V) by the concentric grid and upon collision with the collector neutralize by accepting an electron. This process induces a current ≈10nA in this collector which can be measured and calibrated for a certain gases (e.g. N_2). Due to the creation of soft x-rays (<180eV) through the photoelectric effect by collision of electrons with the grid, the x-rays eject electrons from the collector and induce a current. This problem becomes most apparent at low pressures $<10^{-9}$ where electrons have few gas molecules to interact with. This sets the pressure limit, or more formally defined as x-ray limit, of the gauge at $3x10^{-10}$torr. The accuracy of the gauge readout is ±20% when corrections are made for different gas sensitivities according to manufactures specifications. However, it is generally believed that the accuracy is within but not exceeding ±50%. All components are regulated electronically by a control unit with digital display readout of the pressure derived from the ion current.

Another feature of the vacuum chamber is the high pressure cell. This area has a volume of 0.4L and allows transmission of IR through CaF_2 mounted windows (discussed in the IRAS section). The sample probe can be translated vertically into this area through a differentially pumped sliding seal. Differential pumping is achieved by both a rotary pump and a turbo pump. This isolated area can then be filled with high pressure gas or gases for reaction studies after sample preparation in-situ. This area is thus a unique feature of this UHV chamber. Pressure is measured with an MKS Baratron pressure gauge which is a type of differential pressure gauge that utilizes a capacitance diaphragm. The gauge measures the capacitance change induced from pressures exceeding 1torr from a reference value that is maintained at essentially zero pressure. The maximum measurable pressure on our system is 1000torr. This type of gauge has an accuracy of ±1%.

Auger Electron Spectroscopy

Auger electron spectroscopy is a surface analytical technique which utilizes an electron beam to generate emission of secondary electrons characteristic of the target sample. A brief description of the theory, instrumentation, and its use for the data presented in this thesis is discussed below. Additional information on the subject can be found in the references herein.

Pierre Auger discovered the Auger effect while studying x-ray photoionization of noble gases.[93] Auger observed in the distribution of backscattered electrons unique secondary electron features that were independent of the incident x-ray energy and

specific to the noble gas under consideration. The kinetic energies of these electrons could not be described by the photoelectric effect:

$$E_{kinetic} = h\upsilon - B_e - \varphi$$

These secondary electrons were ascribed as originating from an electronic rearrangement caused by a radiationless process. Since the kinetic energy of an auger electron signal was dependent on the discrete energy levels in the element and independent of the incident beam the usefulness for characterizing specimens in material science became obvious.

The Auger radiationless process was rationalized and proved using theoretical methods to involve (i) creation of a vacancy by the ejection of a core level electron (ii) radiationless transition of an outer-shell electron into this vacancy (iii) energy transfer from the radiationless process to an outer-shell electron (iv) ejection of this outer-shell electron (see **Figure 8**). The Energy is conserved during this process and the auger electron is emitted with a kinetic energy equivalent to:

$$E_{KLM} = E_K - E_L - E_M - \delta E - \varphi$$

where E_{KLM} is the kinetic energy of the auger electron, $E_{K,L,M}$ are the binding energies of the electron in the K, L, and M shells, δE is the energy shift caused by relaxation effects, and φ is the work function of the sample. The binding energy is the energy necessary to bring a core level electron to the Fermi level (E_F) while the work function φ is the energy required to eject the electron from E_F into vacuum. The notation of these transitions is discussed below. As can be seen in **Figure 8** the sample is left in a double ionized state. The AES process is a three state process and therefore only valid for all elements with

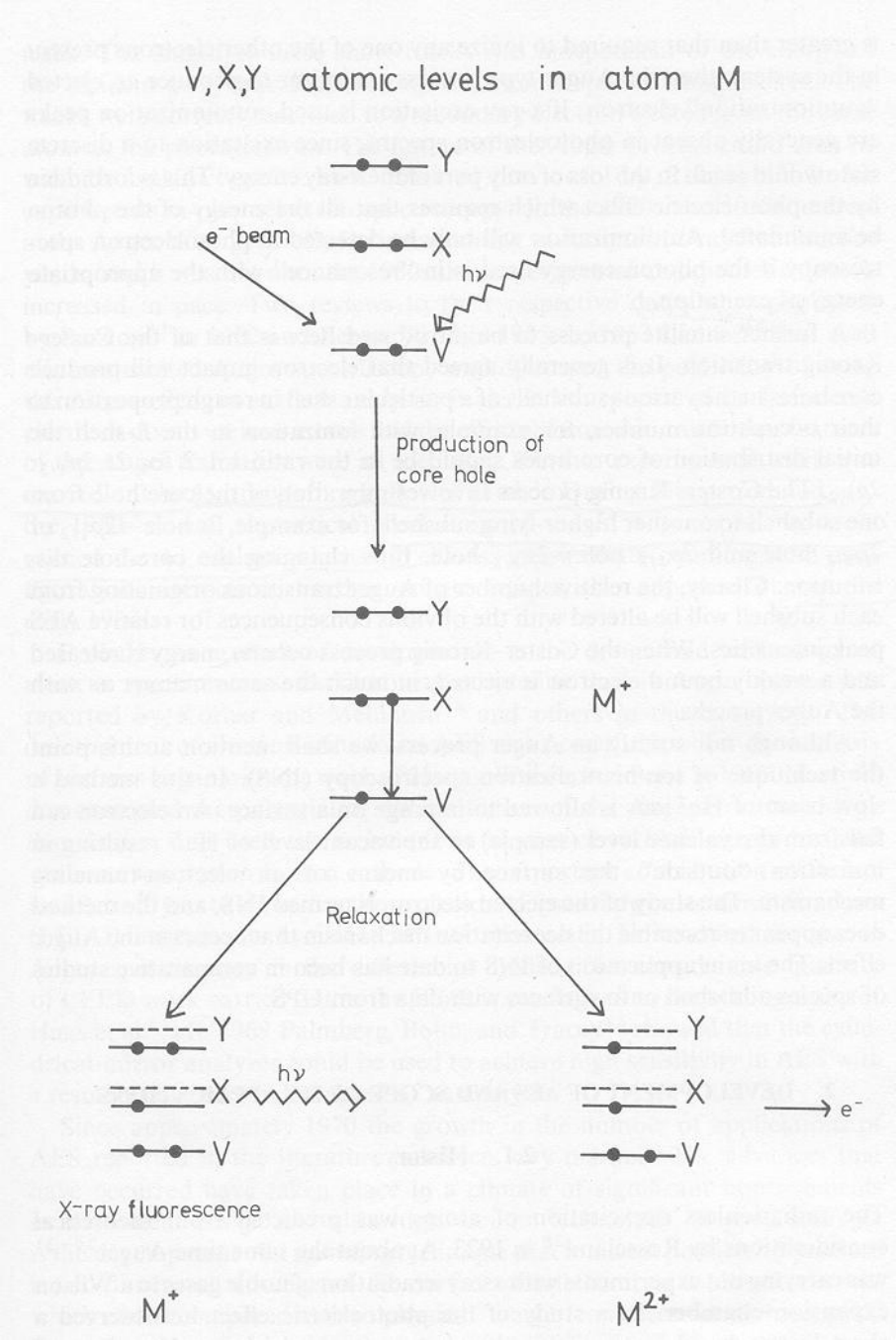

Figure 8. Auger electron transition.[93]

atomic mass greater than 2; hydrogen and helium cannot be detected using this method. The Auger effect is governed by the transition probability and the impact cross section of the incident beam.[93-95] The transition probability for an auger emission decreases for elements with Z>20 due to fluorescence. This phenomenon is due mainly to the various relaxation pathways that result for large electronic configurations[93].

The AES apparatus used in this study is a commercial instrument made by Perkin-Elmer. The AES spectrometer consists of an electron gun and an energy analyzer which can detect Auger electron peaks in the total secondary electron energy distribution. These two components are mounted in one unit coaxially with the energy analyzer outer and the electron gun inner. This system, as with all electron spectroscopy, requires the use of ultra-high vacuum conditions to allow a sufficient mean free path of the ejected electrons from the sample through the analyzer. This is typically $<10^{-6}$torr. The electron generation for the electron gun occurs from a heated tungsten filament operating at a temperature of approximately 2500K. The electrons are accelerated through by a positive potential applied to the lenses along the cylindrical direction of the gun. The filament potential is held negative to ground while the accelerating plates are held near ground potential[93]. The primary beam energy can be adjusted using a commercial power supply.

The energy analyzer records the energy distribution of emitted electrons. The analyzer consists of coaxial cylinders with the inner kept at ground potential while a negative potential is applied to the outer cylinders. The name given to this type of analyzer is cylindrical mirror analyzer (CMA). The voltage is ramped and electrons

emitted from the sample pass into the CMA through the entire azimuthal angle 2π at an entrance angle of 42.7degrees.[93,94] This angle produces the highest throughput. Electrons move in a parabolic path through the analyzer and into the multiplier. A channeltron continuous dynode multiplier is used. Here, incident electrons collide with semiconducting glass and generates 10^7-10^8 secondary electrons which results in a final signal gain of 10^3-10^5.[93,94] Multiplier operating voltages of 1-3kV are typically used. The AES utilizes a lock in amplifier for phase sensitive detection along with RBD computer software for analysis.

The ratio between the primary electron beam and the binding of core level electrons E_p/E_b to achieve the highest signal is about 3 (see **figure 9**).[93,95] Therefore, the voltage of the electron gun is kept greater than the binding energy of the core level electrons in the specimen. This means operating voltages in excess of 1000eV are necessary. Typical AES electron energies range from 20-600eV. This makes the AES technique extremely surface sensitive as the escape depth of electron in this energy range is approximately 2-10 layers as depicted in **Figure 10**.[93,94] The electron beam diameter is 25-100μm. The sensitivity is approximately 0.1 to 1 atomic percent with scanning rates of 1eV per second.[93-95] The analyzer transmission and resolution are about 10% and 0.6% respectively.[94] The instrumentation accuracy is about 1ev.[94]

The Auger peaks are superimposed on a continuous background of secondary electrons generated from the high incident electron beam. The AES features can be more easily observed by differentiating the energy distribution function N(E). The AES spectrum is therefore presented as dN(E)/dE. The notation is written with the initial

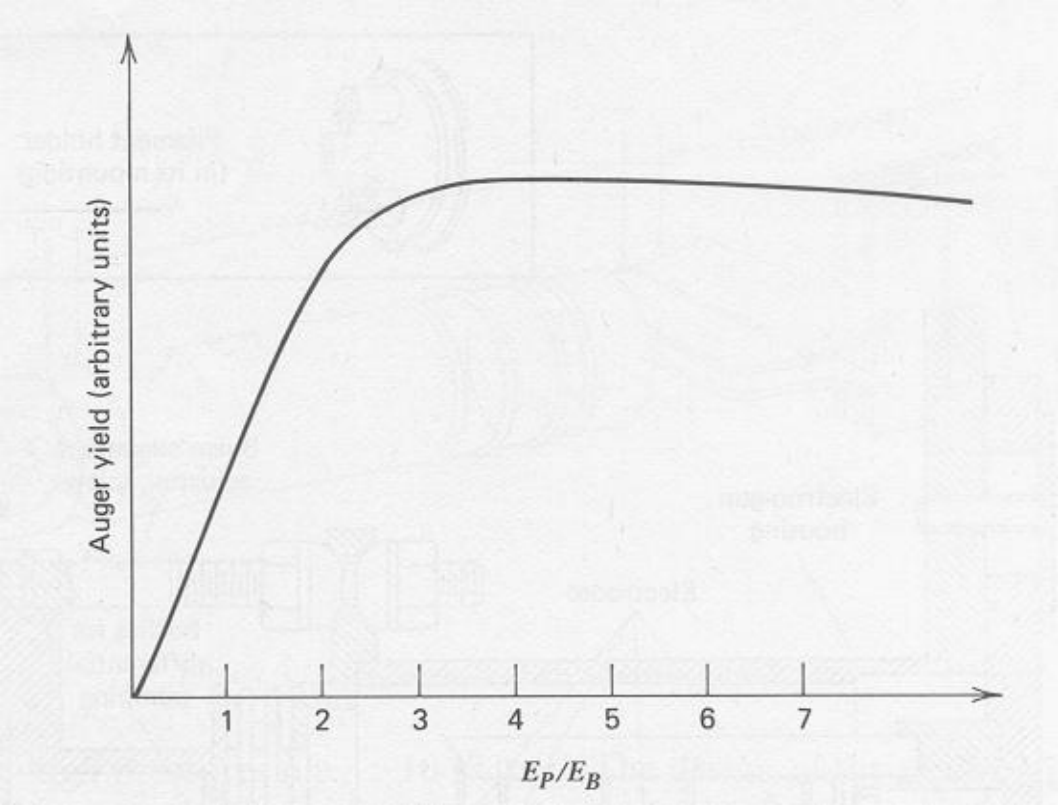

Figure 9. Primary electron-beam energy vs. binding energy. [93]

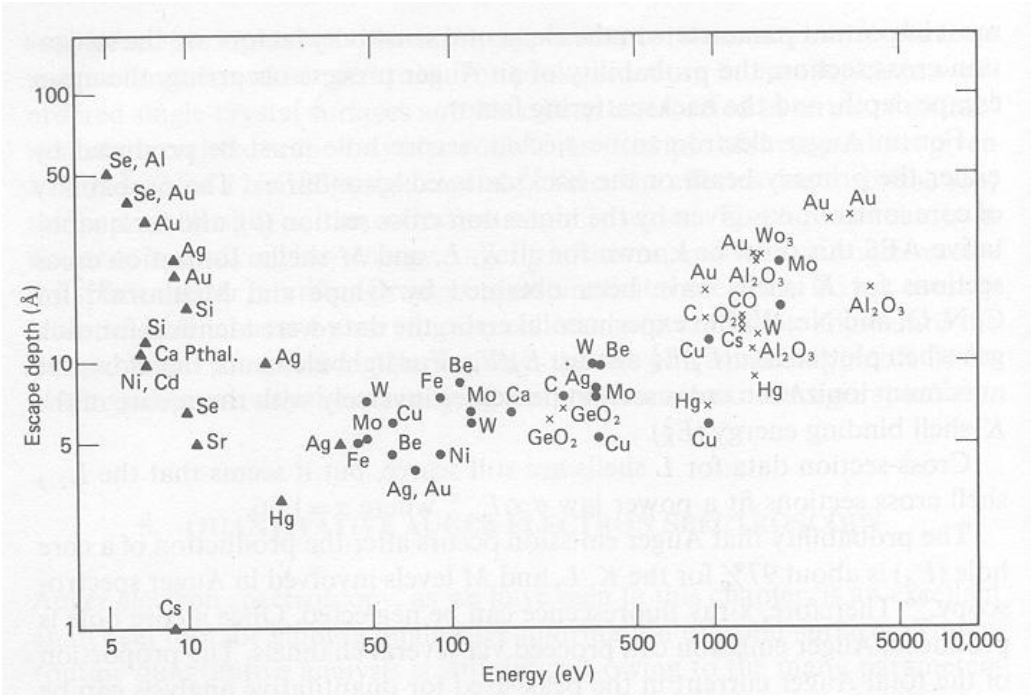

Figure 10. Electron escape depth.[93]

vacancy characterized by the principal, angular momentum, magnetic, and spin quantum numbers $(nlm_lm_s)^I$ resulting in final vacancies (nlm_lm_s) and $(nlm_lm_s)'$ and can be represented by the following expression[93]:

$$(nlm_lm_s)^I \rightarrow (nlm_lm_s)\ (nlm_lm_s)'$$

This process can also be expressed by $V_pX_qY_r$ where p,q, and r are the subshell indices or J values. The letters correspond to shells K,L,M,N corresponding to principal quantum numbers 1, 2, 3, 4 and subshells s,p,d,f which are notation for angular quantum numbers 0,1,2,3.[93] For example, for K series transitions the following notation could be used $KL_1L_2 = 1s2s2p_{1/2}$ or $KL_2L_3 = 1s2p_{1/2}2p_{3/2}$. For L series transitions $L_1M_4M_5 = 2s3d_{3/2}3d_{5/2}$.

AES can be used to determine the concentrtion of a contaminant or over-layer species on a substrate. This type of analysis can be achieved quantitatively by using the following relationship:

$$C_x = (I_x/ S_{x,\ Ag}) / \Sigma\ I_{alpha} / S_{alpha,\ Ag}$$

where I_x are the peak to peak heights, S_x is a sensitivity factor of the element. The AES technique can also be used to estimate the thickness of a film on a conducting substrate.[94,95] This can be achieved by the relationship below[96]:

$$I_s = I^o_s \exp(-t/\lambda^s_i \cos\alpha)$$

where I_s and I_{s0} correspond to the AES signal intensity of the clean substrate and film covered substrate, t is the film thickness, λ_i^s is mean free path of the main AES energy of the substrate through the film in its bulk form, and α is the emission angle with respect to the surface normal (42.7^o) .

The various growth modes of over-layers on metal substrates can be used as a calibration for the deposition rate in monolayers per second. There are three growth modes (i)Volmer-Weber, (ii) Stranski-Krastanov, (iii) Franck-van der Merwe which can be viewed in **Figure 11**.[2,3,96] If the over-layer is assumed to grow epitaxially the intensity of the substrate signal will attenuate according as the equation above. As can be seen in **Figure 11** a break in the linearity is observed after the first complete layer is formed. The intensity change decreases with increasing thickness of the over-layer exponentially. This type of breakpoint analysis can be used to determine when a complete monolayer has covered the surface.[96] When this analysis is determined as a function of time it can be used to establish the vapor deposition rate in monolayers per second. This technique has been used for the calibration of Rh and Pt in this thesis.

Microscopy Techniques

Obtaining an estimate of particle size is an essential part of the characterization process of high surface area technical catalysts and model catalysts samples. Historically, particles size estimates have been determined through dispersion measurements by calculating weight percent of deposited metal and total uptake of chemisorbed gas (CO, H_2, etc.). The dispersion method has proven fruitful and is still widely used today for determining fairly accurate particle size estimates. However, developments in microscopy techniques over the last 40 years have allowed atomic resolution of particle sizes to be imaged on a routine basis. These instruments are now in widespread use throughout industrial and academic settings and have proven advantageous in calculations of particle sizes, size distributions, and particle densities.

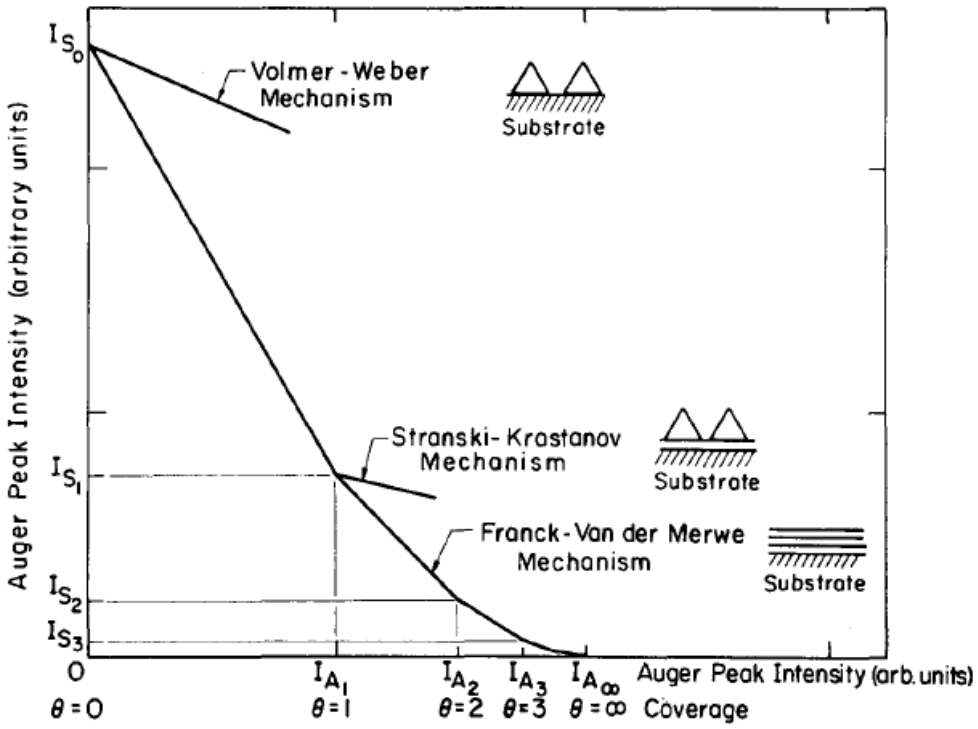

Figure 11. Various growth modes determined with Auger electron spectroscopy.[2]

Discussed below is a brief description of two microscopy techniques (i) scanning tunneling microscopy and (ii) transmission electron microscopy that were employed for estimating particles sizes. Both methods rely on the use of an UHV system. For a more comprehensive description the reader is referred to the references herein.

Scanning Tunneling Microscopy (STM)

STM is a highly sophisticated analytical method that utilizes the phenomenon of quantum electron tunneling to produce an image that is representative of the atomic structure of the surface being probed. Tunneling is the process by which a particle (e.g. electron) can surmount a potential barrier greater than its energy.[97,98] In terms of STM, an atomically sharp metal tip is positioned a few angstroms above the sample surface. If a potential is induced by either biasing the surface or the tip large enough to surmount the barrier electrons will continuously flow across the barrier creating a measurable current in the nA regime.[97,98] This tunneling current can be described as:

$$I = \int_0^{eV} \rho_s(r,E)\rho_t(r,\pm eV,\pm E)T(r,eV,E)dE$$

where ρ_s and ρ_t are the density of states of the sample and tip, r is the tip location, E is the tip energy level, the ± corresponds to both to positive (eV > 0), and negative sample bias (eV < 0), and T is the tunneling transmission probability.[99] To a simpler approximation assuming the barrier is much larger than the sample bias the current can be estimated as:

$$I = cVe^{\sqrt{\phi z}}$$

where c is a constant, V is the bias voltage, ϕ is the tunnel barrier height, and Z is the tip surface separation.[100] As can be seen, the tunneling current depends on the distance between the tip and surface and the local density of states (LDOS). This makes the STM extremely sensitive to corrugations in the surface layer such as step and kink sites described in the introduction section. An STM image is not a real space 3-dimensional topographical image (as in a contour plot) of the surface as the tip is effected only by the LDOS during analysis and contrast differences in the image should only be interpreted as such. However, height and width measurements of surface features such as particles can be conducted once accurate characterization of the sample has been performed with other analytical methods. Such analysis would involve elemental analysis (AES, XPS, etc.) and/or diffraction measurements (XRD, LEED, etc.)

The movement of the STM tip is controlled in both the xy and z planes by piezoelectric transducers. Two modes of operation typically used in STM are the constant current mode and constant height mode.[97,98] Constant current mode is used most frequently and applies continuous feedback to the z piezo (vertical component) to hold the tunneling current at a constant value. This method measures the displacement in the z-direction (vertical) as a function of the lateral movement in the xy-plane (horizontal). Constant height mode holds the distance between the probe tip and surface constant while measuring the tunneling current in the xy-plane. The lateral resolution and depth resolution of an STM are approximately 0.1nm and 0.01nm respectively.[97,98] Particle diameter estimates using STM are frequently determined using the height measurement and geometry to calculate diameter (e.g. assuming the particle is a hemispherical cap and

using the radius to calculate diameter) as well as taking into account tip convolution effects in the lateral direction.

Transmission Electron Microscopy (TEM)

The process of passing an electron beam through a sample and separating the various scattered electrons is the basic function of the TEM system. The TEM apparatus exploits the wave nature of electrons and a series of electromagnetic lenses to create an image of a surface with contrast indicative of the scattering events.[101] Electrons are initially generated by emission from a filament and controlled by deflector coils which are both used in standard electron guns. The accelerating voltage is typically 100-300keV.[101] The electrons are focused by a set of condensers which generates an electromagnetic field symmetrically around the optical axis of the scope. The electron beam has a spot size of <1μm. The convergence angle of the electron beam, illumination of the sample, along with reduction of spherical aberration, distortion, and astigmatism can all be controlled by the condensers and condenser apertures.[101] Below the sample is an objective lens which allows magnification and an aperture in the back focal plane which eliminates diffracted electrons from the image. The image is generated by finally passing through projection lenses and onto a fluorescent screen. A shutter and a camera are located below the fluorescent screen to record the image. Resolution of modern TEM instruments is <0.1nm.[101]

Samples for use in TEM have to be sufficiently thin to allow transmission of electrons in the energy range of the accelerating voltage. The thickness is typically in the nanometer regime.[101] To install samples on the TEM stage they are prepared on a

circular mesh with a diameter of ≈3.05mm with a thickness of several micrometers; the mesh in not transparent to the electron beam. The actual sample is prepared on the mesh where transmission of the beam occurs through a thin sample covering the holes in the mesh. For experiments to be discussed in the results section a carbon coated molybdenum mesh was used to prepare model catalyst samples. Carbon thickness is estimated to be 20nm. The C/Mo mesh was installed in the UHV chamber described in the UHV experimental section. Sample preparation is described in the corresponding sample preparation experimental section. TEM measurements were conducted ex-situ by a commercial JEOL 2010 available for use in the Biological Sciences facility at Texas A&M University.

Thermal Desorption Spectroscopy

Thermal desorption spectroscopy (TDS) also known as temperature programmed desorption (TPD) is an analytical method which allows the desorption temperature of adsorbates to be monitored with a mass spectrometer. In the following section some of the properties that govern the interaction of gas phase molecules with a surface under UHV conditions along with the basic analytical properties of the TDS system are discussed. These topics are explained in the context of experiments performed in the results and discussion section. For a more comprehensive analysis of these systems the reader is referred to the references herein.

Two competing phenomenon on a surface are desorption and adsorption of molecules. When a system is at equilibrium the rate of desorption equals the rate of adsorption.[2,47] Adsorption can defined as a process by which a molecular species

interacts with a surface such that it loses vibrational and/or rotational degrees of freedom. Such a process results in a negative change in entropy.[2,47] The process becomes favorable at relatively low temperatures if the enthalpy of adsorption is negative. Therefore, adsorption is an exothermic process.

Two types of molecular adsorption processes that can occur are physisorption (physical adsorption) and chemisorption. Physisorption is a process that can be described as a molecule in a bound state involving van der waals forces and having an adsorption energy in the range of ≈6kcal/mol.[2,3] Chemisorption can be defined as a molecule being adsorbed in a bound state through electron transfer or sharing and having an adsorption energy of approximately >10kcal/mol.[2,3] These processes are depicted in the energy diagram of **Figure 12**. It is observed that there are two potential energy minima or wells a molecule can fall into. These depend on the both the properties of the surface and the adsorbing molecule. The process of dissociative adsorption has a much deeper well on account of the increase of entropy relative to the associatively adsorbed state. Molecules can also diffuse across the surface with very low activation energy in both the physisorbed and chemisorbed states (see introduction section).

The adsorption energy can be estimated by understanding the surface residence time which depends exponentially on the temperature of the surface (see equation). The heat of adsorption is always listed with a positive sign in contrast to the negative sign used for exothermic processes[47]:

$$\tau = \tau_0 e^{\Delta H/kT}$$

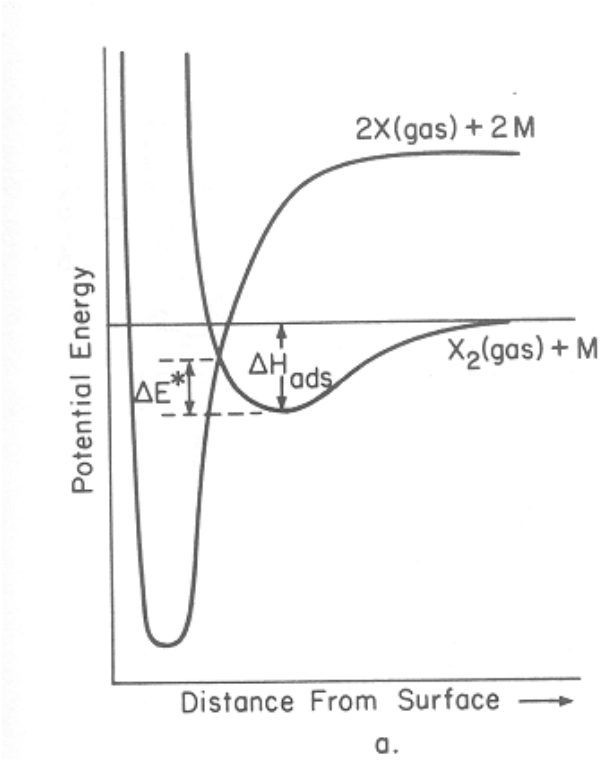

Figure 12. Energy diagram for adsorption.[2]

Once a molecule is adsorbed it can be held almost indefinitely by controlling the temperature. For example, a molecule with an adsorption energy of 80kJ/mol will have a residence time of approximately 15 seconds at room temperature while at a temperature of 77K it will have a stay time of 10^{41}s.[47] The activation energy of adsorption is closely related to the desorption energy. In practice the measurement of desorption energies is not a direct measurement of adsorption because of the many phenomenon that can happen at the surface upon desorption, that being, dissociation or diffusion to a lower energy site or residence time. However, calculations of desorption energies are closely related to adsorption and it is generally easier to perform desorption measurements. This energy can be explored for molecules that will not dissociatively desorb.

The desorption of molecules from a surface can be monitored with a commercial quadrupole mass spectrometer (MS). The basic description of the instrument is as follows. The instrument utilizes 4 parallel cylindrical conducting rods oriented in a square configuration.[47] Two of the rods are held at a potential $U+V\cos(\omega t)$ while the remaining two rods are held at a $-[U+V\cos(\omega t)]$; thus both pairs have a DC component and also an AC component at a radio frequency of a few MHz. This configuration result in an analyzer which can transmit ions of a certain m/e ratio down the longitudinal direction of the analyzer while forcing other ions towards the outer direction. The ions make their way through the analyzer and strike a negatively charged plate which neutralizes the ion and results in a current which can be detected. The signal can be enhanced by using a channeltron multiplier similar to that described in the auger electron spectroscopy section.

The TDS set-up was custom built in the early 1990's by Dr. D. Wayne Goodman and co-workers and combines 4 separate components.[92] These four components are a power supply, thermocouple, mass spectrometer (MS), and computer for data aquisition. The data acquisition simultaneously controls the heating rate of the surface while scanning and monitoring the mass signals with the MS. The feedback loop involves the thermocouple and the power supply. The power supply is directed by a 0 - 5V signal input from the computer's digital to analog converter. The output from the power supply is adjusted to give a linear temperature rate and fluctuations in temperature are controlled by a proportional-integral-derivative controller (PID). The thermocouple used in experiments is a c-type W/Re spot welded to the sample. This thermocouple is used with an Omega cold junction compensator.

A TDS profile can be analyzed by numerous methods in order to calculate the activation energy of desorption. Two particular methods are the redhead peak maximum method or by solving the Polanyi –Wigner Arrhenius expression[102]:

$$r = -\frac{d\theta}{dt} = k_{des}\theta_n = \upsilon(\theta)\theta^n e^{-\frac{E(\theta)}{RT}}; T = T_0 + \beta t$$

where r is the rate of desorption, θ it the coverage in monolayers, t is the time, k_{des} is the rate constant for desorption, n is the order of desorption, v is the pre-exponential factor for desorption and E(θ) is the activation energy for desorption. The temperature can be determined from the initial temperature and the heating rate. Redhead peak maximum offers a simplified expression. The redhead can be applied for coverage independent desorption parameters and first order kinetics where E_{des} is only valid for the zero coverage limit[103]:

$$E_{des} = RT_{max}\ln\left(\frac{\upsilon T_{max}}{\beta}\right) - 3.46$$

The parameter υ is derived from the pre-exponential factor in transition state theory. Assuming a tightly bound transition state that resembles the ground state of the desorbing molecule the frequency is chosen to be usually 10^{13}/s.[1,47] This value could increase to 10^{14} - 10^{19} for loosely bound molecules which have greater degrees of translational and rotational freedom.

Infrared Reflection Absorption Spectroscopy

Infrared reflection absorption spectroscopy (IRAS) is a surface analytical technique which utilizes the reflection of infrared light at grazing incidence to obtain vibrational information of surface adsorbates. The IRAS technique is versatile as analysis can be conducted under both UHV and atmospheric pressure conditions during a heterogeneous catalytic reaction (depending on the peripheral optical components). IRAS thus offers an essential perspective of the surface aside from traditional electron spectroscopies which are typically restricted to UHV conditions. In the following section the IRAS apparatus and theory of operation are briefly discussed in the context of experiments to be addressed in the results and discussion section. For a more comprehensive discussion the reader is referred to the references herein.

The main component of the IRAS apparatus is a commercial Fourier transform infrared spectrometer. This apparatus utilizes a Michelson interferometer which uses a half-silvered beam-splitter to split incident IR light into two beams with separate pathways towards stationary and movable cube-corner mirrors.[104] Each beam is then reflected back towards the beam-splitter with the total distance traveled by one of the

beams varied by the movable mirror (oscillating at 40kHz). The path length difference between the beams upon recombination at the beam splitter results in an interference spectrum which is detected by liquid nitrogen cooled mercury cadmium telluride detector (detection range 5000-800cm^{-}). The main purpose of using an interferometer in this regard is to allow the many frequencies emitted from a resistively heated SiC IR-source to pass through the system simultaneously but analyzed individually.[105] This process is achieved by utilizing a monochromatic HeNe laser for real time measurement of path length difference in the interferometer and fast Fourier transform analysis to resolve the IR interferogram into individual frequency components. IR measurements conducted in this manner results in fast scan times (≈4min for 512 scans) at a maximum resolution of 2cm^{-} for our current apparatus.

The reflection mode of the IRAS was performed using two separate experimental set-ups. The first was used without polarization and at pressures below 10^{-6}torr while the second with polarization-modulation for spectra up to 500torr. In the absence of polarization modulation the infrared area was purged with N_2 to eliminate gas phase water and carbon dioxide. Polarization modulation will be discussed shortly. Otherwise, the following experimental set-up was identical for both apparatus. The infrared reflection part of the IRAS set up can be viewed in **Figure 13**. Infrared light reflected from a clean metal surface can be described by the following relationships using the complex index of refraction n=n+ik and assuming $n^2+k^2 >> 1$ [6]:

$$R_s = \frac{(n-sec\phi)^2+k^2}{(n+sec\phi)^2+k^2}\ , R_s = \frac{(n-cos\phi)^2+k^2}{(n+cos\phi)^2+k^2}, tan\Delta = \tan\left(d_p - d_s\right) = \frac{2k\ tan\phi\ sin\phi}{tan^2\phi-(n^2+k^2)}$$

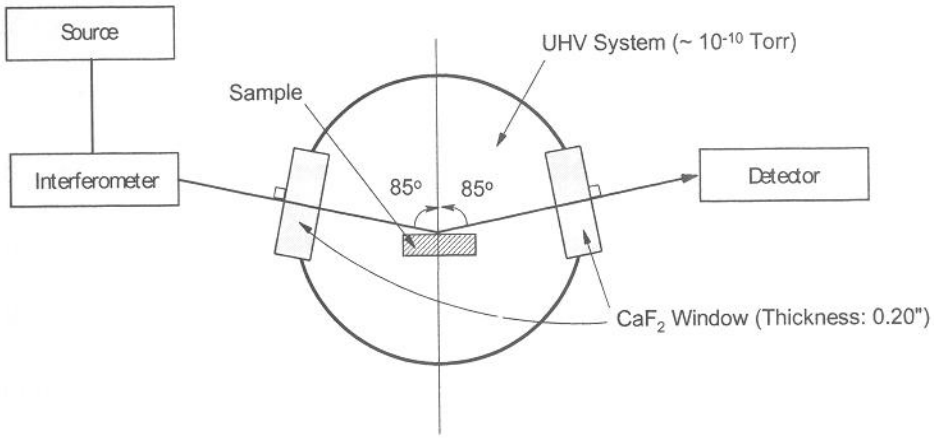

Figure 13. IRAS reaction cell.

where R_s and R_p are the intensities of the s and p polarized light, d_s and d_p are the phase shifts, ϕ is the angle of incidence, and E_s and E_p are the electric field components. For the system in **Figure 13**, the incident IR beam is focused through CaF_2 (IR cutoff ≈1000cm$^-$) windows attached to the vacuum chamber as described in the UHV section. The beam reflects from the sample at a grazing incidence angle of 85 degrees from the surface normal. Such high angles of incidence are necessary due to the strong dependence of the absorption intensity on the electric field component, $E_p^2 sec\phi$, perpendicular to the surface (see **Figure 14**).[6] The electric field component parallel to the surface suffers a uniform phase shift of 180degress at all angles of incidence thus eliminating its electric field by destructive interference. Essentially, there is no electric field component parallel to the surface which can interact with an adsorbate whose dipole moment is parallel to the surface. This effect gives rise to a strict selection rule which dictates that only components with dipole moments perpendicular to the surface can be observed in IRAS.[6]

Separating the IR-absorption of surface vibrations from gas phase vibrations is achieved by polarization modulation.[6,105] This technique is used as the vibrational-rotational frequencies of gas phase molecules often overlap and shadow their surface vibrations once attached to the substrate. Gas phase absorption of p polarized light becomes a problem at pressure exceeding 10^{-3}torr. Since gas molecules can also absorb s polarized light, by modulating the incident beam through p and s polarizations and obtaining the ratio of the s and p components one can generate a spectrum essentially free of the gas phase signal. This can be achieved by the following: prior to entering the

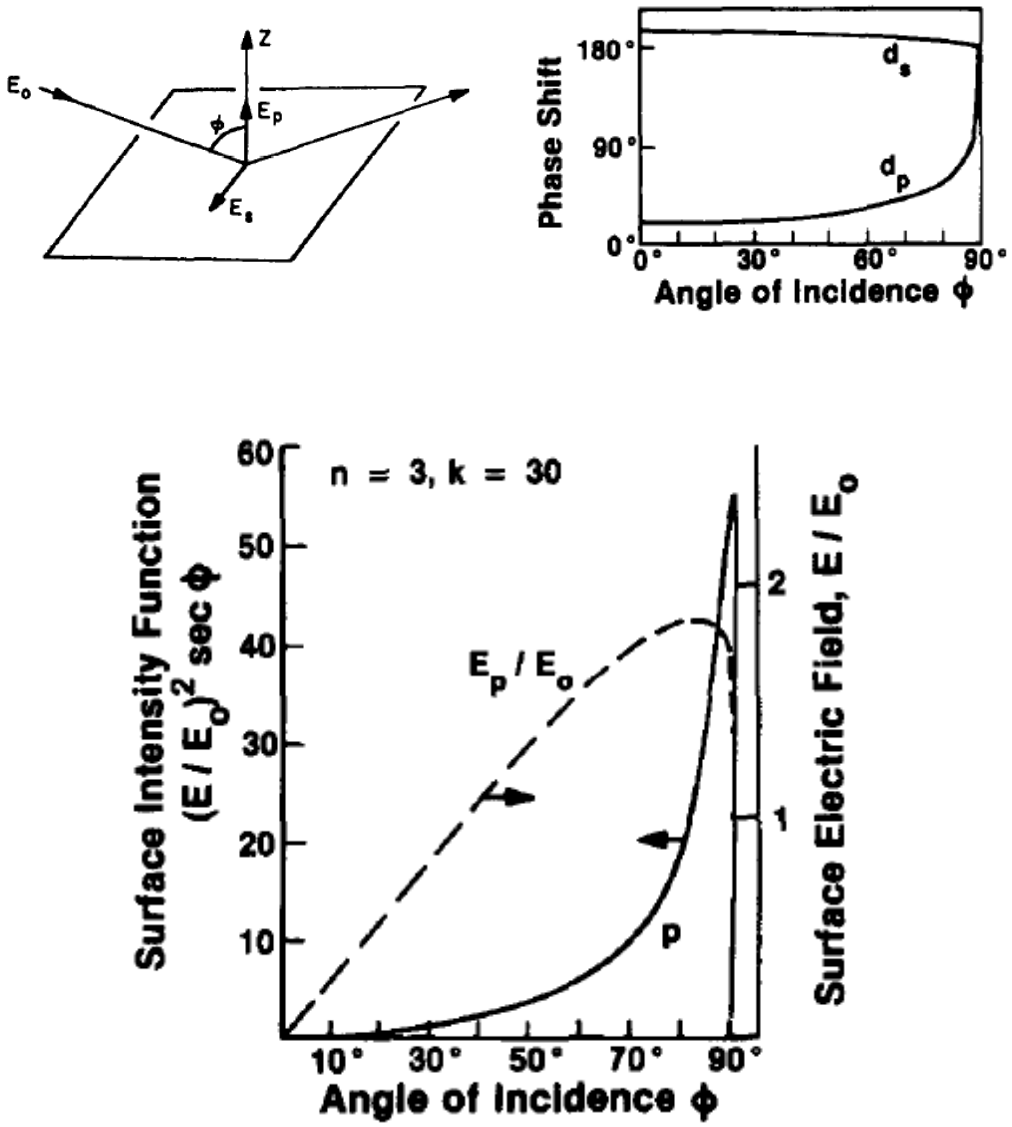

Figure 14. IRAS selecton rule.[6]

CaF_2 window of the high pressure cell, the IR beam is focused by a Au coated parabolic mirror with a focal point at the position of the sample. The beam then passes through a wire grid polarizer (Graseby Specac, Inc.) aligned to allowed a p-polarized electric field vector with respect to the sample face followed by passing through a photoelastic modulation optical head (II/ZS50, Hinds instruments) containing a ZnSe crystal aligned 45 degrees from the surface normal. A sinusoidal voltage applied to the ZnSe crystal induces mechanical oscillations along the optical axis of the crystal generating birefringence (double refraction). The result is a phase lag of one electric field component which results in a rotation of the resultant electric field vector. This process generates a rotation of 90 degrees with a frequency of 50kHz. Essentially, the incoming beam is rotated periodically between p and s configuration relative to the surface normal. The spectrums obtained from the s is subtracted from the p and normalized to the total intensity of both p and s. This is achieved using a digital to analog converter, multiplexing electronics unit, a photoelastic modulator controller, and a synchronous sampling demodulator with a speed of 10kHz. Additional artifacts were removed by subtracting the background spectrum of a clean surface.

IRAS has been most successful in obtaining the vibrations of carbon monoxide adsorbed on Pt-group single crystals and nanoparticles.[6] This is because of its relatively simple vibrational and electronic structure see **Figure 15**. IRAS sensitivity for adsorbed CO is approximately 1/1000 of monolayer.[6] It has been determined experimentally the CO stretching frequency is sensitive to the geometry of the adsorption site and the number of CO molecules in the ad-layer.[6] Typically, the vibrational frequency of CO

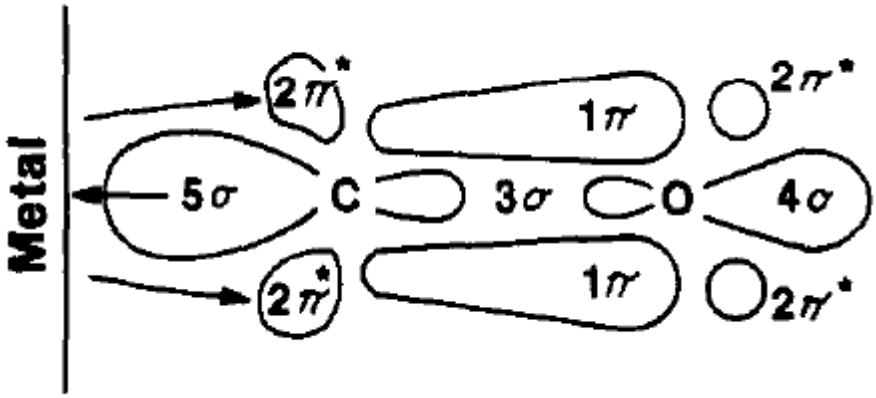

Figure 15. CO molecular orbital diagram.[6]

chemisorbed on a surface is 30 - 50cm^{-} lower than its gas phase value (2143cm^{-}).[6] This result has been attributed to three main influences (i) mechanical renormalization (ii) interaction of the vibrating dipole with its image in the surface see figure (iii) chemical effects such as back-donation or dipole coupling.[6] In a theoretical treatment, Blyholder[106] estimated the 5σ orbital of CO to have the largest interaction with the electronic state in the surface. Back donation of electron density from the surface to the 2π* antibonding orbital CO tends to shift the frequency to lower energy. Frequency shift are also caused by intermolecular dipole-dipole coupling between adjacent molecules.[6,107] The magnitude of each effect above is highly dependent underlying substrate.[6,107]

Sample Preparation

A Mo(112) single crystal sample (circular disk, 0.986 cm diameter) was used as a substrate for film growth. The sample is resistively heated through a Ta wire lead welded to the edge of the sample, with temperature control and measurement accomplished via a W/Re thermocouple spot-welded to the rear of the sample.

Oxide supported model catalyst surfaces were generated in two steps: *(1)* preparation of SiO_2 film on the Mo(112) substrate and *(2)* vapor deposition of Rh or Pt metal on the SiO_2/Mo(112) sample. Several laboratories[108-111] have developed procedures for preparation of ultra-thin (1 ML) and thicker (several ML) SiO_2 films; a vapor deposition recipe similar to that developed previously in our laboratory was utilized for SiO_2 film growth.[111] Si dosing was accomplished by vapor deposition from a home-built doser consisting of Si held by a Ta filament. Silica films were grown by

alternating steps of *(1)* Si dosing at a sample temperature of T = 650 K in P ~ 5 x 10^{-6} Torr O_2, followed by *(2)* annealing at T = 800 K in P ~ 1 x 10^{-5} Torr O_2. This procedure was performed on both sides of the sample, such that *both* faces of the Mo(112) were covered with an SiO_2 film. After Si dosing was completed, the sample was annealed at T = 1000 K for 20 min in P ~ 2 x 10^{-5} Torr O_2 ambient to complete oxidation of the SiO_2 film. AES spectra of the SiO_2 film are similar to those previously observed[108,111]; indicating a fully oxidized Si (in SiO_2) AES feature (78 eV) with a SiO_2 film thickness which almost completely attenuated the Mo (187eV) AES feature (this corresponds to 5 ML (15 Å) SiO_2 film[108]). The ultra-thin silica film used for STM measurments was prepared by the oxidization of deposited Si atoms on Mo(112) and subsequent annealing to remove multi-layer SiO_2. Prior to Si deposition, the sample was flashed to 2100 K and then oxidized in 5×10^{-8} Torr O_2 at 850 K for 7 min. A p(2×3)–O surface was obtained after the oxidation. The silica film was then prepared by depositing less than 1 ML Si onto a Mo(112)-p(2×3)–O surface, followed by annealing at 800 K in 5×10^{-8} Torr O_2 for 5 min then increasing the temperature to 1200 K for an additional 10 min. This Si deposition/oxidation/annealing procedure was repeated several times until a constant Si/Mo AES ratio was achieved. The silica film was then annealed in UHV at 1200 K for 5 minutes. For TEM measurements, silicon was vapor deposited a carbon coated molybdenum grid under identical conditions as on the Mo(112) listed above.

Rh or Pt particles are generated on the SiO_2 film by vapor deposition (at a sample temperature of T = 300 K), using a home-built evaporative doser (high purity Rh or Pt wire heated on a tungsten filament). Rh or Pt was dosed *only* on the front side of the

SiO_2/Mo(112) sample. For Rh, the dosing rate on the SiO_2 was calibrated with a breakpoint analysis of the primary Rh AES feature (302eV) on the Mo(112) surface. This analysis showed a breakpoint at a Rh(302eV)/Mo(187eV) AES ratio of ~ 0.5. For the purposes of dose calibration, this ratio will be referred to herein as a monolayer equivalent coverage of Rh; typical Rh deposition rates were ~ 0.25 ML/min. Pt was vapor deposited (typical dose rates ~0.1 - 0.2 ML/min) at a sample temperature of T = 300 K, with the dose calibrated via breakpoint analysis on Pt/Mo; the breakpoint occurred at Pt(68eV)/Mo(187eV) = 1, which will be referred to herein as a 1 ML Pt coverage. To assess the uniformity of the deposited Rh or Pt coverage across the sample, AES measurements were conducted at various points across the sample surface for a Rh/Mo(112) and Pt/Mo(112) coverage of θ_{Rh} = 1 ML. Based on these measurements, we estimate the coverage across the sample varies no more that ±15% from the stated coverage.

Pt(110) (circular disk, 1.04 cm diameter), Pt(100) (circular disk, ≈1 cm diameter), Rh(111) (circular disk, 0.986 cm diameter) single crystal samples were also used for analysis. Each sample temperature was monitored with a C-type W/Re thermocouple spot welded to sample. Each surface was cleaned by Argon sputtering followed by repeated oxygen annealing cycles in $5x10^{-7}$torr O_2 at 750K followed by final annealing at 1250K in UHV until AES did not reveal any contaminant features (C, S, etc.).

Sample Characterization

CO-TDS experiments were conducted to provide an estimate of the number of Rh or Pt surface sites from CO chemisorption on particle samples, compared to Rh(111) or Pt(110) single crystal respectively. For these experiments, Rh or Pt metal is deposited on the SiO_2 film, prior to TDS measurements, Pt or Rh surfaces were cleaned with O_2 (5 x 10^{-6} Torr, 600 K, 10 min) to remove residual carbon from the vapor deposition process. The sample is then run through an initial TDS cycle in vacuo. Next, a saturation coverage of 4 L CO is dosed on the sample at T_{ads} = 175 K. The sample was then heated at a rate of ~ 5 K/s from T = 130 - 700 K to obtain CO thermal desorption spectra. TDS spectra (m/z=28) are obtained with negligible line of sight to the quadrupole from the sample. As expected, TDS spectra demonstrated negligible CO uptake from the sample leads (desorbed <100K), indicating CO adsorption and desorption is occurring on the particles.

Reference TDS spectra were obtained on the Rh(111) single and Pt(110) crystal samples for a saturation 4 L CO coverage. Since the number of surface atoms can be estimated on the single crystals, the integrated TPD spectra from the single crystal $\left(A_{TPD,Crystal}\right)$ can be used to convert particle TPD spectra integrated area $\left(A_{TPD,particles}\right)$ into an estimate of the number of surface sites $\left(N_{Particles}\right)$ on samples for a desired metal coverage: $\left(\frac{A_{TPD,particles}}{A_{TPD,Crystal}}\right)N_{Crystal} = N_{Particles}$. These estimates are then put into terms of metal sites per cm^2, by dividing by the Mo(112) sample area. For the Pt nanoparticles, two desorption features were observed in the CO-TDS spectra and were separated using

a Gaussian fit followed by integration to assess the relative percentage of terrace and step sites on the Pt/SiO_2 surfaces as a function of particle size. This kind of analysis has been applied successfully by previous investigators in studies of stepped Pt single crystal surfaces.[112]

Prior to CO-IRAS measurements, Pt or Rh surfaces were cleaned with O_2 (5 x 10^{-6} Torr, 600 K, 10 min) to remove residual carbon from the vapor deposition process. CO adsorption on Pt or Rh from residual CO in the UHV (P_{base}= $5x10^{-10}$ torr) background was also negligible. PM-IRAS measurements were conducted on Rh/SiO_2 surfaces during reactivity measurement were indicated. Experiments conducted in this manner subjected the nanoparticles to reactant gases in an identical fashion to those used for reactivity measurements. IRAS spectra did not show any CO adsorption on SiO_2/Mo(112).

STM measurements of samples were conducted to provide particle size distribution, aspect ratios, and an additional method for site estimates as a function of θ_{Pt}. STM measurements were conducted in a separate UHV chamber. Rh or Pt particles were deposited on an ultra thin (1 ML SiO_2) film at T = 300 K under UHV conditions. Using the particle size, distribution, and aspect ratio measurements, a geometric estimate of the number of active sites as a function of Pt or Rh coverage can be calculated assuming hemispherically shaped particles. Particle size estimates were also obtained using transmission electron microscopy (TEM). TEM measurements were performed ex-situ. Particle sizes were determined using software analysis. The average particle sizes from TEM were determined using the diameter-weighted average for >100 particles.

Gas Handling and Analysis

Adsorption Measurements

For TDS and IRAS measurements, ultrahigh purity (UHP) ^{12}CO was utilized for all IRAS and TDS experiments; CO gas was further purified by passing over a heated 3Å molecular sieve, followed by a LN_2 trap. UHP ^{13}CO (m/z = 29) (99%) was also used in several experiments, primarily to provide clarity in CO-TDS spectra obtained from ethylene (m/z = 28) pre-exposed surfaces. UHP C_2H_4 (99.98%) utilized for TDS and IRAS experiments, was further purified by multiple freeze pump thaw cycles. Gases were delivered to the surface through conventional leak valves (1 L = 1 x 10^{-6} Torr sec).

CO Oxidation Reactivity Measurements

CO oxidation reactions were conducted in a batch reactor mode in the contiguous high pressure cell ($V_{reactor}$ = 0.3 L). O_2/CO mixtures were pre-mixed (prior to charging reaction cell) with ultra high purity O_2 and CO; CO was further purified through a heated 4A molecular sieve and subsequent LN_2 cryogenic trap to remove any carbonyl impurities; O_2 was used without further purification. For example, an P = 8.0 Torr charge of a (1/1) O_2/CO reaction mixture contains P_{O_2}= 4.0 Torr and P_{CO} = 4.0 Torr. Initial reaction rates (<10% conversion) were measured with a baratron gauge in a technique described previously.[113] Control reactivity experiments conducted on prepared SiO_2 films (without Rh or Pt) to estimate any background contributions to the reaction measurements demonstrated that background reaction rates were typically no more than a few percent of the overall reaction rate at a given temperature. This indicates essentially all CO_2 production arises from the presence of the Rh particles. Reaction

data are initial rates obtained during the first 10% conversion of the batch cell mixture. Normalization calculations were conducted assuming one site per single crystal surface atom.

CO Hydroformylation Reactivity Measurements

Rh/SiO_2 samples are transferred in situ to the high pressure reactor cell for $C_2H_4/CO/H_2$ kinetic measurements. Reaction gases were added to the cell in the following order (i) CO, (ii) C_2H_4, (iii) H_2 at a ratio of 1:1:8 and a total pressure of 500 Torr. An initial GC sampling at T = 300 K was obtained, followed by heating of the Rh/SiO_2 sample to the reaction temperature. Product gases from the reactor are sampled at t = 1 hour to determine product formation and TOF values via gas chromatography using a HP 5890 with a flame ionization detector (FID). This instrument utilized a Hayasep column and helium carrier gas (30ml/min). Hydrogen and air flow rates were 30 and 400 ml/min respectively. Concentrations and retention times of product gases were determined using calibrated hydrocarbon gas mixtures, propionaldehyde standards, and standard literature FID sensitivity factors and GC techniques.[114,115] Reaction measurements were run to low conversions (< 10 % C_2H_4 conversion) and background reactivity measurements (on SiO_2 films) showed no activity for reaction across the reaction conditions probed, indicating reactivity occurs only when Rh nanoparticles are present on the SiO_2 surface. UHP H_2 was used as received. UHP CO was further purified via heated 4A molecular sieve and LN_2 trapping; UHP C_2H_4 was further purified by multiple freeze pump thaw cycles. Characterization reactions utilizing C_4H_{10}

hydrogenolysis were conducted in a similar fashion. Reactant C_4H_{10} was further purified via multiple distillations prior to use.

n-Heptane Dehydrocyclization

Reactivity measurements were conducted in a batch-reactor. This system is coupled to the UHV chamber which the samples can be translated *in-situ* after preparation. n-Heptane (Honeywell B&J brand >99.99% C7, 99.38% n-heptane) was obtained and first out-gassed by multiple freeze, pump, and thaw cycles followed by a triple distillation prior to use. Impurities of 2-methlyhexane and 3-methylhexane could not be detected. A detectable C7 impurity was methylcyclohexane (MCH) at a concentration of <100ppm. Kinetic studies in our lab demonstrate MCH dehydrogenation to be insignificant (<<0.001 molecules/site/s) at this concentration. Conversion of MCH is found to be suppressed by competitive adsorption with n-heptane. UHP Hydrogen was used without further purification. Reactions were performed at a total pressure of P_T = 495torr at a ratio of 31:1 H_2/n-C_7H_{16} and a temperature of 575K to allow comparison with literature data. n-heptane was administered into the reactor followed by hydrogen. Rate measurements were obtained using an HP 5890 gas chromatography with a flame ionization detector (FID). This instrument utilized a Porapak column and helium carrier gas (30ml/min). Hydrogen and air flow rates were 30 and 400 ml/min respectively. (HP 5890, FID). Rates obtained for Pt(110) and Pt(100) were acquired in an identical manner. Background reactions on the SiO_2/Mo(112) surface did not reveal any dehydrocylization, hydrogenolysis, isomeration, or cyclization products over the course of our reaction time (t=1hr). This

indicates all reaction products are catalyzed from Pt nanoparticles. Reaction were kept at low conversions typically <0.01%.

Calculations

An f.c.c. truncated octahedron can be described as a structure with 8 hexagon (111) faces and 6 square (100) faces. An f.c.c. truncated octahedron "cap" is shown in **Figure 16**. This surface can be described as having 3 square faces of (100) on the sides, 3 half hexagons of (111) on the side, and one full hexagon of (111) on top. Using the statistics by V&H[49] for a truncated octahedron, one can calculate the concentration of various surface sites on a "cap" where *m* is the number of atoms lying on an equivalent edge.

The number of (111) sites on a cubo-octahedron hexagon face:

$$\frac{C_9^3 sites}{face} = \frac{8(3m^2 - 9m + 7)}{8\ faces} = 3m^2 - 9m + 7$$

Total (111) face sites on a "cap"= 3 x half (111) hexagon faces on sides + 1 x whole (111) hexagon top face:

$$= \left(3 \times \frac{1}{2}\ \frac{C_9^3 sites}{face}\right) + \frac{C_9^3 sites}{face} = \frac{3}{2}(3m^2 - 9m + 7) + 3m^2 - 9m + 7$$

Total (100) face sites on a "cap" = 3 x whole (100) sites:

$$\frac{C_8^{4,5} sites}{face} = 3 \times \frac{C_8^{4,5} sites}{6\ faces} = 3 \times \frac{6(m-5)^2}{6\ faces} = 3(m-5)^2$$

The total C_6^6 is always 12 since there are only 3 square (100) faces and each C_6^6 lies at a corner.

To calculate the concentration of C_7 sites the derivation is as follows:

For a Cubo-octahedron:

$$C_7^5 + C_7^9 = 24(m-2) + 12(m-2)$$

Therefore, $C_7^5 + C_7^9 = 72\,; m = 4$

For a "cap" with m=4 the total number of $C_7^5 + C_7^9$ can be determined by counting sites in **Figure 16**:

Therefore, $C_7^5 + C_7^9 = 30\,; m = 4$

The ratio of cubo-octahedron to cap sites for m=4:

$$\frac{72}{30} = 2.4$$

Since the cubo-octahedron and cap scale by the same factor the concentration of C_7 sites can be determined by:

$$\text{Cap } C_7^5 + C_7^9 \text{sites} \simeq \frac{Cubo-octahedron\ C_7^5+C_7^9}{2.4} = \frac{24(m-2)+12(m-2)}{2.4} =$$

$$10(m-2) + 5(m-2)$$

From the calculations above the total surface sites on a cap can be approximated:

$$N_s \cong 9m^2 - 18m + 44$$

The diameter of "cap" can be approximated by the following. The diameter of a regular hexagon is double the length of its side. The base of a cap is an irregular hexagon but the diameter can be approximated by adding the length of two adjacent sides. For example, a cap of m=4 will have an adjacent side of 7 atoms. Therefore, the diameter is 11atoms wide. If an atom has a diameter of 0.28nm, such as in platinum, this corresponds to a

particle diameter of approximately 3nm. A Pt cubo-octahedron with m=4 would have a diameter of 2.5nm.

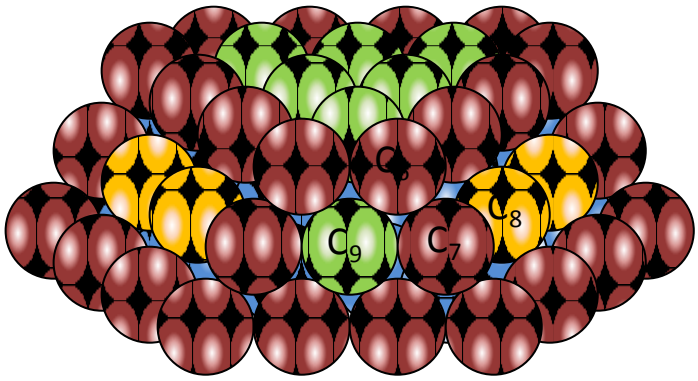

Figure 16. Truncated octahedron cap model.

CHAPTER III

CHARACTERIZATION AND REACTION STUDIES OF SILICA SUPPORTED PLATINUM MODEL CATALYSTS

Probing Terrace and Step Sites Using CO and Ethylene

Two of the most well studied adsorbates to date are CO and C_2H_4. Much work has been performed on the adsorption of CO and co-adsorption of CO and ethylene on the surface of low-index single crystals.[7,63,116-133] These studies have provided information on surface structure, charge transfer, and interactions between adsorbates. To a much lesser extent such interactions have been studied on supported catalysts and high-index surfaces.[125,134-136] Here, the influence of Pt particle size on the adsorption of CO and the co-adsorption of ethylidyne (derived from ethylene) and CO is studied. This analysis is extended to directly probe the percentage of highly-coordinated and under-coordinated atoms on the surface of Pt NPs. The results obtained from our adsorption measurements are compared to statistical estimates of surface sites based on simple geometrical models and arguments. This study represents a first effort to quantify the percentage of step and terrace sites simultaneously on the surface of Pt NPs as a function of Pt NP size using probe molecules in UHV. Pt in this sense allows for separation of step and terrace features in the CO adsorption/desorption spectra due to the strong variation in electronic structure at the step.[92,137,138]

Figure 17 displays three IRAS spectra each obtained at 300 K in a $P = 1 \times 10^{-7}$ Torr CO ambient on 2.6 nm Pt particles. As discussed in the experimental section,

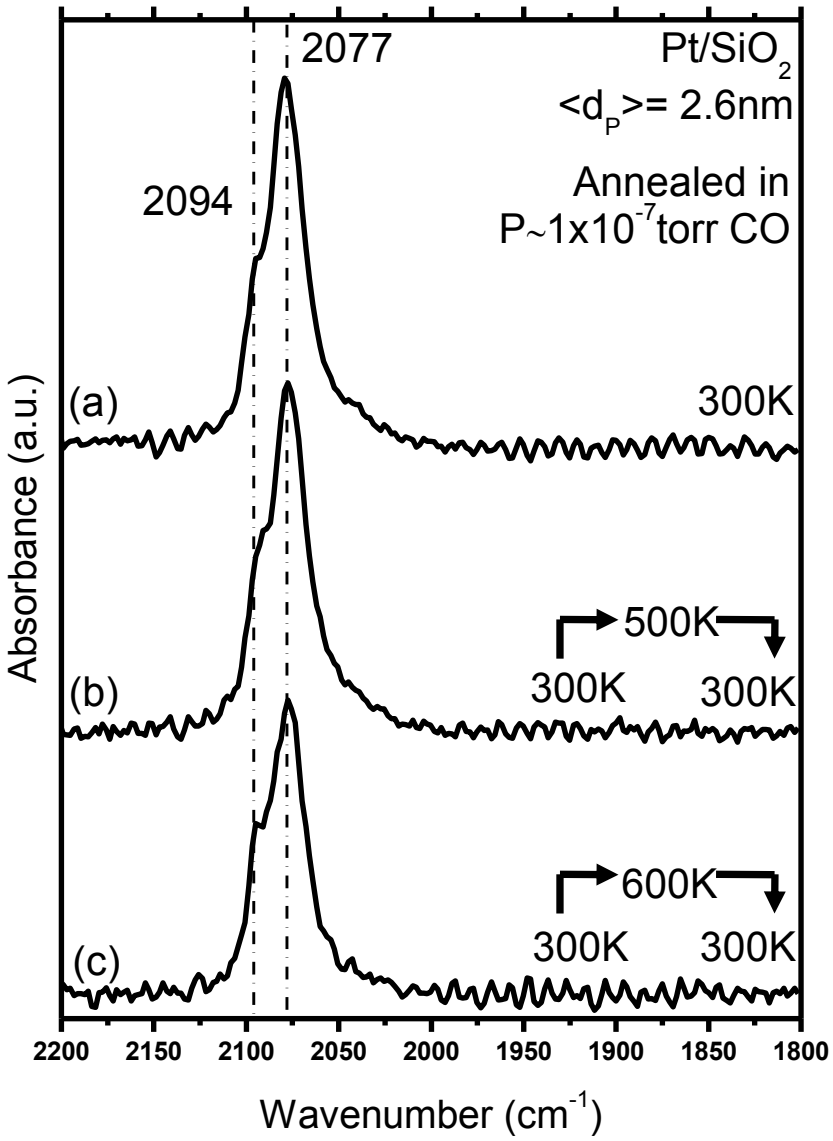

Figure 17. CO-IRAS of <dp> = 2.6nm Pt nanopariticles on SiO_2. All spectra were acquired consecutively at T=300K in a background of P=1x10^{-7}torr CO.[53] Spectrum (a) cooled from T=500 to 300K in CO, (b) annelased to T=500K in CO followed by cooling to 300K in CO, (c) annealed to T=600K followed by cooling to 300K in CO.

Pt/SiO_2 surfaces are prepared then cleaned in O_2 at 600 K to remove residual carbon. Spectrum (a) depicts cooling the surface in 1 x 10^{-7} Torr CO from 500 to 300 K after O_2 cleaning and represents a saturated CO surface at 300 K. Two features are present, one at 2077 cm^{-1} and another at 2094 cm^{-1}. As will be discussed shortly, these correspond to *step-like* and *terrace-like* adsorption sites on the Pt NP surface, respectively. The sample is then heated to the indicated temperatures of T = 500 K (b) and T = 600 K(c) in the above CO environment followed by cooling to 300 K in CO. All three spectra (a), (b), and (c) show approximately the same adsorption features and intensities indicating CO adsorption is reversible for both features under all three conditions. Additionally, these data illustrate that Pt/SiO_2 surfaces are essentially free of surface oxygen from the cleaning procedure, as indicated by the lack of CO stretching associated with Pt-oxide surfaces[139]; in other words, CO is adsorbed on metallic Pt NPs. Further analysis of the 2.6 nm particles is presented in the temperature dependent CO-IRAS data of **Figure 18**. A CO saturated surface labeled θ_{CO} = 1 was prepared by cooling from T = 500 to T = 300 K in P = 1 x 10^{-7} Torr CO as in **Figure 18** followed by complete evacuation to achieve UHV conditions (P < 10^{-9} Torr). From here, the IRAS spectrum was sequentially acquired at the indicated temperatures of **Figure 18**. The feature at 2094 cm^{-1} red shifts 9 cm^{-1} to 2085 cm^{-1} at a temperature of T = 320 K then disappears at a temperature of T = 375 K where only a single feature can be observed at 2060 cm^{-1}. Further heating leads to a shift to 2046 cm^{-1} at 425 K followed by complete desorption at T = 450 K.

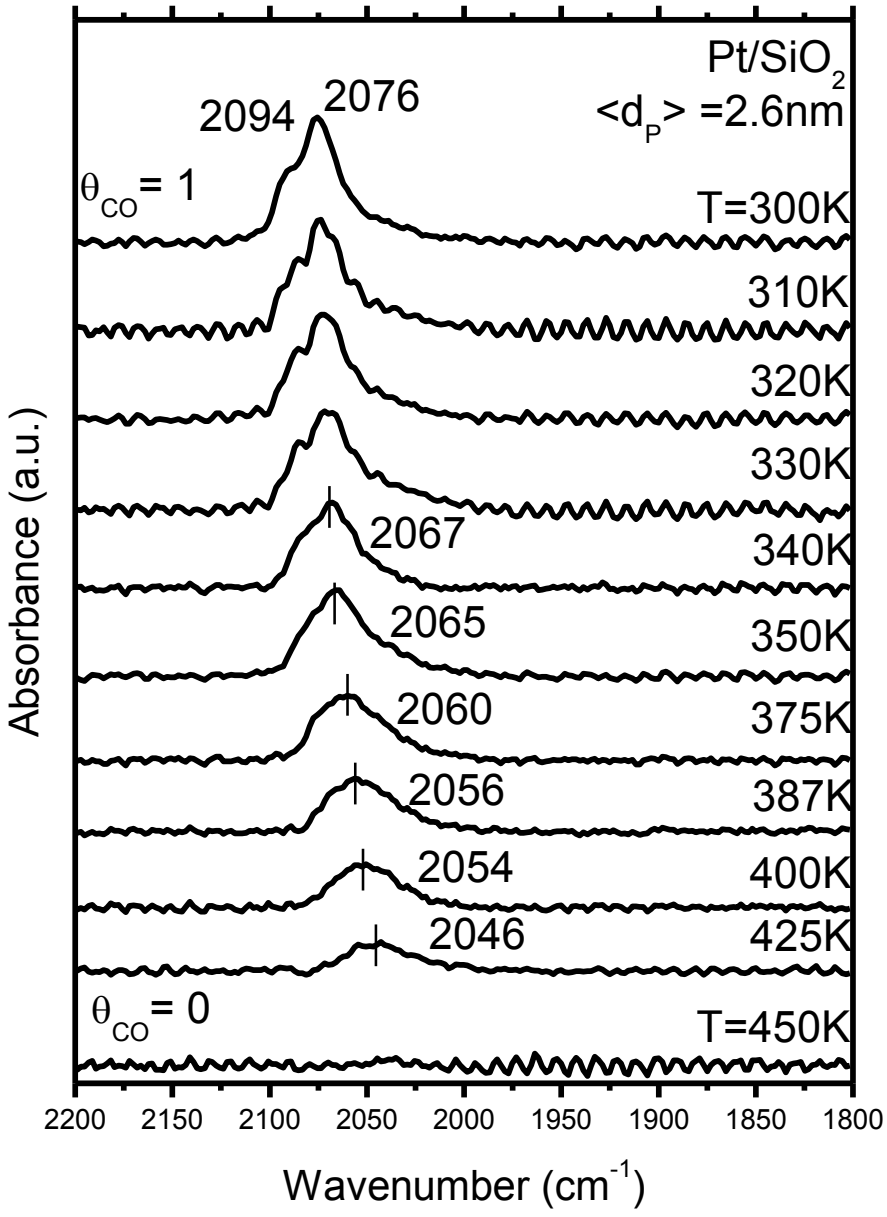

Figure 18. Temperature dependenct CO-IRAS on $<d_p>$= 2.6nm Pt nanoparticles. The sample was first cooled from T=500 to 300K in $1x10^{-7}$torr CO as in Figure 17 followed by evacuation to UHV and heating to the indeicated temperatures.[53] Θ_{CO} represents a maximum coverage of CO at T=300K in UHV.

Figure 19 shows NP size dependent (2.5 nm to >4 nm) CO-IRAS spectra each acquired at 150 K. Each surface was cooled from T = 500 to 150 K in P = 1 x 10^{-7} Torr CO followed by IRAS spectral acquisition in a P = 1 x 10^{-7} Torr CO environment; all features in **Figure 19** represent CO saturated surfaces. For clarity, the 2.5 nm, 2.6 nm, and 3.3 nm IRAS data have been multiplied by a factor of 10, 4, and 3, respectively. Two features are clearly visible at all particle sizes and qualitatively correspond to *terrace-like* (high-wavenumber) and *step-like* (low-wavenumber) adsorption. Upon increasing particle size, the *terrace-like* feature of the 3.3 nm particles increases in intensity and becomes approximately equal to the *step-like* feature. The *terrace-like* feature further increases and becomes the dominant feature for particles >3.3nm. A third feature on >4 nm NPs at 1850 cm^{-1} can also be observed (not shown). All three features qualitatively correlate to what has been observed on highly stepped Pt single crystals with particular emphasis to the Pt(112) and Pt(335) crystal planes[51,140-146] (discussed below) and can be qualitatively attributed to *terrace-like* and *step-like* adsorption.

The two distinct CO stretching features observed in CO-IRAS can be further explored with TDS as shown in **Figure 20**. **Figure 20** displays a saturation dose of ^{13}CO on 2.5 nm to > 4 nm NPs where two features develop with increasing NP size. On small NPs the first feature to develop is a high temperature one at 450 K followed by a low temperature feature at 350 K as the NP size increases. The feature at 450 K grows for increasing NP size and becomes saturated while the feature at 350 K continuously grows with an increase in NP size. A similar two-peak desorption profile was observed in thermal desorption spectra of CO from Pt(335)[51,140] and Pt(112)[51,145,146]. The high-

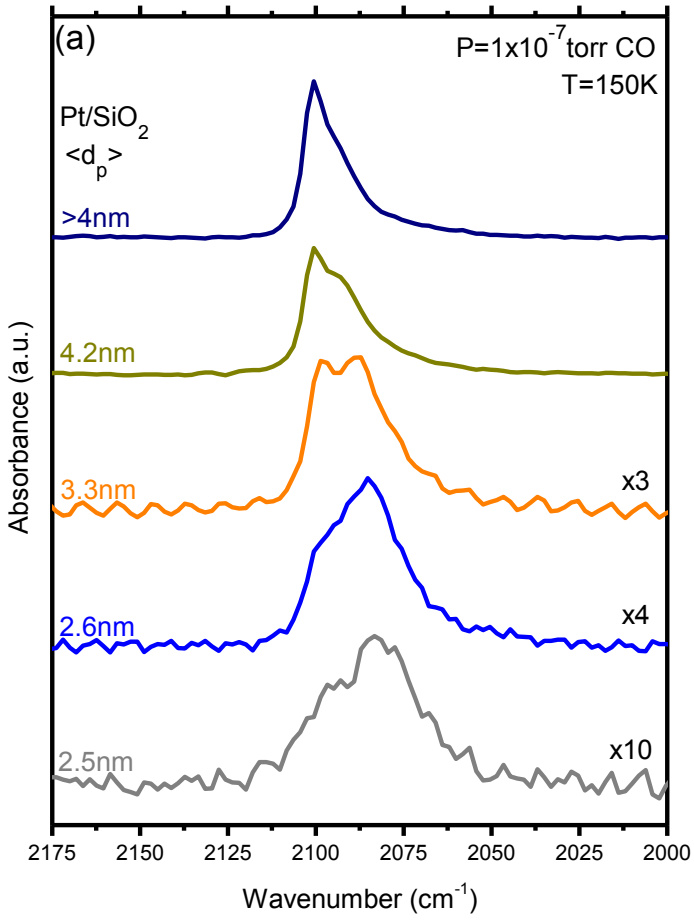

Figure 19. CO-IRAS spectra of Pt nanoparticles of varied size on SiO_2. Acquired at T=500K. Each surface was cooled from T=500 to 150K in $1x10^{-7}$torr CO and each acquired in a background of $1x10^{-7}$torr CO.[53] For clarity, spectrums $<d_p>$= 2.5,2.6, and 3.3nm have been multiplied by a factor of 10, 4, and 3 respectively. These data are also presented in Figure 22 for clarity.

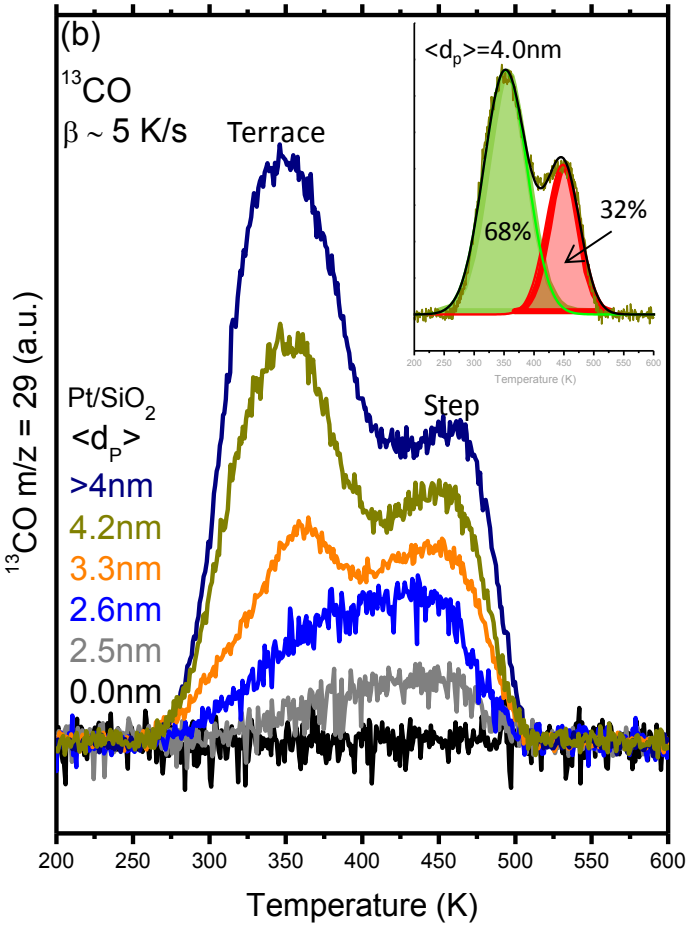

Figure 20. CO-TDS of Pt nanoparticles of varied size on SiO_2. Each surface was cooled from T=500 to 90K in P=1x10^{-7}torr CO followed by evacuation.[53] Each desorption profile has a heating rate of 5K/s/ The inset is an example of the Gaussian fit and deconvolution used to calculate the percentage of terrace sites plotted in Figure 25.

temperature feature can therefore be qualitatively assigned to *step-like* adsorption and the low-temperature feature to *terrace-like* adsorption (to be discussed). The profile of each spectrum in **Figure 20** was Gaussian fit and separated into *terrace-like* and *step-like* profiles (inset **Figure 20**). The area of the *terrace-like* feature for each particle size was normalized to the combined integrated area of its respective *step-like* and *terrace-like* features and plotted as % CO-TDS terrace sites (to be discussed below) with respect to NP size.

Freshly prepared NP surfaces were each exposed to a 20 L dose of ethylene at 300 K followed by cooling the surfaces in P = 1 x 10^{-7} Torr CO from T = 300 to 150 K. IRAS spectra were subsequently run on these Pt NPs and are presented in **Figure 21** where only the CO stretching region has been displayed. The step and terrace double-feature observed on the clean NPs in **Figure 19** is absent from the NP spectra of **Figure 21** and present only as a single-feature. This feature is red-shifted for NPs >2.5 nm with respect to both terrace and step features on the clean NPs. Moreover, **Figure 21** displays a red-shift that is dependent on size which can be more clearly seen in **Figure 22**. Both the clean and ethylene exposed NPs do, however, display a similar feature at 1850 cm^{-1} on NPs > 4 nm.

For TDS, each clean NP surface was exposed to 20 L of ethylene at 300 K followed by cooling in 1 x 10^{-7} Torr ^{13}CO to 150 K followed by evacuation. ^{13}CO-TDS spectra from the ethylene pre-exposed NPs of 2.5 nm and 4.2 nm are plotted against their clean NP profiles (from **Figure 20**) in **Figures 23 and 24**. Two CO desorption features are apparent and can be correlated to the two CO desorption features observed

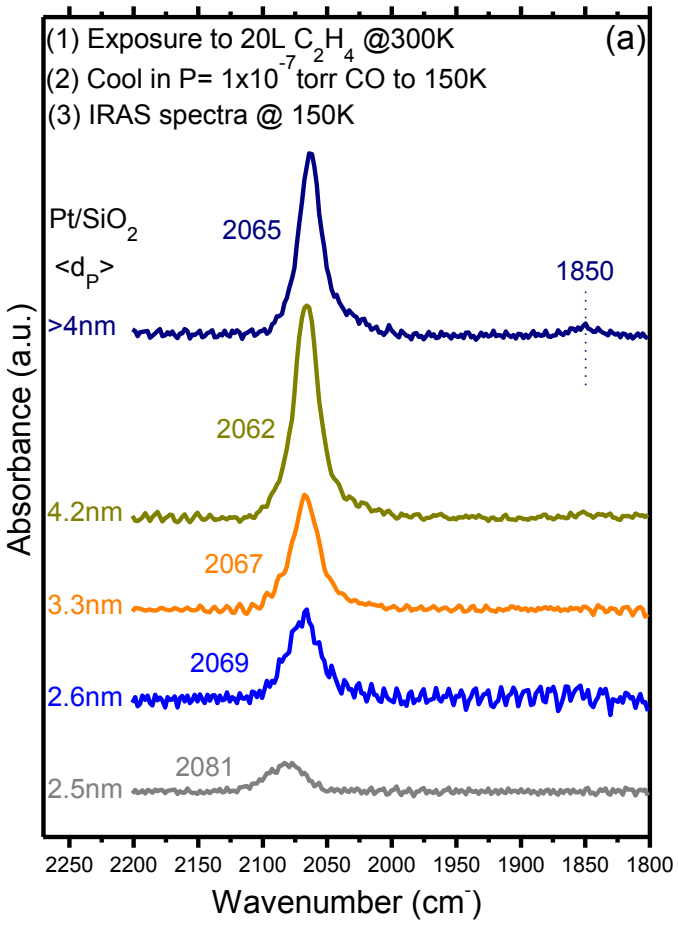

Figure 21. CO-IRAS spectra of Pt nanoparticles of varied size on ethylene pre-exposed surfaces. Each Pt/SiO_2 surfac was exposed to 20L of ethylene at T=300K to form ethylidyne followed by evacuation and then cooled from T=300 to 150K in P=1x10^{-7}torr CO.[53] All spectra were acquired at 150K in a background of P=1x10^{-7}torr CO. These data are also plotted in Figure 22 for clarity.

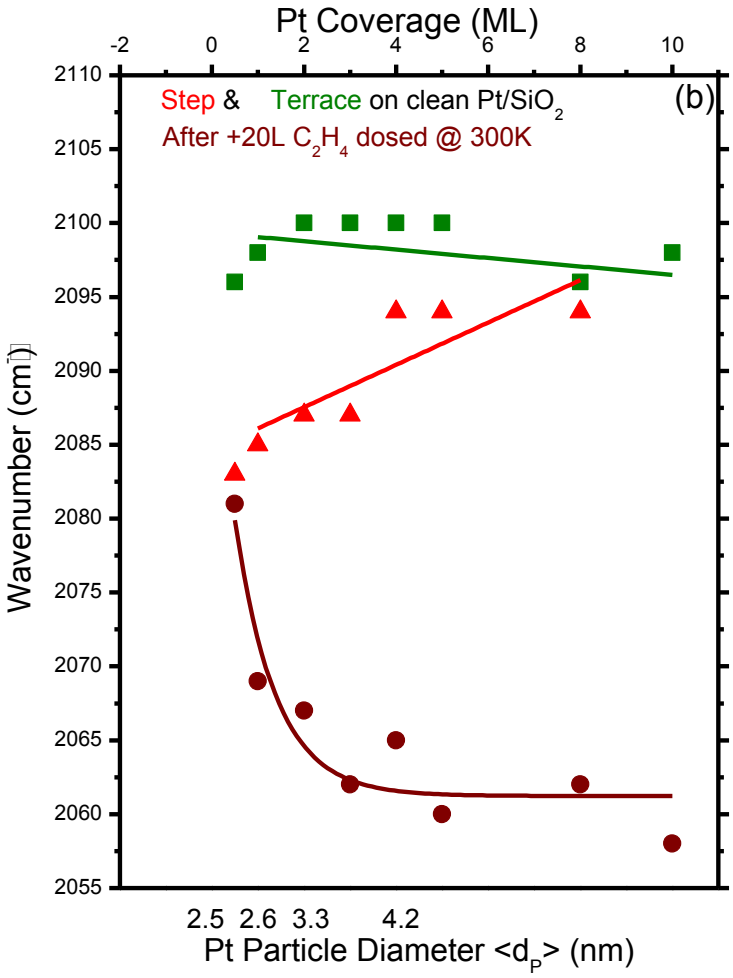

Figure 22. CO-IRAS wavenumber vs. Pt nanoprticle size for clean and 20L ethylene pre-exposed Pt/SiO_2 surfaces. Data points are acquired from Figures 19 and 21.[53]

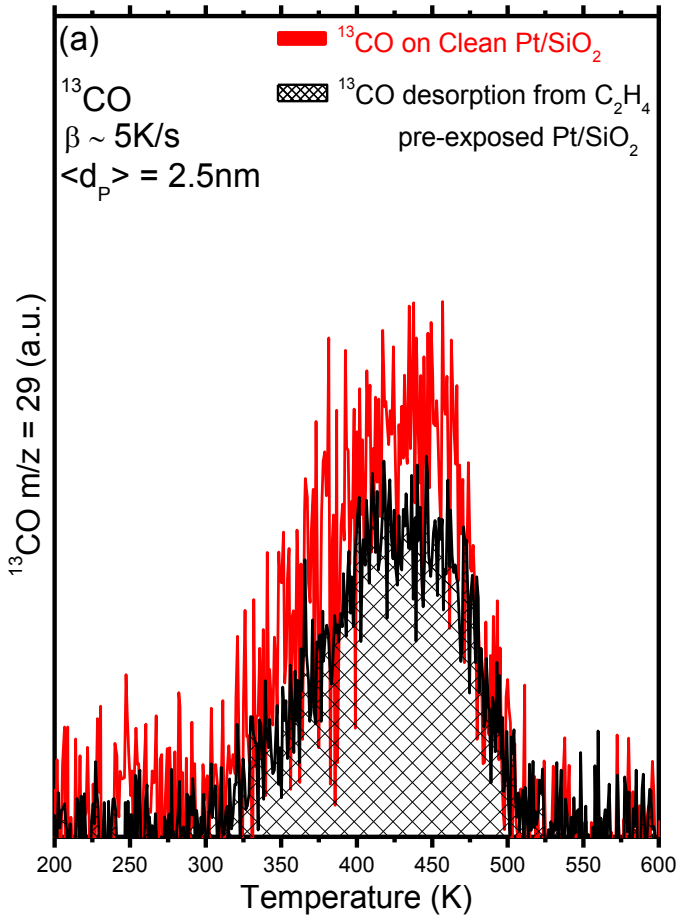

Figure 23. ^{13}CO-TDS from clean and ethylidyne covered nanoparticles of <d_p> =2.5nm. The Pt/SiO_2 surface was exposed to 20L of ethylene at 300K to form ethylidyne followed by evacuation, then cooling from 300 to 90K in P=1x10^{-7}torr in ^{13}CO.[53] The desorption profile has a heating rate of 5K/s. The area under the ethylidyne covered surface profile has been shaded for clarity.

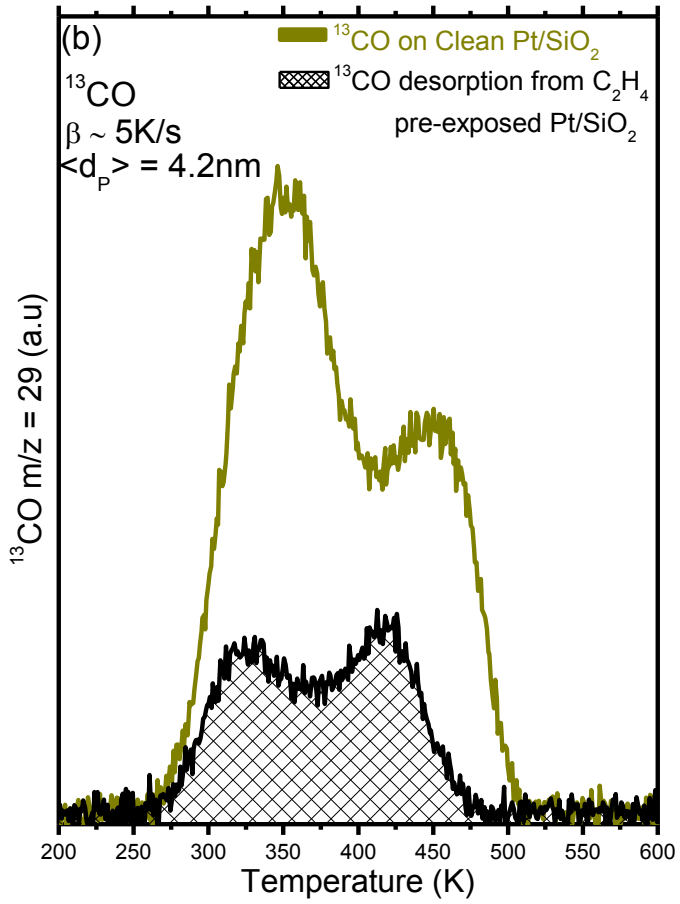

Figure 24. ^{13}CO-TDS from clean and ethylidyne covered nanoparticles of <d_p> = 4.0nm. The Pt/SiO_2 surface was exposed to 20L of ethylene at 300K to form ethylidyne followed by evacuation, then cooling from 300 to 90K in P=1x10^{-7}torr in ^{13}CO.[53] The desorption profile has a heating rate of 5K/s. The area under the ethylidyne covered surface profile has been shaded for clarity.

from the clean NPs (discussed later); these features are referred to as *terrace-like* and *step-like*, respectively. For >4.0 nm NPs (and all >2.5 nm NPs discussed later) each peak is attenuated when compared to their respective clean surfaces. The *step-like* feature on ethylene exposed 4.2 nm NPs have approximately the same intensity as the terrace feature. The leading edge of the desorption profile on ethylene pre-exposed surfaces matches that of the clean surface for all NP sizes. There is almost no change between the clean and ethylene exposed 2.5 nm TDS profile in **Figure 23**.

CO Adsorption

Pt NPs are known to grow spherical on SiO_2 and exhibit cubo-octahedral structures with (111) and (100) type facets.[49,147-150] Adsorption measurements presented in this paper indicate two desorption features in the CO-TDS profiles from Pt NPs, of which, a low temperature desorption feature is dominant on particles >3 nm. CO-TDS measurements on Pt(100)[146,151] and Pt(111)[146] low index crystal planes exhibit desorption profiles that are very different from Pt NPs as both crystals each reveal only one CO desorption feature. CO desorption from Pt(110)[129,146] reveals two features with the low temperature feature less intense than the high temperature feature. Kinked surfaces such as the Pt(321)[124] also do not have comparable CO desorption spectra to Pt NPs and will not be addressed at present. Only single crystals with a combination of (111) and (100) planes in correct proportions (discussed below) can provide a reliable means of indirectly assessing the structure of Pt nanoparticles grown on SiO_2 in UHV.

When the NP drops to 2.5 nm the terrace feature in the TDS becomes almost completely attenuated and step features become dominant (**Figure 20**). The trend in

TDS measurements indicate that the average ΔH_{ads} is enhanced on small Pt NPs. Indeed, experimental data for approximated ΔH_{ads} is shown to increase with decreasing size.[16,26] The result is caused by the increased density of step sites on the surfaces of smaller Pt particles, sites which bind CO more strongly than terrace sites. The step sites on larger particles (e.g. >4nm) compose <30% of the surface area and thus do not have a large contribution to the overall ΔH_{ads} value. The enhancement in ΔH_{ads} for small particles has also been shown to increase the activation energy for the CO oxidation reaction on small Pt particles (1.7 nm) on Pt/Al_2O_3 model catalyst surfaces.[26] An increase in ΔH_{ads} is also observed experimentally when comparing stepped Pt(210) to planar Pt(111); ~142kJ/mol and ~109kJ/mol, respectively.[146] From this data, it does not appear that the overall Pt NP size greatly affects the adsorption energy at a step, as indicated by an almost constant peak desorption temperature for a step site (**Figure 20**) for various Pt particle sizes. This would indicate that the increased ΔH_{ads} observed on small Pt NPs is not a unique aspect of Pt NPs alone and that it is simply a continuation of the intrinsic property observed on high index Pt single crystals.

At this point it is worth noting the similarities between our Pt/SiO_2 system and Pt NPs on other supports (i.e. Al_2O_3) and also with model and high surface area technical catalysts. Zafiris et. al.[26] were able to probe Pt/Al_2O_3 prepared in UHV and observed one CO desorption feature for an average particle size of 1.7 nm and two CO desorption features for a particle size of 14 nm consistent with step and terrace binding. Greenler et al. indicate $\upsilon(CO) = 2063\ cm^{-1}$ on a step for an average size range of $d_p = 4$ nm[152], similar to a step ($2065\ cm^{-1}$) on Pt(335)[140]. Our results in **Figure 18** show that a step site

with a vibrational feature at 2060 cm^{-1} for a particle size of 2.6 nm correlates well with these studies and that of other high surface area Pt/Al_2O_3 samples (2060cm^{-1} [153]). Similar IR results on technical Pt/SiO_2 catalysts with a size range of 5 – 15 nm display an absorption near 2050 cm^{-1} using transmission IR[154] which has also been observed on a commercial Pt/Al_2O_3 catalyst[155].

An excellent treatment concerning the effect of Pt-atom coordination on υ(CO) is demonstrated by the calculations of Brandt and Greenler et al.[156]. Data from the low coverage limit of CO on high-index crystals were used to assess singleton stretching frequencies of CO for a number of Pt surface-coordination-numbers assuming an "idealized" condition. It was determined that a linear correlation exists between Pt-coordination and υ(CO), consistent with reports of this effect from experimental data in the literature.[157] In a second paper the same authors were able to extend this analysis to Pt nanoparticles of cubo-octahedral geometry and to show a correlation in υ(CO) and IR-intensity between theory and experiment.[158] Calculations demonstrated dipole coupling shifts can depend on the in-phase and out-of-phase stretching modes of CO adsorbed on different regions and also on the concentration of CO in the ad-layer.[158] It then becomes obvious that assignment of υ(CO) from experimental data to a specific coordination-number on a NP is a difficult task because of the various factors which can potentially influence changes in υ(CO). For example, a Δυ(CO) can also be demonstrated for the 2.6 nm NPs by increasing the temperature from T = 300 to 340 K, $\Delta\upsilon(CO^{terrace}) = 9\ cm^{-1}$, or from T = 350 to 425 K, $\Delta\upsilon(CO^{step}) = 19cm^{-1}$, as in **Figure 18**. Increasing the temperature leads to an decrease in the CO-adlayer as observed by TDS and therefore

$\Delta\upsilon(CO^{terrace}) = 9$ or $\Delta\upsilon(CO^{step}) = 19$ cm^{-1} can be related to the dipole-dipole induced shift known to occur for CO adsorption on Pt.[159,160] **Figure 25** demonstrates that 60% of the surface area of 2.6 nm Pt NPs are consumed by step-sites (e.g. $C_{7,}$ C_6). It can be concluded that the remaining 40% of the surface has CO molecules bound to higher coordination sites (e.g. $C_{9,}$ $C^{4,5}{}_8$). Coupling between step sites of different coordination, step sites of identical coordination, step-terrace coupling, and terrace-terrace coupling are all known to effect $\upsilon(CO)$.[158] Therefore, experimental data concerning the magnitude of $\Delta\upsilon(CO)$ based on particle size and Pt-atom coordination at the surface is questionable.[134,157] Based on the results of **Figure 18**, the only estimate we can make with confidence with regard to $\upsilon(CO)$ and its' relation to Pt-atom coordination, is that the singleton $\upsilon(CO)$ on a step site must be below 2060 cm^{-1} in the size range of 2.5 nm. This is consistent with the calculations of Brandt and Greenler et al.[156,158]

For our IRAS data in **Figure 19**, with increasing average particle size the intensity of the *terrace-like* feature gains intensity while the *step-like* feature also gains intensity. This effect is not observed on stepped single crystals. On these crystals, the intensity of terrace CO species is enhanced at the expense of step CO intensity through dipole interactions.[107,159] This effect requires close proximity (r^{-3} dependence[6]) of the CO molecules in the ad-layer and can be inferred that in the absence of intensity sharing, CO must be on distinctly different particles (i.e. the overall intensity from step-only absorption in **Figure 19** is a combination of all particles in the size distribution). This emphasizes another limitation for direct comparisons between stepped single crystals and high surface area catalysts[155] (i.e. both model and technical particle systems can

exhibit *similar* spectra to single crystals although intensities and frequencies can be quite different). Other adsorption geometries such as bridging Pt_2CO at 1850cm^{-1} that have been reported on Pt(112)[51] and Pt(335)[51] single crystals are also observed on our >3.3 nm NPs (not shown). The nature of this species cannot be determined with confidence since terrace and step bridging CO are known to exist on both Pt(112) and Pt(335). CO bridging on the (100) crystal planes is also known to exhibit an absorption frequency in this region.[161]

CO and Ethylene Adsorption

It is well established that three prominent ethylene derived species can exist on Pt (i) π-bonded ethylene (Pt-C_2H_4), (ii) di-σ-bonded ethylene (Pt-CH_2CH_2-Pt), (iii) multiply bonded ethylidyne (Pt_3ΞC-CH_3).[17,64,130-132,134,136,160-165] In a UHV environment, the π and di-σ species are only formed at temperatures T < 250 K. The ethylidyne species forms at T > 250 K and can only be manifested on (111) crystalline terraces.[131,165] Measurements by a number of researchers on both Pt and other transition metals indicate ethylidyne to be the dominant species on the surface at T ~ 300 K.[7,17,130,131,133,135, 162-165] On our Pt particles, we observed the ethylidyne methyl symmetric mode $\delta_s(CH_3)$ at ~1340 cm^{-1} with IRAS on NPs > 3.3 nm at 300 K (not shown) in good agreement with literature values. Based on literature data which indicates CO adsorption can displace both the di-σ-bonded and π-bonded ethylene[136], we propose ethylidyne to be the only species on the surface. Our results in **Figures 21** and **23** show CO to be uninhibited on NPs of 2.5 nm indicating 2.5 nm NPs do not have the ensemble required to support ethylidyne under the present conditions. As the average particle size and *terrace-like*

sites increase the total surface concentration of ethylidyne also increases (**Figure 25** discussed below). A continuous red-shift in υ(CO) follows this trend that is opposite the effect of CO dipole-dipole coupling interactions which is known to blue-shift with increasing CO coverage on Pt-group metals.[159,160] From our data, it is not clear which interaction, Stark or charge transfer, between ethylidyne and CO is dominant.[7] Some insight can be gained from the results of **Figure 24** which indicate two CO-desorption features from the ethylidyne covered surface. For this, three facts are invoked from the literature (i) ethylidyne requires an FCC (111) ensemble[130,131,162-165] (ii) ethylidyne is stable between ~300 and 400 K[133,162] (iii) ethylidyne has a surface coverage of $\theta \sim 0.25$ on Pt(111) because of repulsive interactions between ethylidyne.[131,165] From these three facts, three arguments can be made concerning the nature of the two CO desorption features in Figure 5(b). First, the concentration of ethylidyne on the NPs must be limited due to repulsive interactions. Second, similarly with Pt(111) and Pd(111), the unoccupied terrace sites are still available for CO adsorption.[133,135] Third, step sites on NPs are also available for CO adsorption. As an example, the terrace feature from CO-TDS of the ethylidyne-covered NPs for various particle sizes is plotted along with CO-TDS from the terrace feature of clean NPs in **Figure 25**. Here, ethylidyne is shown to occupy ~18% of total sites on a surface containing 4.2nm NPs. This is less than the ~68% of *terrace-like* sites [(100) + (111)] shown to exist on clean 4.2nm NPs and indicates ~50% of terrace sites are still available for CO adsorption. Based on these data it can be inferred that both step and terrace CO are present on the ethylidyne-covered NPs and desorb as two separate features in the ^{13}CO-TDS (**Figure 24**). Since only one

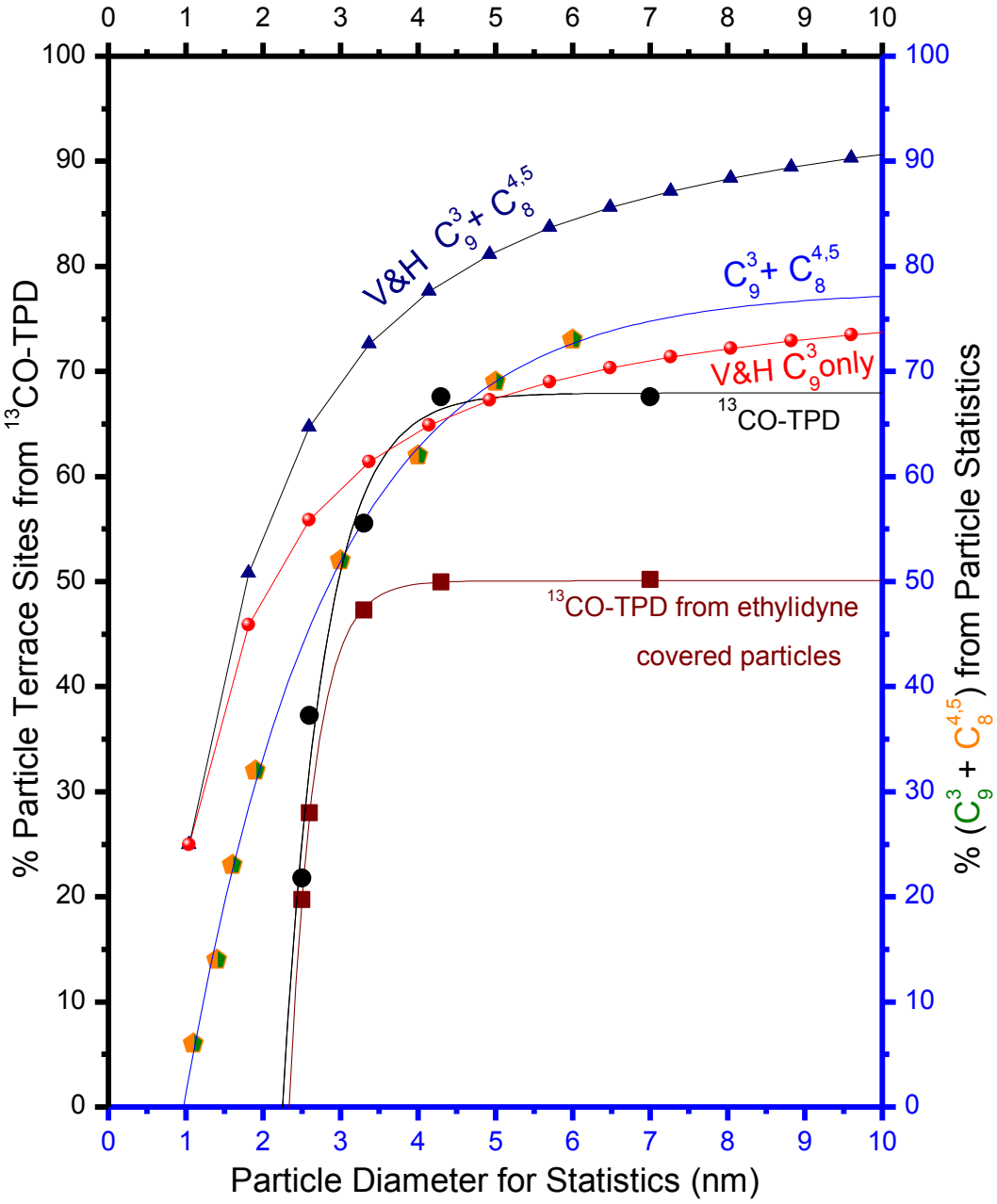

Figure 25. Percentage of terrace sites obtained experimentally from ^{13}CO-TDS on clean and ethylidyne covered Pt nanoparticles.[53] Also plotted is the percentage of terrace-like sites C_9 and C_8 sites from Figure 7 along with statistics from V&H. Particle size estimates are based on previous data obtained using STM. Error bares are obtained from the standard deviations ±σ of repeated measurements.

CO-IRAS feature is observed it can also be inferred that both step and terrace CO experience a similiar local environment on ethylidyne-covered NPs. As can be seen from the data of **Figure 21**, υ(CO) is relatively sharp and symmetrical for each particle size indicating the homogeneity of the adsorption sites. The effect of atomic hydrogen from ethylene decomposition on υ(CO) IR frequency on high-index Pt single crystals shows a repulsive behavior and the formation of compressed one-dimensional CO islands on the surface.[112,106] The hydrogen concentration is small considering the percentage of dissociated ethylene and the concentration of step sites and therefore should not have an appreciable effect on the CO stretching frequency. Possibly, charge transfer to the CO $2\pi^*$ anti-bonding orbital[106,166] becomes enhanced at a terrace site which shifts its absorption towards that of CO bound to step site. Dipole coupling between step and terrace CO gives rise to an intense symmetrical feature. Au clusters are also shown to have an effect where two CO desorption features can be present in CO-TDS but show only one IR absorption.[126] Interestingly, a feature at 1850cm^{-1} which can be related to a bridging CO species (Pt_3-CO or Pt_2-CO) is present on >3.3 nm NPs and is unaffected by the presence of ethylidyne. Possibly, this species may also exist for smaller Pt particles but the concentration may be below the detection limit of our current IRAS setup. On Pt(112), bridging CO forms for high CO concentrations on both terrace and step atoms. It would appear that the sites occupied by υ(CO) = 1850cm^{-1} on a Pt particles are not active in the formation of ethylidyne as would be expected based on the results from stepped crystal planes.

In **Figure 25** we make a quantitative estimate of the amount of surface covered with ethylidyne by performing ^{13}CO-TDS on the Pt NPs before and after exposure to ethylene at 300 K. **Figure 25** shows the percent terrace from both the terrace sites obtained from the TDS profiles of **Figure 20** and the percentage of available terrace sites after exposure to ethylene. For reference we utilize a calculation for a truncated cubo-octahedron cap of ~4nm which has a surface area of consisting of 237atoms of which 93 atoms have (111) C^3_9 coordination. Based on Pt(111) which exhibits an ethylidyne ($Pt_3\Xi C\text{-}CH_3$) saturation of ~25%[131] our 4nm model particle can accommodate ~8 ethylidyne species. Experimental results in **Figure 25** demonstrate ethylidyne to block approximately 18% of a surface covered with 4nm particles. Our Pt/SiO_2 samples with particle sizes in the range of ~4 nm (4 ML Pt) are shown to exhibit 8.1 x 10^{14} total surface sites per cm^2 based on our previous studies[11] of which ~68% are terrace (**Figure 25**). Knowing our approximated surface density of particles ~8.9x10^{12} per cm^2, and assuming a narrow size distribution we can estimate the number of ethylidyne per 4nm NPs to be ~4 ethylidyne molecules. This is in fair agreement with the ~8 ethylidyne molecules estimated from a 4nm model-particle calculation. As the average particles size decreases, the total effect of blocking terrace-sites by ethylidyne decreases. This becomes most apparent for a surface with an average particle size of 2.5 nm as both the CO IRAS and TPD profiles do not change after exposure to ethylene (**Figure 21 and 23**). Also presented in **Figure 25** are the site estimates for C^3_9 + $C^{4,5}_8$ and C^3_9 -only terrace sites on the surface of cubo-octahedrons of various sizes from V&H[49] along with our counting model labeled "cap C^3_9 + $C^{4,5}_8$" from **Figure 7**. It is easily observed that if

the V&H[49] model takes into account both C^{3}_{9} and $C^{4,5}_{8}$ sites an overestimate is made from the experimental data. If only C^{3}_{9} sites are assumed then the V&H[49] model approaches the TDS results for >3.3 nm NPs but begins to fail while moving to smaller NPs. The main reason for this deviation is that the V&H[49] model is based on completed cubo-octahedron (111) crystal planes. The truncated cubo-octrahedron "cap" model, which takes into account both C^{3}_{9} and $C^{4,5}_{8}$, provides a better fit to the experimental data but deviates for NPs >4 nm. These results suggest that NPs between 2.5 - 3 nm exhibit a higher concentration of (100) sites and that (111) sites begin to dominate as the particle size increases to 4.2 nm and greater.

Summary

Platinum NPs display both terrace and step features in the CO IRAS and TDS spectra that are comparable to Pt(112) and Pt(335) high index crystal planes but not with Pt(110), Pt(111), or Pt(100) low index crystal planes. Statistics and experimental results presented here and in the literature demonstrate that Pt NPs begin to deviate from Pt(112) and Pt(335) surfaces as the particle size drops below 4 nm. Despite this behavior, the assignment of terrace and step CO in IRAS and TDS spectra remains valid as NPs become smaller than 4 nm. Separation of terrace and step features in the CO-TDS profiles allows the percentage of terrace-sites on Pt NP of varying size to be determined experimentally. As the NP size decreases from 4.2 - 2.5 nm the terrace feature in the CO-TDS decreases by 50%. The most drastic change in Pt NP terrace sites, C^{3}_{9} and $C^{4,5}_{8}$, occurs between 2 and 3 nm, and correlates with statistical arguments by V&H[49].

Ethylidyne (derived from ethylene) was employed as a terrace blocking species. Post-adsorption of CO was investigated by IRAS on ethylidyne-covered NPs and displayed an intense symmetrical CO stretching feature which is red-shifted relative to clean NPs. CO continues to red-shift $\Delta\upsilon(CO) \sim 20$ cm^{-1} as the NP size is increased from 2.6 to 4.2 nm. This single feature, although having approximately the same frequency as CO on a clean NP step-site (~2060 cm^{-1}), cannot be associated with step-only adsorption as indicated by the two CO desorption features in their respective TDS profiles. It can be inferred that both terrace and step sites experience a similar environment on ethylidyne-covered Pt NPs since only one CO stretching feature but two CO desorption features are observed. Exposure of ethylene to NPs <2.6 nm has no effect on CO adsorption. This demonstrates ethylidyne formation is inhibited on Pt NPs <2.6 nm. TDS of CO from ethylidyne-covered NPs was also used to determine the concentration of ethylidyne from a surface with an average particles size $<d_p>$ = 4.2 nm. This was estimated, based on our NP surface density and size distribution estimates from our previous results[11], to be between ~4 - 8 ethylidyne molecules per nanoparticle. This investigation demonstrates a direct correlation between numerical values of site concentrations on Pt nanoparticles from experiment and theoretical-models. These results can now be used to correlate active-site concentrations on Pt nanoparticles to selectivity data obtained from elevated pressure reactions in ongoing fundamental investigations being conducted in our laboratory.

CO Oxidation

CO oxidation on Pt-group metal single crystal surfaces, under similar reaction conditions, have demonstrated that under elevated pressure conditions (pressures approaching 1 atm and CO dominant surface conditions) and relevant catalytic temperatures (T = 450 - 625 K), the CO oxidation reaction on Pt-group metals (Rh, Pd, Pt) exhibits structure insensitive behavior; i.e. observed catalytic activity is largely independent of the underlying crystal structure.[68-70,167-169] This is supported by good agreement between single crystal studies and technical catalyst studies under similar O_2/CO and temperatures.[68-70,167-169] Under CO-rich conditions (e.g. lower O_2/CO conditions or lower temperatures), CO_2 formation is believed to be rate limited by the CO desorption step, as CO blocks sites for O_2 adsorption and dissociation.[177] Data obtained from model and technical catalyst studies of supported Pt have illustrated that, under CO-dominant reaction conditions (O_2/CO ratios near or below stoichiometric) at elevated pressures, CO oxidation kinetics exhibits little dependence on particle size for Pt particles with average particle diameters (dp) > 2 nm.[70,170-172] Under such conditions, the reaction is rate limited by CO desorption, which blocks sites for O_2 adsorption and dissociation. Particles with sizes greater than 2 - 3 nm, generally consist of terrace sites, as shown by simple hard sphere models; the concentration of step sites shows little dependence on particle size after d_p =3 nm.

Under conditions which facilitate higher O_2 coverages (e.g. high O_2/CO conditions or high temperatures), CO_2 production rates have been reported to exhibit structure sensitivity. The existence of structure sensitive behavior has been supported by

measurements probing high temperature and/or high O_2/CO conditions on Pt technical catalyst samples[171-177], and has been observed in low pressure measurements[28,178-180] of Pt-group metal single crystal and model catalyst surfaces. The reactivity and nature of Pt-group metal surfaces under high O_2/CO conditions at elevated pressures has been the subject of recent debate and remains an active area of study.[60,62,72, 113,181-184] Similarly, as particle sizes become very small (d_p < 2 nm), structure sensitivities can also arise in CO oxidation kinetics, as observed in studies of Pt model catalyst[16,26,27] and Pt technical catalyst surfaces[171-173]. Studies by Gorte and coworkers[26] have demonstrated that smaller particles (1.7 nm Pt/Al_2O_3) are observed to exhibit lower CO oxidation rates (with Ea = 178 kJ/mol) than larger particles (14 nm Pt/Al_2O_3) (with E_a = 125 kJ/mol). This observation is correlated to the increased binding of CO on smaller particles (< 2 nm), which contain a high fraction of CO bound to Pt step sites which have a larger desorption energy than terrace sites, thus affecting CO oxidation kinetics in the desorption limited regime.[16,27,53] This observation is consistent with expectations from simple hard sphere models, which predict that the number of step:terrace atoms on the surface of a close packed particle should sharply increase below 2 - 3 nm; above particle sizes of 3 nm, the ratio of step:terrace surface atoms is less strong.

As discussed below, Pt/SiO_2 model catalyst surfaces are characterized and run under under elevated pressure reaction conditions (approaching 1 atm) using CO oxidation reaction kinetics under CO-dominant conditions. These conditions are used to test the efficacy of CO oxidation as a probe for determining the concentration of total surface sits under high pressure conditions. The data are compared to data obtained on a

Pt(110) surface under identical reaction and reactor conditions. The results demonstrate the utility of model catalyst samples in providing quantitative and qualitative reactivity data at elevated pressures, and can serve as a useful benchmark for future work on more complicated systems.

Shown in **Figure 26** are reactivity measurements [molecules CO_2 formed/sec vs 1000/T(K)] obtained from a series of Pt/SiO_2 model catalyst samples with varying Pt coverage (θ_{Pt} = 1 through 10 ML) using a (1/2) O_2/CO gas mixture, along with data obtained from the Pt(110) single crystal. Control reactivity experiments were conducted on prepared SiO_2 films (without Pt) and show negligible CO_2 production, indicating all CO_2 production arises from the deposited Pt particles. As expected, CO oxidation rate increases as the Pt coverage (and hence number of available reaction sites) is increased. Arrhenius plots (dashed lines) for the Pt/SiO_2 exhibit similar activation energies (E_a = 110 ± 10 kJ/mol), and are in general agreement (E_a comparable to CO desorption energy) with values observed in previous studies of Pt single crystal[62,169], Pt particle[7,10] and other Pt-group metals under CO rich reaction conditions[66-68,169]. Experiments conducted with the (1/2) O_2/CO mixture under the temperature conditions shown in the **Figure 26**, demonstrated repeatable behavior (i.e. samples could be run repeatably throughout the temperatures ranges with negligible changes to the measured reaction rate) indicating that reaction induced deactivation of the particles are not occurring under these conditions. Replicate measurements indicate a typical error of ±10% in the reported rate values. Normalization of Pt/SiO_2 and Pt(110) data of **Figure 26** provides a method to estimate the number of active Pt sites on Pt/SiO_2 samples as a

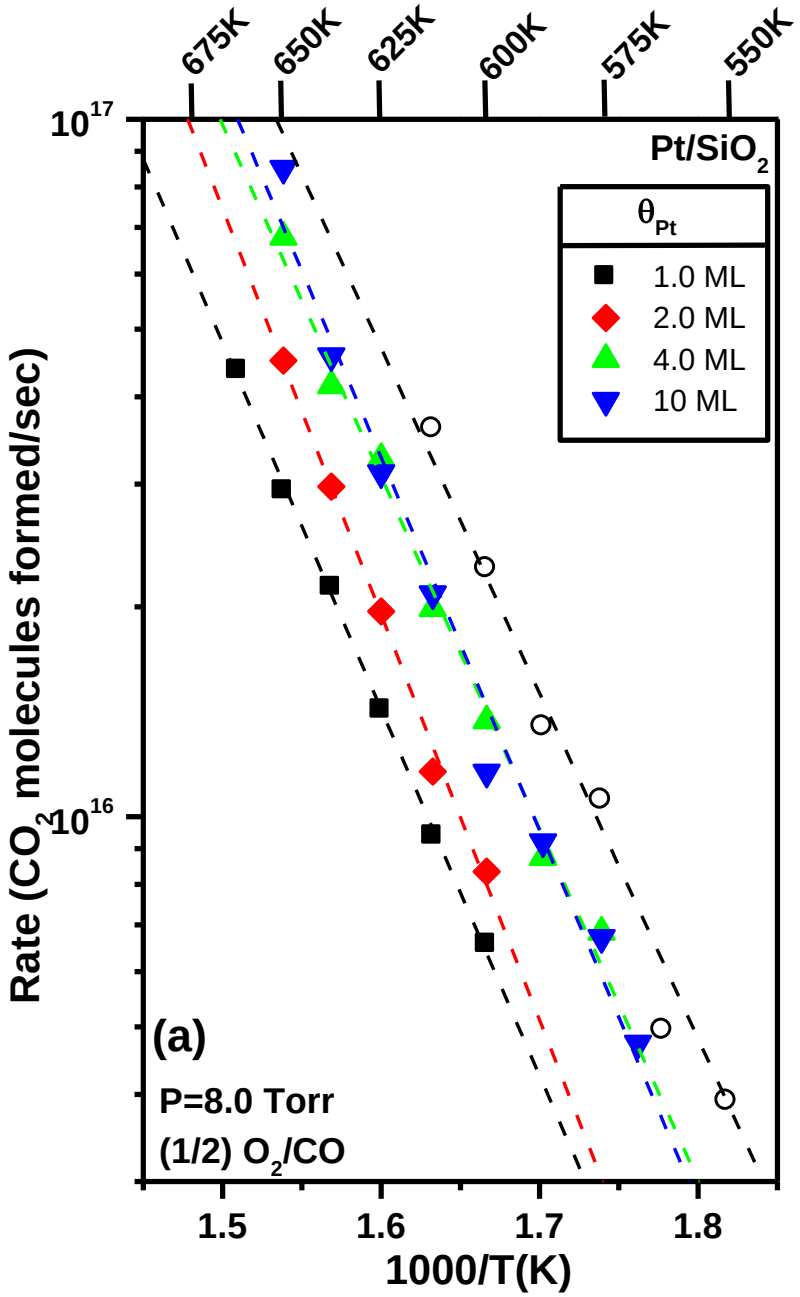

Figure 26. CO_2 reaction data, (CO_2 molecules formed/sec) vs. 1000/T(K), for various Pt coverages (θ_{Pt}) on Pt/SiO_2 model catalyst samples. Typical error in reactivity measurements, based on replicate measurements, is ±10%.[11]

function of θ_{Pt}, under elevated pressure conditions (Pt(110) surface density = 9.2 x 10^{14} atoms/cm^2).[12] This exercise is visualized in **Figure 27**, which is an Arrhenius plot of the data of **Figure 26** in terms of TOF, where Pt/SiO_2 reactivity data for the various coverages has been normalized by a linear least squares fit. The number of sites obtained from normalization are shown in the figure for the coverages (θ_{Pt} = 1 through 10 ML). (Note: Pt particles are deposited on only one side of the SiO_2/Mo(112) sample).

Figure 28 presents reactivity data (TOF) for the 2 ML Pt/SiO_2 surface and the Pt(110) surface as a function of gas mixture (O_2/CO). Reactions are run for gas mixtures (2/1), (1/1), and (1/2) at a pressure of P = 8.0 Torr. Site estimates obtained from **Figure 27** for the 2 ML Pt/SiO_2 surface (2.8 x 10^{14} Pt sites) is used for normalization. Reactivity measurements were repeatable throughout the reaction temperatures explored; replicate reactivity measurements exhibit the typical spread obtained in reactivity data (typically ± 10%). Normalizing data for the (1/2) to (2/1) gas mixtures by the number of Pt sites obtained from **Figure 27**, TOF data agree well with data obtained on the Pt(110) single crystal. Additionally, results illustrate that reactivity increases with increasing (O_2/CO), consistent with the well-known behavior of CO oxidation on Pt-group metals in the CO rich regime[62,66-70,169] (i.e. positive order dependencies in O_2, and negative order in CO). Increased O_2 partial pressure increases the amount of O_2 adsorption and dissociation on the surface, aiding reaction. These observations show that, under the O_2/CO reaction mixture conditions utilized, the observed kinetic behavior is consistent with a reaction occurring on a primarily metallic, CO inhibited Pt surface.

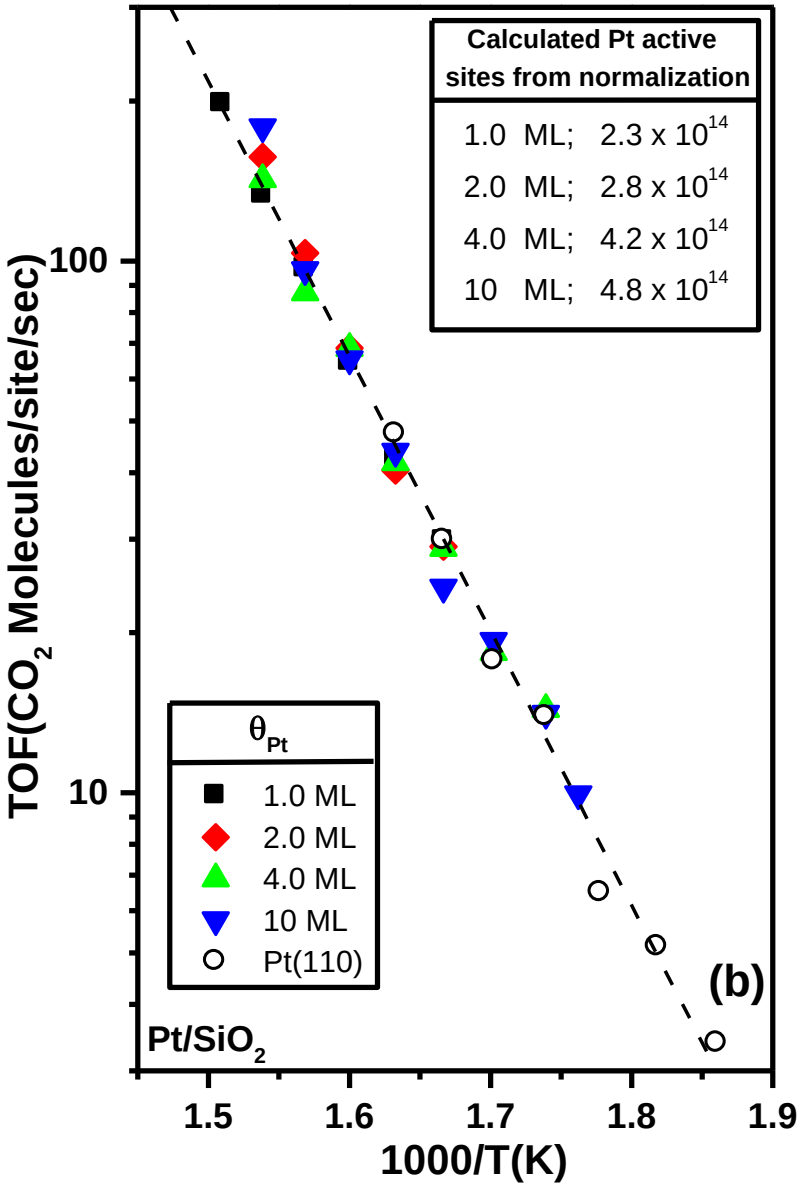

Figure 27. Data from Figure 26, normalized to Pt(110) to give CO_2 reaction data, (CO_2 moleculesformed/site/s) vs. 1000/T(K), for various Pt coverages (θ_{Pt}) on Pt/SiO_2 model catalyst samples. Typical error in reactivity measurements, based on replicated measurements, is ±10%.[11]

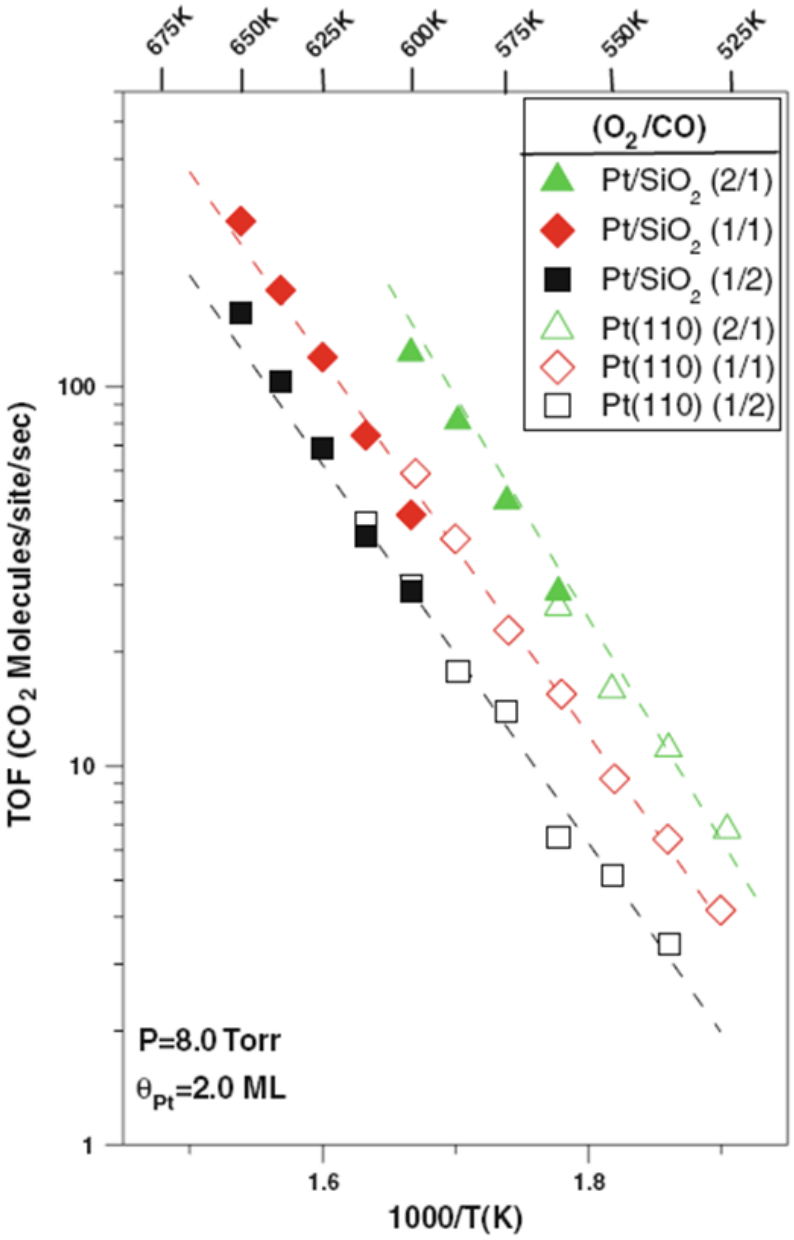

Figure 28. CO_2 reaction rate data (TOF (CO_2 molecules formed/site sec)) vs. 1000/T(K)) performed for various O_2/CO gas mixtures over a Pt/SiO_2 surface with 2ML Pt coverage. Shown as open symbols are corresponding reaction data taken on Pt(110) single crystal sample. Data is normalized using the number of site estimate obtained for θ_{Pt} = 2.0 ML coverage in Figure 1(b) (2.8 x 10^{14} Pt sites). Typical error in reactivity measurements, based on replicate measurements, is ± 10.[11]

STM and CO TPD data were collected in order to provide an additional measure of the number of active sites present on the Pt/SiO_2 surfaces and to provide information on Pt particle size under low pressure conditions. STM images were collected on Pt/SiO_2 samples as a function of Pt coverage (θ_{Pt} = 0.5, 1, 2, and 4 ML Pt) in a separate STM/UHV system. **Figures 29** shows a representative STM image of a 1 ML Pt/SiO_2 surface (100 x 100 nm image). **Figure 30** shows average particle size, d(Å), obtained from all Pt/SiO_2 measurements, along with the minimum and maximum particle sizes observed for each coverage. Error bars represent standard deviation of d(Å) from image histograms. Particle height measurements have also been obtained (with corrections for tip effects), to obtain aspect ratio measurements of the Pt particles. Z-height measurements indicate the as-deposited Pt particles have average aspect ratios of ~ 0.3. Using aspect ratio measurements, particle size and distribution statistics, an estimate of Pt sites/cm^2 can be obtained using geometric arguments, assuming hemispherical cap shaped particles; a complete description of this exercise can be found in ref. 12. The result of this calculation is shown in **Figure 31** (▲ symbol). This site estimate assumes that the surface atom density of the particles are that of the Pt(111) facet (1.5×10^{15} Pt atoms/cm^2). As this assumption will likely overestimate the number of sites present on the particles, we have also calculated site estimates based on Pt(110) (9.2×10^{14} Pt atoms/cm^2; Δ) and Pt(100) (1.3×10^{15} Pt atoms/cm^2; --Δ--) surface atom densities, facets which expected to be associated with particle surfaces.

Shown in **Figure 31** is a plot of number of Pt active sites per cm_2 as calculated from the TPD measurements, STM, and reactivity data. As the data of **Figure 31**

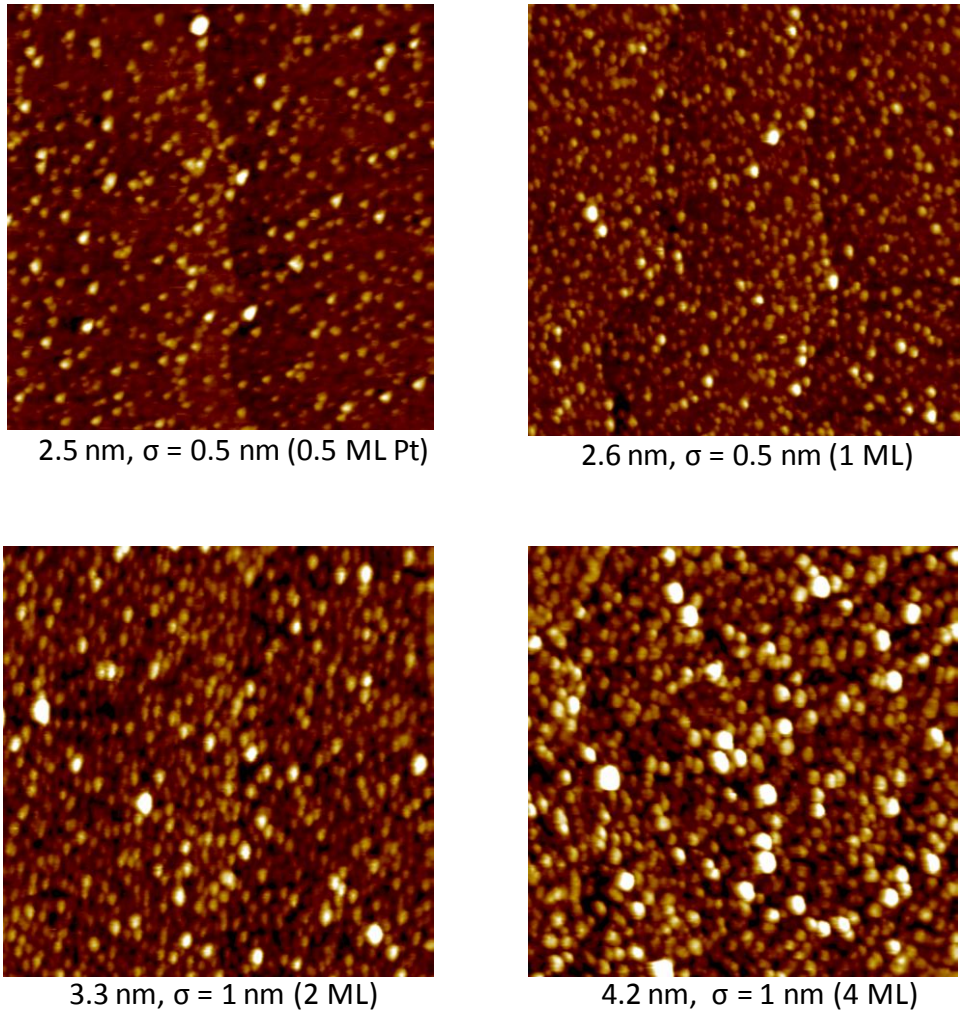

Figure 29. STM of Pt/SiO_2 for various Pt coverages. Images 100 nm x 100 nm.

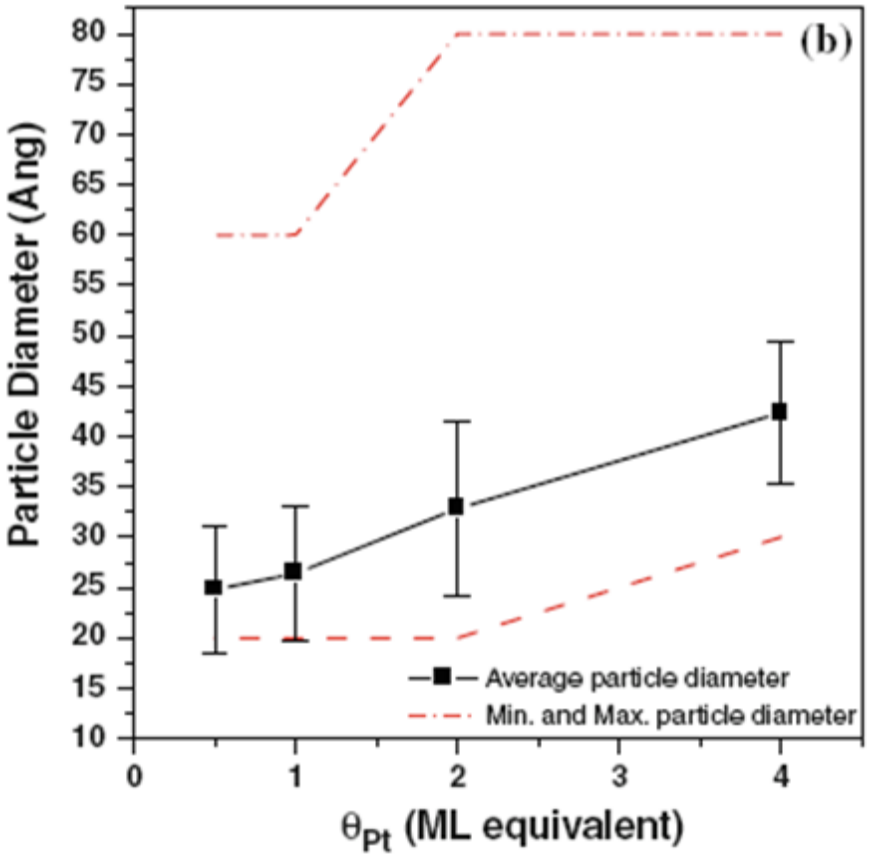

Figure 30. Particle size vs. monolayer coverage obtained from STM. Average particle diameter (in Angstroms, Å) (■) and standard deviation (error bars; ±σ), as determined from histogram data obtained from STM images (θ_{Pt}=0.5 ML through 4.0 ML). Shown by dotted lines (-----) are the minimum and maximum Pt particle diameter observed for a given θ_{Pt}.[11]

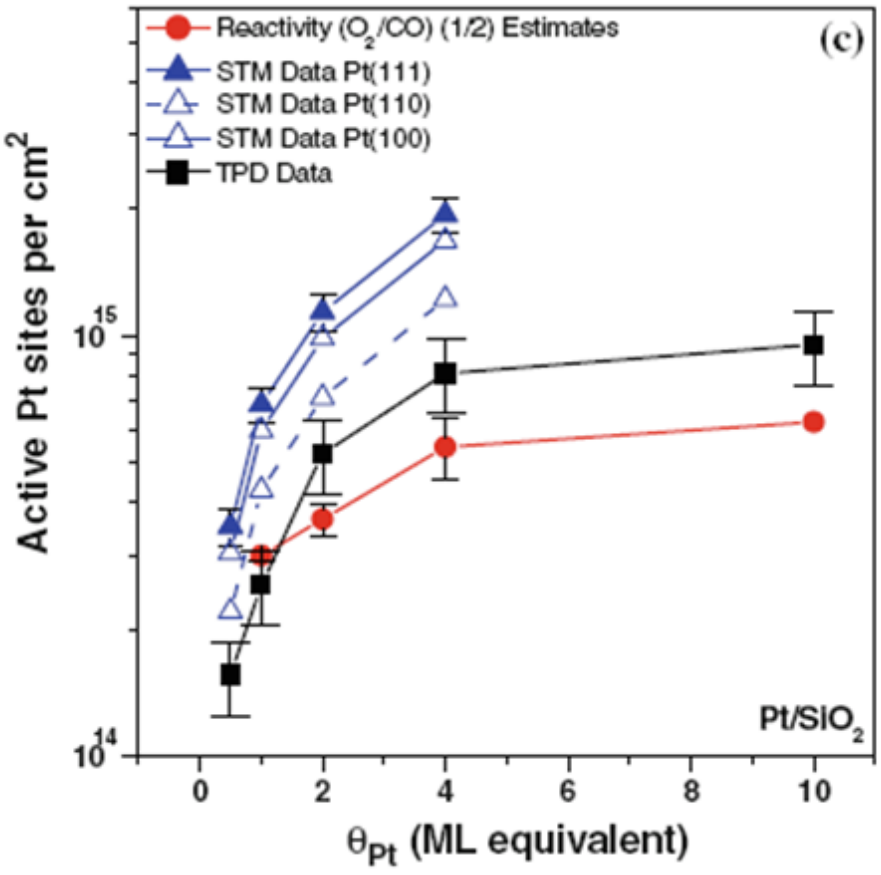

Figure 31. Number of active sites per cm^2 vs. θ_{Pt} (ML equivalent), as estimated from CO-TDS, (1/2) O_2/CO reactivity data, and STM data. [(▲), assuming Pt(111) surface atom density (1.5 x 10^{15} Pt atoms/cm^2); (Δ) assuming Pt(100) surface atom density (1.3 x 10^{15} Pt atoms/cm^2); (--Δ--)assuming Pt(110) surface atom density (9.2 x 10^{14} Pt atoms/cm^2)]. Characteristic error bars for the data sets, shown for reference, are discussed in text.[11]

illustrates, Pt site measurements from the various techniques show agreement. However, as shown by the data, slight differences can be observed between the level of agreement of the different methods. Better agreement is achieved between CO TPD (■) and reactivity estimates (●); both are methods which provide a direct experimental measure of active surface sites available for CO adsorption. STM data (▲), on the other hand, appears to predict a higher number of sites than the reaction and TPD measurements. It is postulated this could be due to assumptions made in estimating active sites via this geometric method. Such a simplifying assumption will likely provide an overestimate of the number of active sites for particles. As shown in **Figure 31**, site estimate calculations employing Pt(100) (Δ) and Pt(110) (--Δ--) surface atom densities (facets more characteristic of smaller particles) begin to approach the reactivity and TPD data to provide better quantitative agreement. This exercise illustrates the errors associated with the simplifying assumptions employed in analyzing the STM data. We speculate that the quantitative disagreements between and the STM and the TPD/reactivity methods could simply arise from these simplifying assumptions associated with the geometric STM estimation method. Regardless, a general agreement is achieved with the various estimation methods, with all methods tracking well with one another with increasing Pt coverage. This is surprising, considering the ~10^{10} order of magnitude difference in pressure range over which the characterization measurements were taken (STM, CO TPD measurements: P = 10^{-10} Torr; CO oxidation reactivity measurements: P = 8 Torr). In this sense, careful reactivity measurements of CO oxidation (conducted under rich CO

gas mixtures) can provide a reasonable method to measure Pt active sites from TOF values obtained under elevated pressure conditions.

STM measurements of the Pt/SiO_2 samples in the present study indicate that the Pt/SiO_2 samples used in our reactivity measurements ($\theta_{Pt} \geq 1$ ML Pt/SiO_2) have average diameters larger than d_p = 2.6 nm (**Figure 30**); for particles of this size range, the particle surface is primarily dominated by terrace adsorption sites. Similarly, CO TPD and CO-IRAS data demonstrate that for surfaces $\theta_{Pt} \geq 1$ ML Pt/SiO_2, the ratio of step to total adsorption Pt sites does not substantially change much as a function of θ_{Pt} (only changing by ~20% from θ_{Pt} = 1 ML to 10 ML)[29]; for such a small dependence (and considering the error in our reactivity measurements ±10%), it is probably unlikely any noticeable particle size dependence would be observed in CO oxidation kinetics on the Pt/SiO_2 samples of the present study, consistent with our reactivity results. The largest changes in step adsorption sites[53] occur as particles decrease below d_p = 2.5nm (below θ_{Pt} = 1 ML) in agreement with expectations.[49] Secondly, the activation energies across the Pt coverages studied, exhibit similar activation energies (E ~ 110 kJ/mol), demonstrating no dependence on particle size and consistent with reaction occurring on a Pt terrace site. Attempts were made to run reactions on surfaces containing $\theta_{Pt} < 1$ ML Pt/SiO_2 to probe this region of highly dispersed particle sizes (< 2.5 nm); however, rates were too slow to reliably measure reaction rates under CO rich conditions, in our current experimental setup. The primary error which could arise in our normalizing technique is assuming that all Pt sites on the particle exhibit the same activity. One way to observe how this may affect the site estimation technique is to place an upper bound

on the active site estimates; this can be accomplished by assuming that only terrace sites are contributing the observed reaction rate. Note that this is clearly an extreme case as (1) step sites will exhibit some CO_2 production activity and (2) it is likely that, under reaction condtions, CO diffusion between step and terrace sites is rapid. Using our estimates of terrace sites from TPD data, we can estimate the total number of active sites assuming reactivity from terrace sites alone; this is shown in the data of **Figure 31**. As this upper bound limit estimates, the primary trends still hold true; site estimates begin to approach the TPD site estimates assuming all sites are active, however the error in these measurements exhibit overlap (we will examine TPD and reactivity measurements further in our discussion of **Figure 31**). Clearly, this upper bound limit does not stray far from the initial estimates. Thus to summarize, in the experiments of the present study we remain focused on reaction conditions which generate CO-rich conditions (in Figure 27 O_2/CO = 0.5, moderate temperatures) on Pt particles with average diameters of d_p > 2.6nm. Based on our measurements and previous observations of other studies, we conclude CO oxidation kinetics on our samples are essentially structure insensitive (independent of particle size) and can provide a reasonable method to estimate total active sites present on the Pt/SiO_2 model catalyst surface during elevated pressure reaction conditions.

Due to the well-studied nature of the CO oxidation reaction, the availability of technical catalyst data in the literature (under similar O_2/CO ratio conditions and pressure regimes) allows and opportunity for comparison to the reactivity data obtained in the current study. While technical catalyst studies are generally conducted under flow

conditions (as opposed to the batch reactor conditions employed in this study), it is nonetheless useful to compare such model studies to technical catalyst studies under similar O_2/CO conditions. Such comparisons have proven insightful in comparing single crystal data to technical catalyst reactivity data.[66-68,169] Chemisorption measurements (e.g. CO or H_2) are commonly utilized to assess the total number of active sites on a technical catalyst sample. This estimate is then used to convert absolute reaction rates into turnover frequencies. The model catalyst data collected in this study offer an opportunity to conduct an analogous calculation to compare to the technical catalyst data; CO TPD site estimates can be used to convert absolute CO oxidation reactivity measurements into turnover frequencies. Shown in **Figure 32** are CO_2 oxidation reactivity measurements for Pt/SiO_2 data (1-10 ML Pt; 1/2 O_2/CO) obtained in the current study (solid squares, ■), normalized by active site estimates obtained by CO TPD measurements. Also shown are reactivity data obtained in previous technical catalyst studies of Cant et. al.[70] (heavy dash line) under the same O_2/CO ratio = 0.5 conditions. Additionally, single crystal reactivity data (Pt(100)) of Berlowitz et. al.[169] (open circles ○), also taken under the same O_2/CO conditions, is also shown for comparison. As the data illustrates, excellent agreement is achieved between the model Pt/SiO_2 data of the present study and previous single crystal (Pt(100))[169] data. Pt/SiO_2 model catalyst data also lines up well with an extrapolated trend of the higher temperature (T > 450 K) region of CO oxidation kinetics on Pt/SiO_2 technical catalyst surfaces[70], and exhibits no substantial particle size effect over the particle sizes and reaction conditions studied.

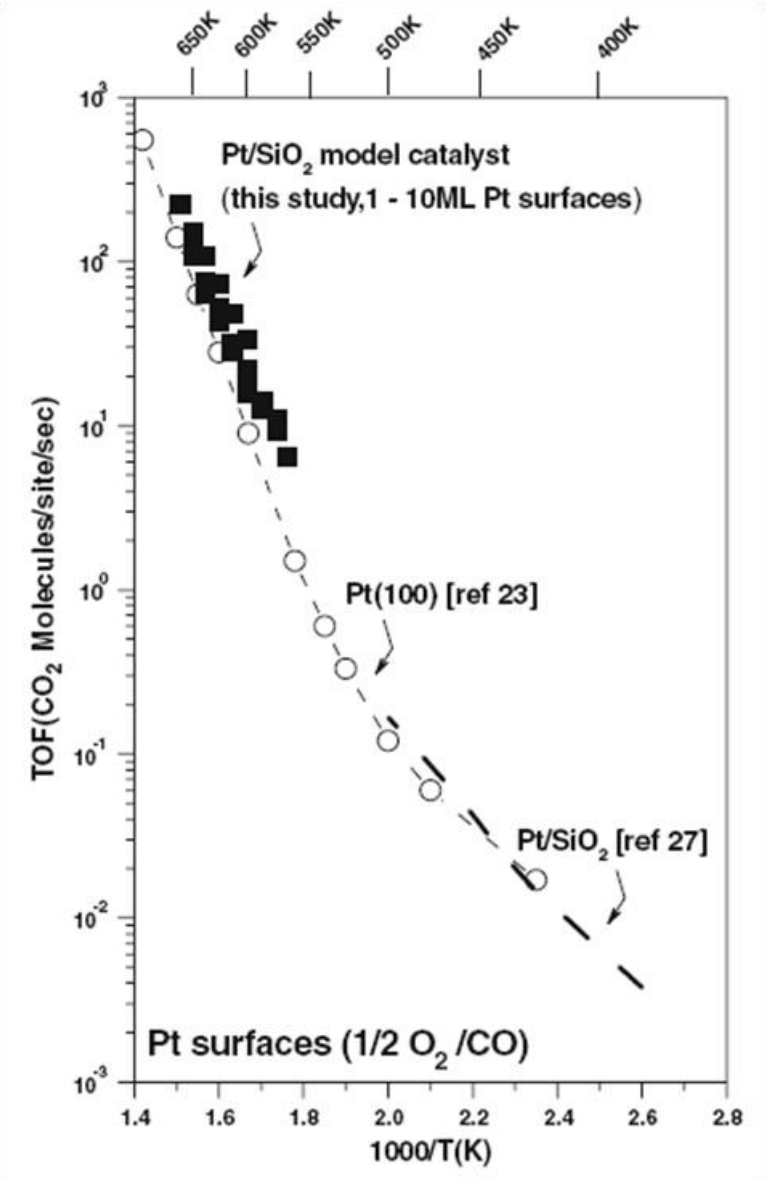

Figure 32. Comparison of Pt/SiO_2 model catalyst data to literature single crystal and technical catalyst data. Pt/SiO_2 model catalyst data (of Figure 1(a)) normalized by CO TPD site estimates of Figure 27. Open squares (□): Pt/SiO_2 model catalyst data (1-10 ML Pt; Pt particle diameter range d_p = 2.6 - 4.2 nm) from present study (1/2 O_2/CO, P_{total}=8 Torr). Heavy dashed line: Pt/SiO_2 technical catalyst data from Cant. et. al.[70] (1/2 O_2/CO, P_{total}=14.6 Torr). Open circles (-○-): Pt(100) single crystal data from Berlowitz et. al. [169] (1/2 O_2/CO, P_{total}=24 Torr).[11]

This data highlights the good agreement achieved between low pressure (CO TPD) and elevated pressure (reactivity) characterization site estimations on model Pt/SiO_2 systems.

Taken together, the data presented illustrate the utility and insight which can be gained into high pressure reactivity measurements with well-characterized model catalyst surfaces prepared by vapor deposition techniques. These characterization studies will serve as a useful benchmark for investigating structure sensitive reactions and samples/reaction systems with increased complexity on such UHV prepared films.

In summary, Pt/SiO_2 model catalyst surfaces were prepared and studied entirely in situ, under relevant temperature and elevated pressure conditions (approaching 1 atm). CO oxidation reactions were run under elevated pressure conditions to assess reactivity and characterize the number of active Pt surface sites as a function of Θ_{Pt}. CO TPD and STM measurements were also conducted to provide additional measure of active Pt sites and assess Pt particle sizes as a function of Θ_{Pt}. Results demonstrate that CO oxidation reaction on Pt/SiO_2 model catalyst samples exhibit similar O_2/CO dependencies (negative in CO, positive in O_2), activation energies, and structure insensitivity as observed on Pt single crystal and technical catalyst samples, under CO-dominant reaction conditions investigated (average Pt diameters: $d_p > 2.6$nm). Estimates of Pt active sites based on CO oxidation kinetics (under CO dominant conditions (1/2) O_2/CO) are in good agreement with estimates obtained from TPD measurements. STM images obtained for Pt particles deposited on ultra thin SiO_2 film at T = 300 K also provide an additional estimate of active sites in general agreement with reactivity measurements. In

this sense, we have demonstrated that both low pressure and high pressure characterization methods provide consistent and good estimations of total Pt active sites. Good agreement is achieved between reactivity measurements obtained on Pt model catalyst and previous single crystal studies, and correlates well with technical catalyst studies (T > 450 K), for measurements conducted under similar CO-dominant O_2/CO ratios. This demonstrates the correlation between kinetic results obtained on single crystal, model catalyst, and technical catalyst surfaces.

n-Heptane Dehydrocyclization

In the previous sections the percentage of various adsorption sites on model catalysts surfaces of Pt nanoparticles grown on silica in an ultra high vacuum was determined. These particles have been discussed in terms of their similarities to high index single crystals. Adsorption sites on Pt particles are shown to differ substantially as the size is dropped below 4nm consistent with hard sphere models. Quantitative measurements of this type have not been conducted on oxide-supported high surface area technical Pt catalysts. Accurate relationships between single crystals and high surface area catalysts have therefore not been met as a result of the material gap which exists between these two systems. Here, we assess dehydrocylization reaction on Pt nanoparticles under high pressure conditions and relate the reaction rate to the concentration of terrace and step sites on these surfaces as a function of particle size. We employ similar reaction conditions as were conducted on the high-index crystals so direct comparison can be made. The findings allow relationships to single crystal and oxide supported high surface area catalysts.

Particle Size

Images from TEM experiments are shown in **Figure 33**. Each Pt/SiO_2 sample was prepared on a carbon coated molybdenum grid. The silica films are estimated to be 1.5nm thick as determined from the calibration of silica deposition rate on the tantalum mounting plate used as the sample holder. It can be seen that the particles are relatively mono-dispersed for low Pt coverage's and this characteristic is lost as the coverage increases. It is also observed particle diameter become smaller as the monolayer equivalent coverage is decreased. Particles are circular in shape and indicate the spherical nature of particles grown through vapor deposition techniques. This spherical character is similar to Pt nanoparticles grown on high surface area SiO_2 substrates.

Shown in **Figure 34** are two examples of Pt nanoparticles after being subjected to 15torr n-heptane /480torr H_2 at 575K for 1hour; the reaction conditions discussed below. As can be seen in **Figure 34**, both the size and nanoparticle density are relatively unchanged over the course of the reaction. This indicates that changes in the reaction rate can be described without concern of particle sintering. This type of behavior has been seen by others in the literature.[54] It should be noted, nanoparticle diameters before and after reaction conditions are similar to size estimates obtained from STM measurements of Pt nanoparticle grown on silica thin films (0.3nm).

Concentration of Step Sites

CO thermal desorption spectroscopy (TDS) measurements on Pt nanoparticles have been discussed in the previous section. The results allow a quantitative assessment of the site-concentration on the surface of the Pt nanoparticles. Briefly, the desorption

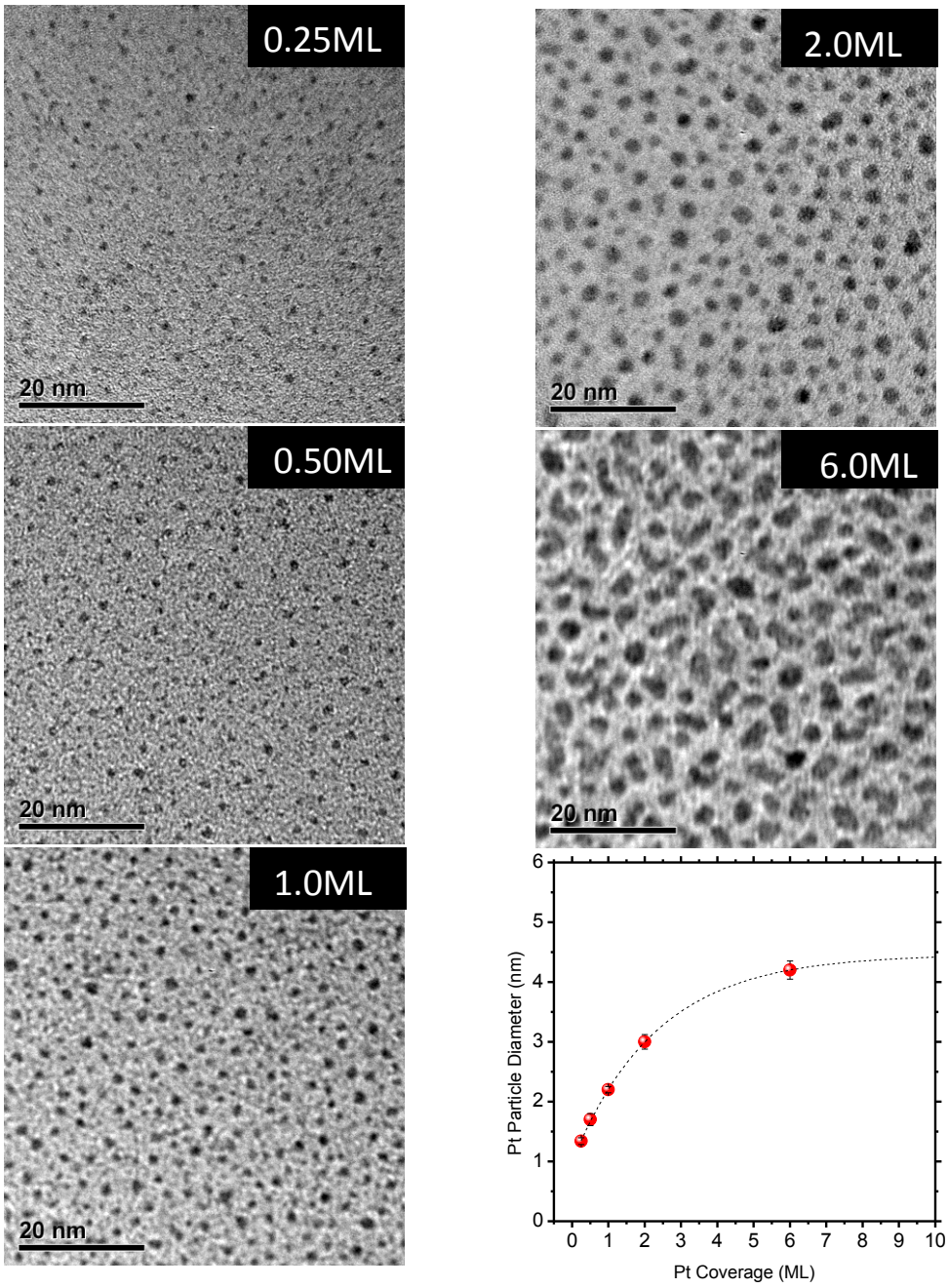

Figure 33. TEM images of Pt nanoparticles deposited on SiO_2. Images taken using a Jeol 2010 at 200 keV. The SiO_2 film was grown on a carbon coated molybdenum grid in ultra-high vacuum (UHV). SiO_2 film thickness is estimated to be 1.5nm thick. Pt was also deposited in UHV and total deposited atoms listed in monolayers ($1x10^{15}$ atoms/cm^2) as indicated.[174]

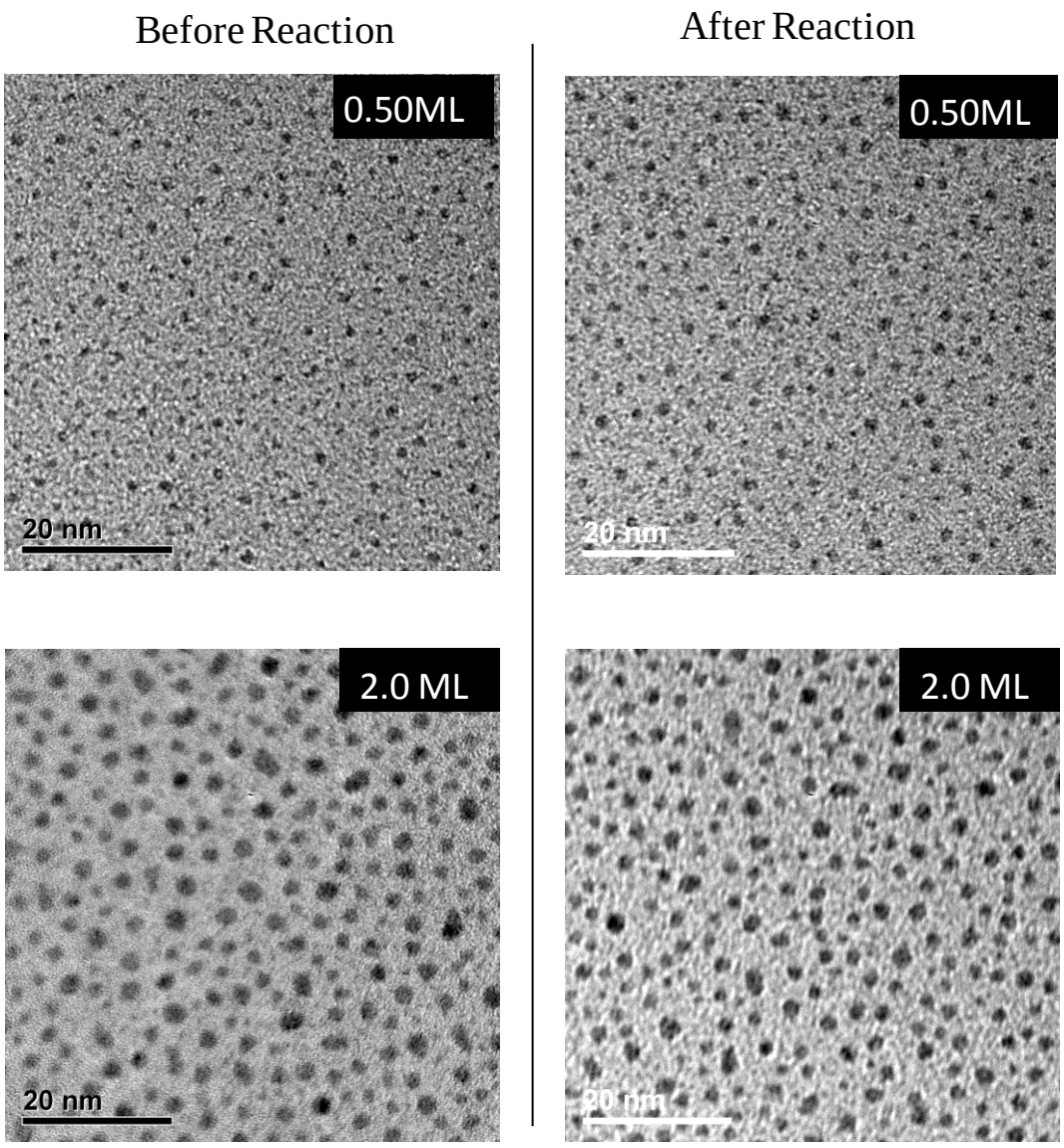

Figure 34. TEM images of Pt/SiO_2 before and after dehydrocyclization reaction. Images taken using a JEOL 2010 at 200 keV.[174]

spectrum of CO from various Pt nanoparticle sizes gives rise to two features which can be assigned to terrace and step desorption sites. The integrated area of each feature can be related to the concentration of these sites on the surface (see **Figure 35**). The analysis can be further corroborated using CO infrared reflection absorption spectroscopy (IRAS). The available surface sites on the nanoparticle can be defined as either ≥ 8fold coordination (e.g. C_9, C_8) or ≤7 fold coordination n (e.g. C_7, C_6, C_5). **Figure 35** demonstrates the concentration of under-coordinated atoms on the surface of Pt nanoparticles from CO TDS measurements. Also presented in **Figure 35** are hard sphere model calculations assuming nanoparticles grow in various geometric orientations: octahedrons, cubo-octahedrons, rhombic dodecahedrons, and truncated cubo-octahedron cap. It is clearly demonstrated the site estimates from the CO TDS (under vacuum conditions) correlate well with the model which describes nanoparticles as a cubo-octahedron cap. These results correlate well with microscopy measurements conducted on bulk catalyst samples which demonstrate Pt nanoparticles grow spherical on silica and exhibit (100) and (111) facets.[49,147-150]

Dehydrocyclization Rate & Selectivity

Two reactions on single crystals in the literature which can be used for evaluating n-heptane reactions on Pt nanoparticles are n-hexane[57] and n-heptane dehydrocyclization[59]. Both n-heptane and n-hexane are believed to cyclize (i.e. to toluene and methylcyclopentane respectively) favorably on similar under-coordinated reaction sites, although, both products can also be formed are highly coordinated terrace sites ≥C_8. Dehydrocyclization is believed to first proceed through cyclization followed

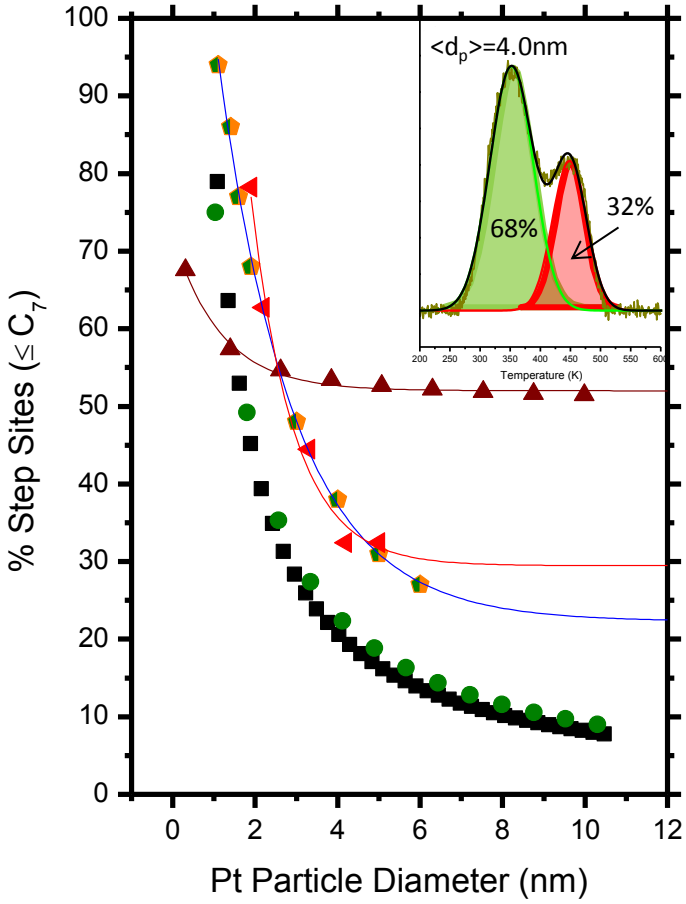

Figure 35. Concentration of step sites with coordination $\leq C_7$ as a function of particle size assuming various nanoparticle geometries.[51] (Square) octahedral, (circle) cubo-octahedron, (triangle) rhombic dodecahedron, (hexagon) truncated cubooctrahdron cap. Also plotted is the concentration of step sites obtained from thermal desorption spectroscopy of CO on Pt nanoparticles. Inset is a representative example of the deconvoluted TDS spectrum.[174]

by dehydrogenation of the reaction intermediate.[185-198] This mechanism can be inferred from cyclohexene dehydrogenation reactions known to form a 1,3-cyclohexatriene (CHT) intermediate on Pt(100) and both a 1,2 and 1,4 MCT on Pt(111).[64,65] Pt(111) is shown to be less active on account of the 1,4 CHT which is believed to block sites for the 1,3 CHT pathway. An intermediate for dehydrocyclization of n-heptane has not yet been observed. For dehydrocylization of n-heptane, the concentration of under-coordinated atoms at the surface of the single crystal is shown to increase the rate of toluene formation.[59] High index surfaces such as Pt(557) which has 7 atom wide (111) terraces and one atom high step sites of C_7 have a higher activity by a factor of 2 than a Pt(111). Terrace width is also shown to be an important factor in the reactivity of the surface. Nanoparticles also exhibit similar catalytic behavior to single crystals. Rioux have demonstrated dehydrogenation of cyclohexene in the presence of hydrogen as a function of Pt particle size.[54] The reaction rate has been shown to increase as particle size is decreased.

For our apparatus, which has the unique perspective of direct comparison between supported and unsupported Pt. **Figure 36** demonstrates the dehydrocyclization of n-heptane to toluene reaction on both Pt single crystals and silica supported Pt nanoparticles. The data are the initial rates of toluene formation at <0.01% conversion. The reactivity data expressed in molecules per site per second (TOF) of toluene formation. Error bars represent the standard deviation of repeated measurements on freshly prepared surfaces. As Pt(100) flat surface and Pt(110) stepped surfaces also do not show reactivity higher than the largest nanoparticles. The Pt crystals display the

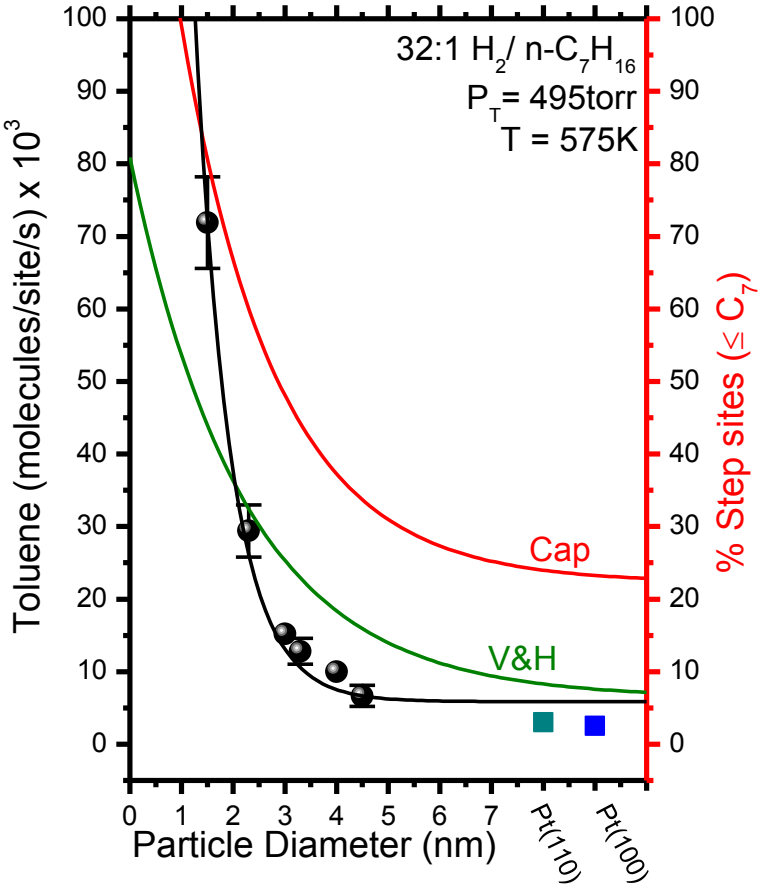

Figure 36. Formation rate of toluene from dehydrocyclization of n-heptane expressed in molecules/site/s as a function of Pt particle size.[174] Error bars represent standard deviation of repeated measurements on freshly prepared surfaces. Rate measurements on Pt(110) and Pt(100) obtained in the same apparatus are indicated. Also plotted are the concentration of step sites with coordination $\leq C_7$ on the surface of both cubo-octahedron[51] and a truncated cubo-octrahedron cap model.

reactivity in absence of any oxide-support effects in the reaction rate. This participation cannot be ignored in the reaction on supported nanoparticles (discussed below).

The rate of toluene formation on Pt nanoparticles (**Figure 36**) as the average nanoparticle size is reduced from 4nm to 1.3nm demonstrates an order magnitude increase in toluene formation rate with an exponential decrease in rate as the particles size is increased. This decay mimics the trend in the concentration of step sites calculated from TDS measurements. To further explore the quantitative comparison between the change in reaction rate and in under-coordinated atoms as the concentration of step sites in a cubo-octahedron is also plotted in **Figure 36**. It appears from this data the order of magnitude change in rate is larger than one would expect based on the concentration of step sites on this surface. This can be rationalized in the support effect increasingly plays a role as the particle size is reduced. From this comparison, larger Pt nanoparticles behave similiarly to single crystals and most likely exhibit a high concentration of terrace sites under reaction conditions. As the particle size is reduced the reactivity is more in line with the truncated cubo-octrahedron cap and particles exhibit surface with a high concentration of step sites per surface area per particle. It has been observed by our group that Pt particles in the size range have a majority (80%) of their sites being under-coordinated sites. This data demonstrate the deviation of single crystal from particles under reaction conditions and the differences in site estimates between high pressure and low pressure characterization techniques.

Time dependent n-heptane dehydrocyclization reactions were conducted on Pt(110) and 6nm Pt/SiO_2 at 575K (see **Figure 37**). Both surfaces were run for a total of

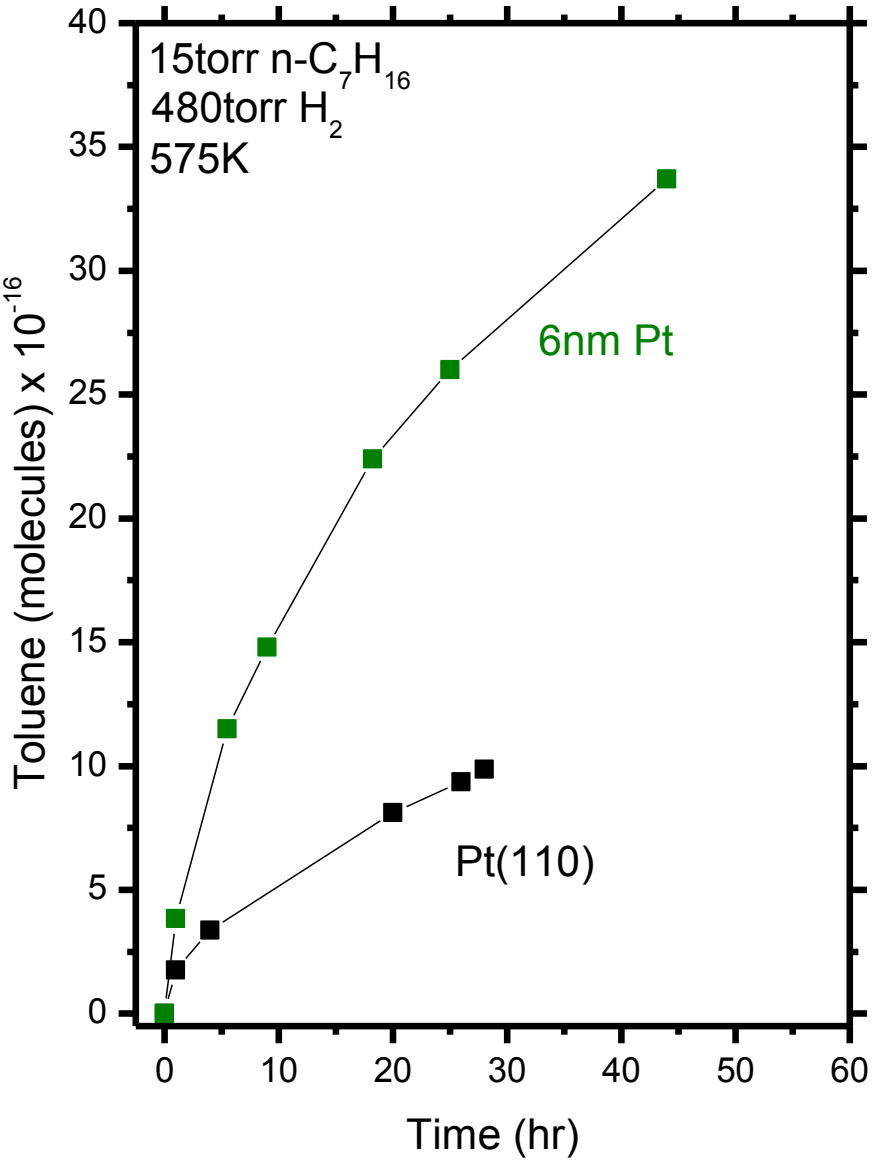

Figure 37. Time dependent n-heptane dehydrocyclization on Pt/SiO_2 and Pt(110).[174]

30hrs. Both surfaces showed progressively slower rates after 1 hour of reaction time. Post reaction AES on both surfaces showed a strong carbon feature on both samples. Reacting with H_2 at 575K post reaction had virtually no effect on the carbon concentration. The carbon could only be removed by cleaning in oxygen. This result is consistent with what has been observed in the literature on Pt single crystals. The data demonstrates Pt/SiO_2 to be more reactive throughout the duration of the experiment than Pt(110) and also to deactivate at a slower rate. Since Pt nanoparticles in the range of 6nm contain only a small percentage of step sites, the higher reaction rate could be attributed to a combination of several factors (i) the facets on the surface of nanoparticles are more reactive than a (110) on Pt(110) (ii) the silica substrate participates favorably in the reaction mechanism (iii) carbon spill-over from the particle to the support. From the rate measurements in **Figure 36** our Pt(110) demonstrated a similar rate as our Pt(100) which indicates pure Pt to be less reactive overall. Moreover, work by Somorjai et. al. demonstrates the rate on Pt(111) to be similar to highly stepped Pt(25,10,7) and the rate for Pt(557), which demonstrates a rate maximum, to be higher by a factor of 2 than Pt(111).[59] Overall, work on single crystals would indicate nanoparticle structure (dynamic or not) in this size regime cannot alone account for the difference in the time dependent data. Substrate participation through spill-over and/or hydrogen transfer is most likely the key factor.

The selectivity for toluene is shown in **Figure 38**. The data indicates as the nanoparticle size is decreased the selectivity for toluene is also decreased. This result is similar to high index single crystal studies where the selectivity decreases with

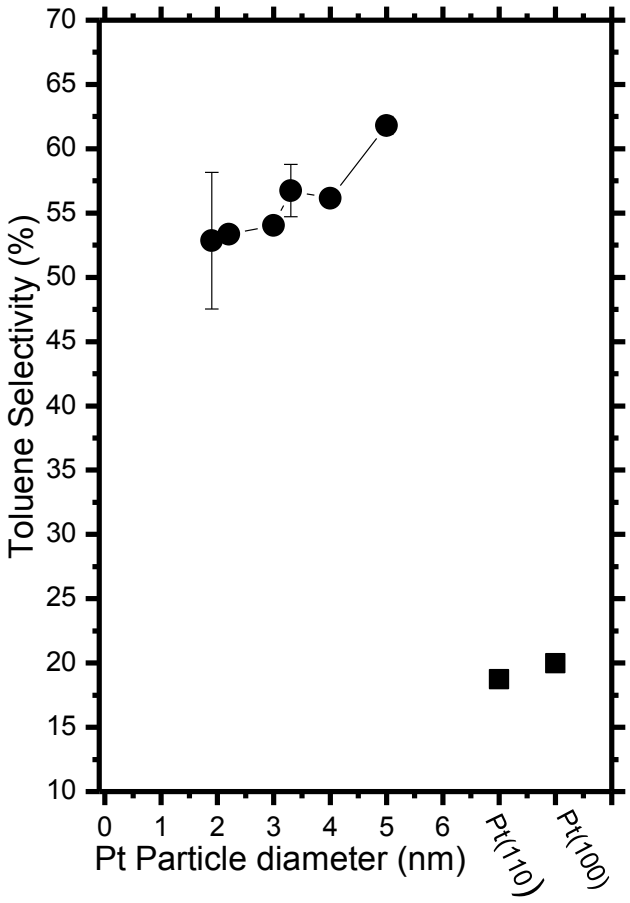

Figure 38. Selectivity of toluene during n-heptane dehydrocylization on Pt/SiO_2, Pt(110) and Pt(100). Selectivity for toluene is determined with reference to hydrogenolysis products and indicated as a percent of total products produced.[174]

increasing kink concentration. Kink site ($\leq C_6$) concentration increases as the nanoparticle size is decreased. For the n-heptane dehydrocyclization reaction high index single crystals have shown an increase in kink site concentration is also shown to decrease the selectivity towards toluene.[59] Terrace width is also an important factor in the selectivity of this reaction. Surface sites which participate in hydrogenolysis, dehydrocyclization, cylization, and isomerization are believed to occur on a similar set of reaction sites with a main component being C_7 undercoordinated atoms. As particle size goes decreases the concentration of kink sites goes up followed by a decrease in selectivity to toluene. This effect occurs along with an increase in step site concentration.

The results presented here are a first attempt to relate the concentration of step sites as the particle size is varied to the change in reaction rate over such particles. The results demonstrate that the trend in undercoordinated atoms closely relates to trend in reaction rate as the particle size is decreased. The results presented here demonstrate the change in undercoordinated atoms cannot alone account for the change in reaction rate. The results must also be related to the contribution of the support and reaction mechanism as the particle size is varied.

CHAPTER IV

CHARACTERIZATION AND REACTION STUDIES OF SILICA SUPPORTED RHODIUM MODEL CATALYSTS

CO Oxidation

Due to its fundamental and practical importance, metal oxide supported Rh model catalyst samples have been prepared and characterized by a number of groups using a variety of synthetic techniques. Insights into particle morphology, particle sintering, interaction with CO and O_2 ambients, and low pressure CO oxidation kinetics have been acquired for a variety of oxide supported Rh systems (alumina[179,199-204], silica[175,205,206], titania[33,207-209], and magnesium oxide[201,204,210] single crystal and thin film substrates). Additionally, recent solution-based methods for generating mono-dispersed Rh nanocubes supported on Si have allowed for ex-situ CO oxidation kinetic measurements on well-defined Rh particles.[211]

With regards to CO oxidation reaction kinetics, much work still remains to fully investigate the behavior of this fundamental reaction on Rh model catalyst systems. While reactivity on Rh surfaces at elevated pressures under high O_2/CO conditions remains a currently debated topic[72,181,183], CO oxidation under CO-rich conditions (low O_2/CO ratios) exhibits structure insensitive reaction kinetics.[66,67,69,70,71,182] As such, CO oxidation kinetic measurements under these conditions could potentially be employed as a probe reaction to directly compare model catalyst and single crystal samples under identical reaction conditions and experimental setup, and thus to investigate the

qualitative and quantitative agreement regarding reaction rates, activation energies, and number of active Rh sites. When oxygen begins to become a dominant surface species on the Rh, Pd surfaces (under sufficiently high temperatures and/or high oxygen partial pressures), kinetic behavior begins to deviate from this CO dominant regime, as oxygen inhibition begins to decrease the observed CO_2 formation rate.[66,67,169] Likewise, reaction measurements obtained under ultrahigh vacuum conditions (via molecular beam techniques) have shown that Rh single crystal[178,212] and Rh/Al_2O_3 surfaces[179], can exhibit structure sensitive reaction behavior outside of the CO inhibited regime (i.e. surfaces containing low CO coverages).[178,179,212] Under oxygen rich (high O_2/CO ratio) reaction conditions at elevated pressures, oxygen surface phases (such as surface or bulk oxide phases) can exist and can provide a source of surface oxygen for reaction with CO[213], however recent studies regarding the exact nature of the reactivity of Pt-group oxide phases have been the subject of much debate.[60,62,72,181,182] While low pressure studies[177,214-217] and recent high pressure studies[60,62,113,182] of CO oxidation on Pt-group single crystals (Pt, Rh, Pd) have suggested that the most active phase for CO oxidation at low and high pressures is a CO uninhibited metal surface, alternative proposals have suggested that surface oxide phases may play the key role in high reactivity on Pt-group metals under oxygen rich conditions.[72,181,183,184] Therefore, the work here is focused on the CO-rich regime (low O_2/CO ratios), in which elevated pressure reactivity behavior is known to behave as a structure insensitive reaction, limited by the CO desorption rate, with reaction kinetics reflecting traditional Langmuir-Hinshelwood behavior.[60,62,66,67,70,182] Under such conditions, CO oxidation reaction can be employed

as a characterization tool to estimate the number of active Rh sites as a function of metal coverage.

In this section, CO oxidation is employed as a probe reaction to characterize $Rh/SiO_2/Mo(112)$ model catalyst samples and their relation to single crystal surfaces. The primary aim in this study is to develop an understanding of the extent of qualitative and quantitative agreement between CO oxidation kinetic data obtained on Rh/SiO_2 model catalyst samples and Rh single crystal samples under elevated pressure conditions (P = 8.0 Torr). Model catalyst results are compared with data collected on a Rh(111) single crystal sample to assess kinetic behavior and (O_2/CO) dependence of the CO oxidation reaction on the model catalyst surfaces. This is the first attempt to directly compare elevated pressure CO oxidation reaction kinetics on Rh model catalyst surfaces to Rh single crystal surfaces (prepared entirely in situ in UHV) under identical reaction and reactor conditions. For additional characterization, CO desorption measurements on Rh/SiO_2 samples have been obtained, and STM data (in a separate STM system) has been collected for Rh deposited on ultra thin SiO_2 films (1 ML, 3 Å) to provide estimates of particle size and number of active Rh sites as a function of Rh coverage.

CO TPD From $Rh/SiO_2/Mo(112)$

Displayed in **Figure 39** are results from CO TDS measurements from the $Rh/SiO_2/Mo(112)$ samples and a Rh(111) single crystal. As discussed in the experimental section, Rh/SiO_2 samples of a variety of coverages (θ_{Rh} = 1 ML through 10 ML) were prepared in the UHV chamber, and 4 L CO ($P_{CO} \sim 5 \times 10^{-7}$ Torr) is dosed at T_{ads} = 175 K, followed by heating to T = 700 K at ~ 5 K/s. TDS spectra of coverages

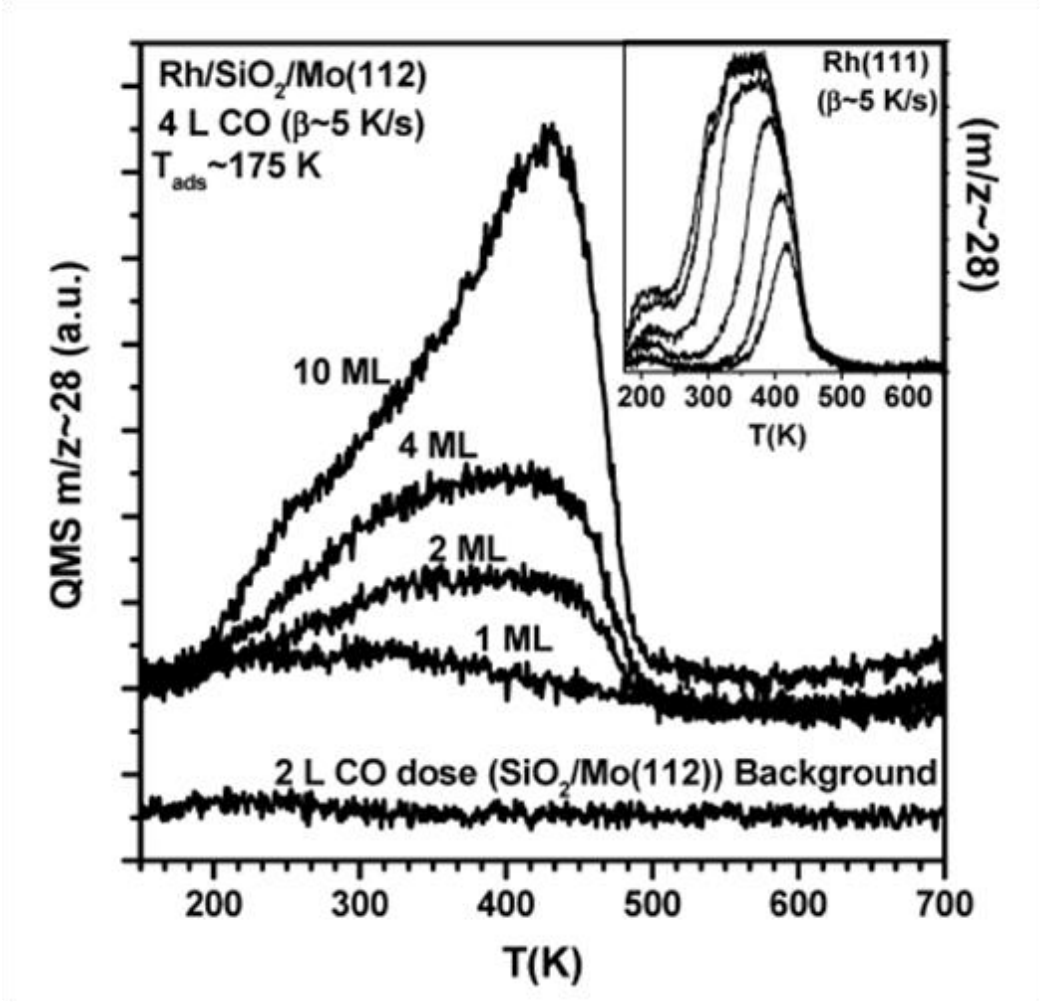

Figure 39. CO-TDS from Rh nanoparticles on SiO_2. Inset: Coverage dependent (0.25 L, 0.5 L, 1 L, 2 L, 4 L and 6 L CO doses) CO TPD from Rh(111).[12]

below < 0.5 ML produced TDS spectra with low QMS signals obscured by background. Also shown in the inset of **Figure 39** are the TDS spectra obtained from the Rh(111) single crystal for various CO doses (0.25 - 6 L CO). A saturation dose is apparent between 2 - 4 L CO. CO TDS from the Rh/SiO_2 and Rh(111) sample exhibited desorption characteristics generally similar to those observed in previous studies on Rh(111) and Rh particle studies.[200,214,218] A small feature on the Rh(111) sample (T ~ 150 - 200 K) for large CO doses is believed to be due to contributions from the sample leads. We conservatively estimate that this contributes to a ± 20% error in the integrated area estimates for the Rh(111) integrated area for 4 L CO dose. As will be discussed below, the CO was observed to adsorb and desorb molecularly, with no indication of substantial CO dissociation. The CO TDS spectra obtained from the particles were then used to estimate the number of Rh sites on the Rh/SiO_2 samples as a function of Rh coverage, as described in the Experimental section. Shown in **Figure 40** are the values obtained from this exercise, in terms of Rh sites/cm^2, as a function of Rh coverage. As the data demonstrates, estimates of Rh sites from the TDS data increases with increasing Rh coverage, approaching the Rh site coverage for the Rh(111) single crystal sample (1.6×10^{15} sites/cm^2). Error bars represent the estimated error (± 20 %) from Rh(111) TDS integration discussed above.

As stated above, CO adsorption and desorption was observed to be molecular in nature from the Rh/SiO_2 surfaces, with no evidence for substantial CO dissociation. While CO dissociation is not believed to occur appreciably on low index Rh single crystal surfaces, it has been shown that high index Rh single crystals (e.g. Rh(210))[219]

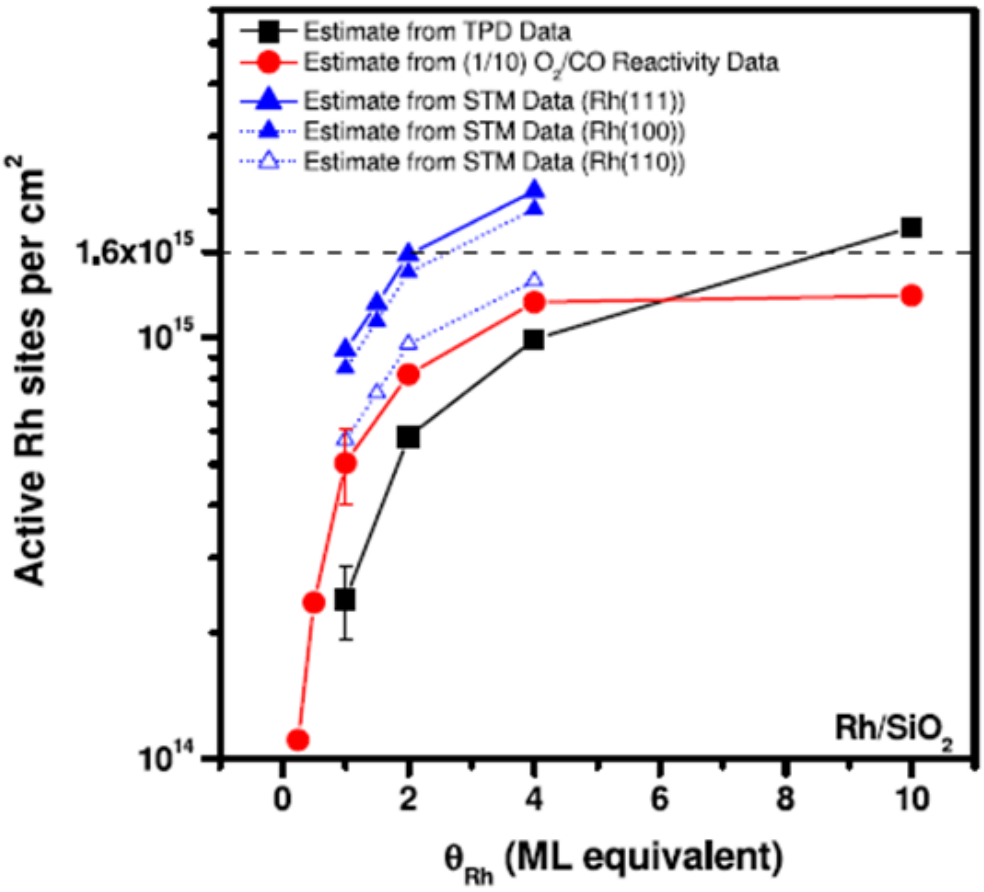

Figure 40. Number of active Rh sites per cm^2 vs. Rh coverage as estimated from TDS, (1/10) O_2/CO reactivity data, and STM data.[12] Characteristic error bars for the data sets, shown for reference, are discussed in text. Estimates of error in θ_{Rh} from stated coverage are ±15%, as discussed in the text. Average particle diameter (in Angstroms, Å) (■) and standard deviation (error bars; ±σ), as determined from histogram data obtained from STM images. Shown by dotted lines (-----) are the minimum and maximum Rh particle diameter observed for a given Rh coverage.

and certain oxide[201-204,220] supported Rh particles can induce dissociation of CO on the Rh surface. Freund and co-workers have demonstrated that on ultra thin alumina substrates, Rh particles can dissociate adsorbed CO upon heating, with an activity for CO dissociation exhibiting a particle size dependence (maximum CO dissociation for particles ~103 atoms).[202,203] Matolin[201,204] has also demonstrated via TPD/SIMS experiments that CO can dissociate on MgO and alumina supported Rh particles during exposure to CO and during CO/O_2 reaction under low pressure conditions (~10^{-6} Pa). Work on technical catalyst surfaces[220] under reaction conditions has shown evidence (via IR spectroscopy) for CO dissociation on alumina and titania supported Rh, but no evidence for appreciable CO dissociation on silica supported Rh, indicating possible effects from support and/or particle size distribution on the different oxides. CO TDS spectra in our studies did not exhibit the high temperature (T ~ 520 K) C + O recombinative desorption feature, which has been observed from TPD studies on Rh/Al_2O_3 films[201] Likewise, CO TDS experiments could be run sequentially (without sample O_2 cleaning), without a significant decrease in CO uptake which would be expected for substantial CO dissociation. Observations during reactivity measurements also did not indicate substantial CO dissociation, with respect to kinetic measurements. Indeed, during our study we have generated Rh/SiO_2 samples and run them through long sequential series of reaction experiments in O_2/CO reaction mixtures (e.g.; 10+ reactions), without cleaning of the Rh/SiO_2 samples. No substantial decrease in activity is observed (within measurement error), which would be expected with substantial C buildup from CO dissociation. However, it should be mentioned that reactivity

measurements will likely be a rather insensitive technique to investigate CO dissociation on small Rh particles under reaction conditions, as it has been previously shown[201,204] that adsorbed C will be reacted away readily by oxygen even under low pressure reaction conditions. Thus, if any CO dissociation is occurring on our Rh/SiO_2 particles, it appears that it is a small amount that does not affect the CO uptake TDS spectra or reaction kinetics (due to rapid reaction of C under reaction conditions), to an extent we can measure under our experimental conditions and measurements sensitivities. Thus, CO uptake measurements are a reasonable technique to quantify the number of Rh active sites on Rh/SiO_2 samples.

CO-IRAS of Rh/SiO_2 and Rh(111) Surfaces

Infrared spectra of CO adsorption on Pt-group metals can offer insights into the nature of particle morphology and available CO binding sites on the Rh/SiO_2 surfaces. CO stretching frequencies (vCO(cm^{-1})) exhibit shifts based on CO binding environment (e.g. atop, bridging, three fold hollow).[106] Shown in **Figure 41** Inset is a CO-IRAS spectra obtained from a CO saturated Rh(111) surface at T = 300 K, for reference comparison to the Rh/SiO_2 samples. In accord with previous detailed IRAS and HREELS studies of the CO/Rh(111) system, CO adsorbs in atop positions (feature at vCO = 2064 cm^{-1}) and three fold hollow positions (feature at vCO = 1865 cm^{-1}) at saturation coverages.[182,218,221,222] As temperature is increased (data not shown for Rh(111)), the CO coverage is decreased, resulting in the disappearance of the three fold hollow feature followed by dipole induced peak shifts to lower wavenumbers of the atop CO feature. Shown in **Figure 41 and 42** are representative temperature dependent CO-

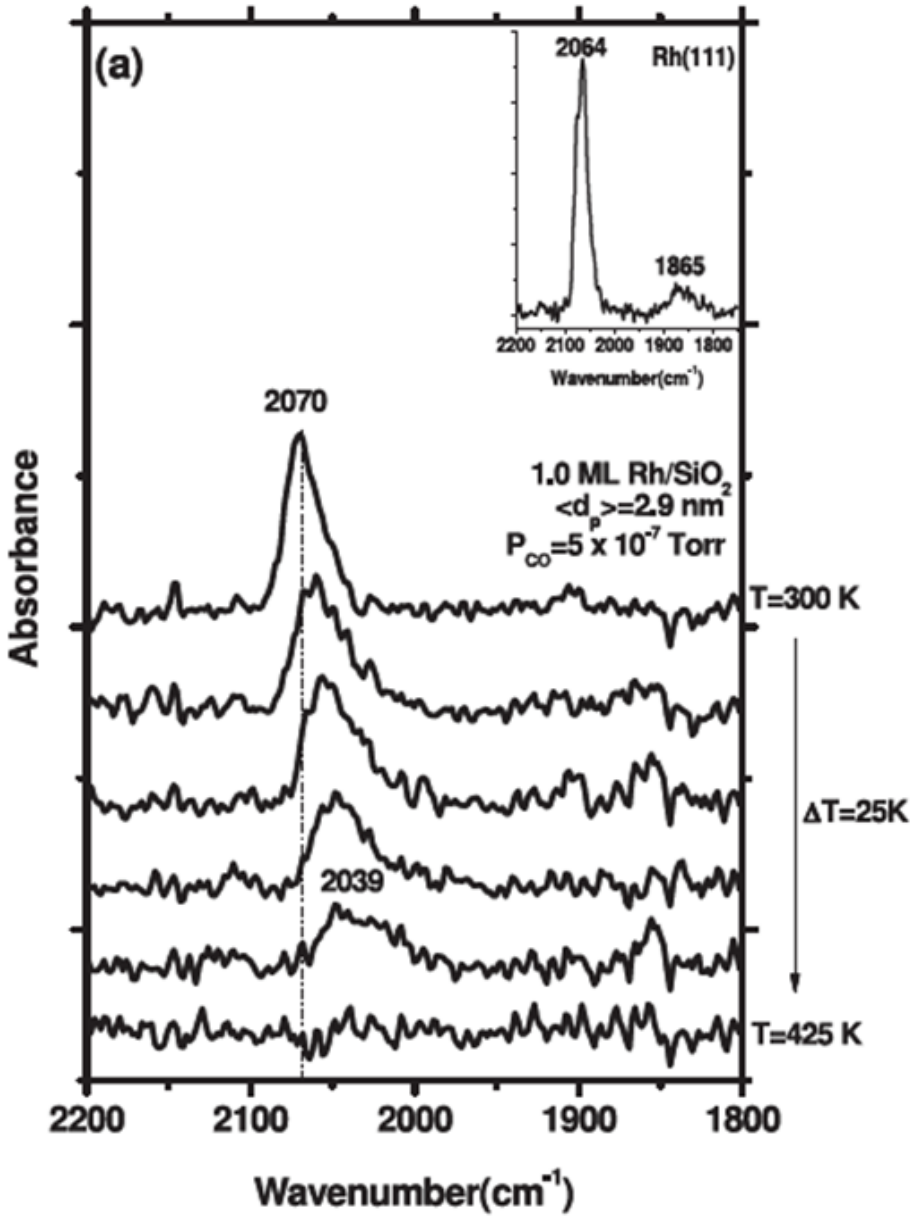

Figure 41. Temperature dependent CO-IRAS spectra on 2.9nm Rh particles. Initial temperature T=300 K, T is increased in T=25 K increments for IR spectra collection. Inset: CO-IRAS spectra of saturation CO coverage on Rh(111) single crystal at T = 300 K.[10]

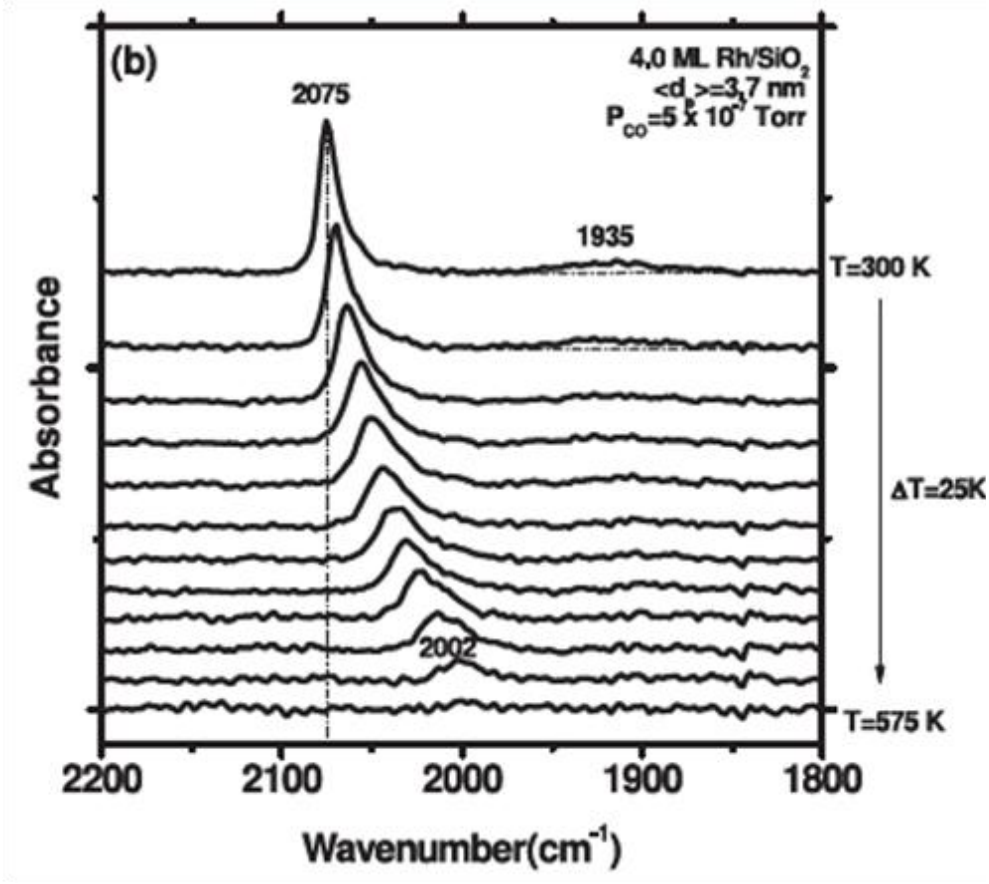

Figure 42. Temperature dependent CO-IRAS spectra on 3.7nm Rh particles. Initial temperature T=300 K, T is increased in T=25 K increments for IR spectra collection.[10]

IRAS spectra obtained from $<d_p>$ = 2.9 nm (Θ_{Rh} =1.0 ML) and $<d_p>$ = 3.7 nm (Θ_{Rh} =4.0 ML) Rh/SiO_2 surfaces. CO spectra are obtained at ΔT = 25 K increments in an environment of P = 5 x 10^{-7} Torr CO, starting from an initial temperature of T = 300 K. At saturation coverages, CO exhibits an atop adsorption feature at ν_{CO} = 2070-2075 cm^{-1} on both the 2.9 nm and 3.7 nm Rh/SiO_2 surfaces. A less intense, broad adsorption feature is observed between 1875-1975 cm-^{1} for the 3.7 nm (4.0 ML) surface at T= 300 K; as will be discussed shortly, this feature is similar to a bridging bound (2- or 3- fold coordinated) CO binding feature which has been observed on previous studies of Rh/Al_2O_3 [223,224] and Rh/TiO_2 model catalysts[225]. As the temperature is increased, CO IRAS spectra exhibit trends in agreement with previous observations of CO on Rh surfaces. With increasing T, the CO surface coverage is decreased due to an increase in the CO desorption rate, as evidenced by the concomitant *(1)* decrease in IRAS signal intensity and *(2)* peak shift to lower wavenumbers. This shift to lower wavenumbers is consistent with decreased dipole coupling of the CO molecules as CO coverage is decreased. Surface concentration of CO is below detection limit above temperatures of T = 550 K for all the surfaces studied. Similar temperature dependent CO-IRAS behavior was observed for all coverages studied (0.5 ML - 10 ML).

Figure 43 shows CO-IRAS spectra obtained in PCO = 5 x 10^{-7} at room temperature, T = 300 K, for various Θ_{Rh} coverages (0.5 ML - 10 ML). As one would expect, CO IRAS intensity increases as Rh coverage is increased. A slight shift (2070 cm^{-1} to 2075 cm^{-1}) in ν_{CO} to higher wavenumbers is observed as the coverage (and particle size) is increased. This slight shift could be due to increased dipole-dipole

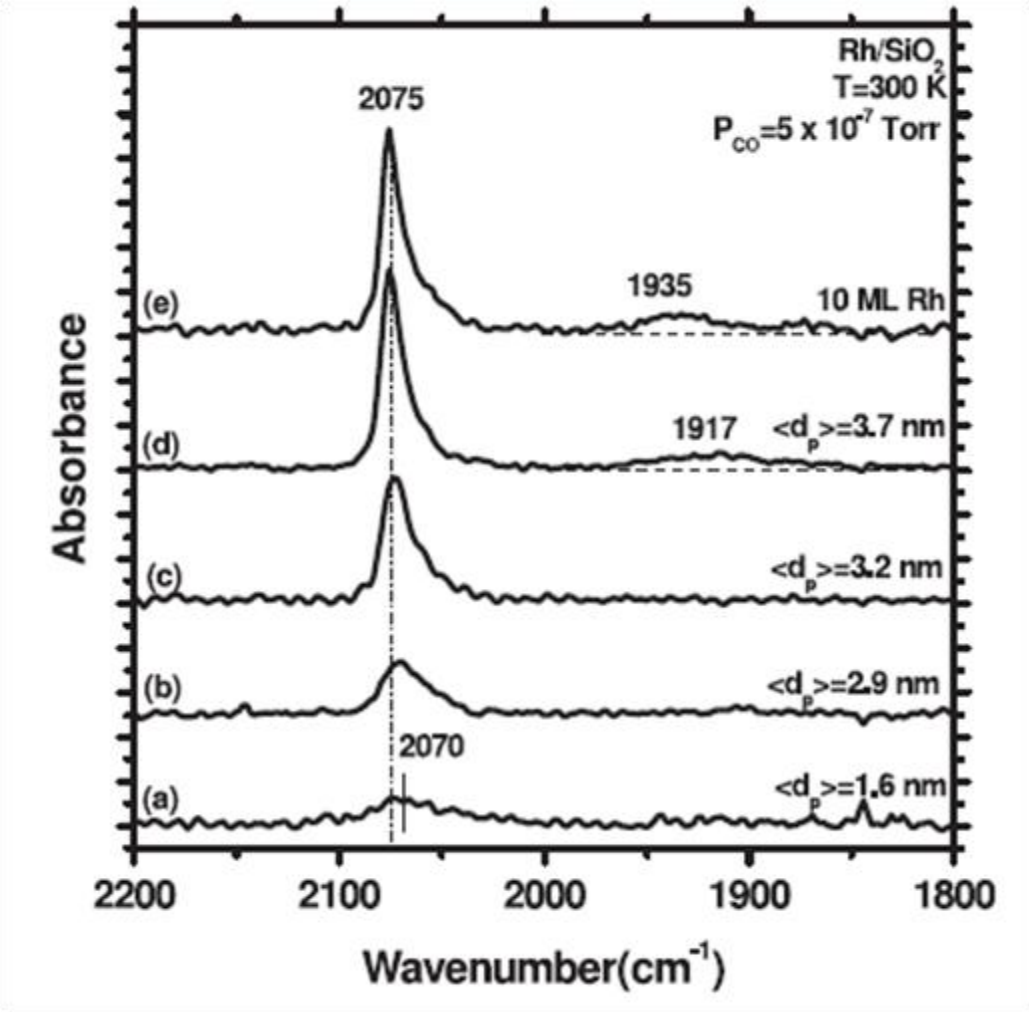

Figure 43. Rh coverage dependent CO-IRAS. (a)-(e).Θ_{Rh} dependent CO-IRAS spectra for coverages (a) 0.5 ML, (b) 1.0 ML, (c) 2.0 ML, (d) 4.0 ML, (e) 10 ML Rh. All spectra obtained in P_{CO} = 5 x 10^{-7} Torr, T=300 K. Average particle sizes for coverages $<d_p>$ denoted in spectra.[10]

coupling between surface bound CO molecules, which may be more pronounced on larger particles which could accommodate more CO (larger close packed (111), (100) facets). As the Rh particle size is increased (to 4.0 ML and above), the second, broad ν_{CO} feature observed at lower wavenumbers becomes visible in the CO-IRAS spectra; this ν_{CO} is consistent with a bridging bound CO surface species observed in previous CO-IRAS studies of Rh/Al_2O_3 surfaces.[223,224] This bridging type feature is less pronounced on the Rh/SiO_2 surface prepared with lower Rh coverages, presumably due to the lower amount of adsorbed CO present on the surface, which attenuates the intensity of the CO-IRAS features.

Detailed work by Freund and co-workers has examined CO adsorption employing CO-IRAS on Rh/Al_2O_3 model catalyst surfaces.[223,224] Infrared spectra obtained by these investigators on samples grown or annealed to T > 300 K, also show atop (2080 cm^{-1}) and bridging (1770 - 1950 cm^{-1}) bound CO features, similar to those observed in the present study. Similarly, infrared studies of CO adsorption on technical catalysts also show characteristic atop and bridging features consistent with those observed in the present study.[83,220] Features associated with Rh gem dicarbonyl $Rh(CO)_2$ species (ν_{CO}, sym ~ 2090 - 2110 cm^{-1}, vCO, asym ~ 2020-2035 cm^{-1}) were not observed over the particle size ranges employed in this study. These additional CO stretching features have been observed in previous studies of highly dispersed, low temperature prepared Rh/Al_2O_3 model catalyst surfaces[223,224] and infrared studies of CO adsorption on technical catalysts surfaces under elevated pressure conditions.[83,220] Though found to be a rather inactive species for CO oxidation under elevated pressure

conditions (compared to atop- bridging bound CO)[69,226,227], the absence of these features in the CO-IRAS spectra allows additional insights into the nature of our particle surfaces. Coupled STM and CO-IRAS studies of Rh/Al_2O_3 model catalyst surfaces by Freund and co workers[223,224], prepared at low temperatures (T ~ 90 K) with sub-monolayer Rh coverages, exhibit a gem-dicarbonyl stretching feature near vCO = 2117 cm^{-1}, due to atomically dispersed $Rh(CO)_2$ species present at oxide defects. If Rh is deposited at T = 300 K, Rh atoms have sufficient surface mobility to form larger particles, eliminating the concentration of highly dispersed Rh species.[223,224] A similar picture has been observed in CO infrared studies of $Rh/TiO_2(110)$ model catalyst surfaces, which demonstrate high temperature treatments of Rh particles can eliminate dicarbonyl stretching features.[225] Infrared CO adsorption studies on bulk catalyst surfaces are qualitatively consistent with these observations.[83,220] A survey study by Trautmann et. al. of Rh clusters supported on various oxides (SiO_2, Al_2O_3, TiO_2) demonstrate gem-dicarbonyl CO features present in IR spectra. These stretching frequencies are essentially constant with increasing coverage (indicative of isolated sites) and tend to attenuate with increasing temperature, observations consistent with stretching features associated with isolated $Rh(CO)_2$-type species.[220] Studies by Cavanagh et. al. have also demonstrated via infrared studies of alumina supported Rh particles, that the presence of spatially isolated $Rh(CO)_2$ dicarbonyl species is prevalent on highly dispersed samples, which exhibit the characteristic gem-dicarbonyl stretching frequencies near v_{CO} = 2101 and v_{CO} = 2030 cm^{-1}.[83] It is likely the case that our surfaces contain Rh particle sizes too large and have been prepared at temperatures too high (T =

300 K) to produce a detectable concentration of dicarbonyl surface species, as these species appear to be associated with atomically dispersed Rh. This also suggests that CO induced disruption of our Rh particles (breakup of particles to form $Rh(CO)_2$)[33] is not detectable via CO-IRAS for the particle sizes employed, under the experimental conditions of the infrared studies. To summarize, low pressure CO IRAS studies of Rh/SiO_2 catalyst surfaces, prepared at T = 300 K across the ($<d_p>$ = 1 - 4 nm) range, exhibit CO species characteristic of atop bound (vCO = 2070 - 2075 cm^{-1}, at saturation T = 300 K) and bridging bound (vCO = 1875-1975 cm^{-1}) CO surface species, as observed previously in the literature.

Rh/SiO_2 STM Results

STM images were collected on Rh/SiO_2 samples in a separate STM/UHV system. An ultra-thin SiO_2 film (1 ML SiO_2, 3 Å)[228] was grown on a Mo(112) substrate, allowing for sufficient conductivity for STM imaging. Rh metal was vapor deposited on the sample at T = 300 K and images taken under UHV conditions at various Rh coverages (θ_{Rh} = 0.1 ML through 4.0 ML). Shown in **Figures 44** are four representative STM images (coverages of θ_{Rh} = 1.0, 1.5, 2.0, and 4.0 ML, resp.) from these studies. Rh particles appear as bright spots in the images, with mean Rh particle size increasing as a function of Rh coverage. Particle site densities calculated from the images show that as the Rh coverages is increased, the particle density increases slightly from 5 x 10^{12} particles/cm^2 to 3 x 10^{13} particles/cm^2. At or below 0.5 ML Rh coverage, small Rh particles partially wet the silica surface and form quasi-2D particles scattering across the surface. The majority of Rh particles have a thickness of approximately 1-2 layers.

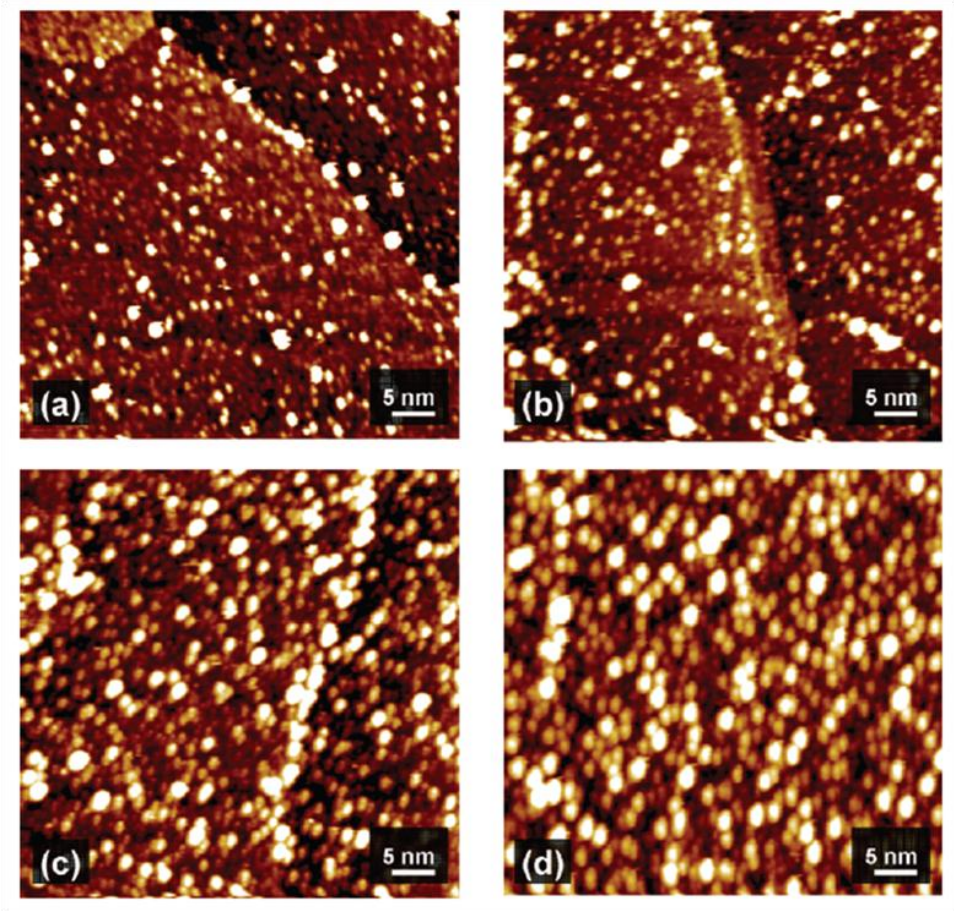

Figure 44. STM images for various Rh coverages (ML). Rh is deposited on on 1 ML SiO_2/Mo(112) films: (a) 1.0 ML Rh; (b) 1.5 ML Rh; (c) 2.0 ML Rh; (d) 4.0 ML Rh. Each panel is a 100 nm x 100 nm image.[12]

The apparent size of these quasi-2D Rh particles is influenced by the variation of sample bias during imaging and increases with the increase of sample bias at above +1.0 V. As the surface Rh coverage increases, Rh particles become 3D and exhibit a hemispherical shape. The apparent size of 3D Rh particles is not influenced by the sample bias, suggesting STM measures the topographic height of 3D Rh particles. The statistics on the particle height and diameter was then measured from these STM images of 100 nm x 100 nm in size. To remove the influence of tip apex in size measurement, we calibrated the measured particle diameter based on the Rh deposition rate. Assuming *(1)* the sticking probability of Rh on the thin silica film is 1 and *(2)* all Rh particles were exaggerated by the same factor, χ, due to the tip apex, we normalized the total calculated volume of Rh particles to the total deposition volume of Rh, by solving the equation, $\sum_{i=1}^{n} \frac{\pi h_i[3(r_i\chi)^2 + h_i^2]}{6} = V_{dep}$. The volume equation of a spherical cap, $\frac{\pi h[3r^2 + h^2]}{6}$, is used here to calculate the volume of each Rh particle. V_{dep} is the amount of deposited Rh, calculated from the flux rate of Rh times the deposition time. The flux rate of Rh is 0.045 ML/min, calibrated by AES breakpoint analysis on the clean Mo(112) surface. Rh AES breakpoint analysis in the STM chamber showed results similar to breakpoint analysis in the reactivity chamber (breakpoint at an AES ratio of Rh/Mo ~ 0.5). The assumption *(1)* on the sticking probability of Rh should be valid, at least, for high Rh coverages. The height over the calibrated particle diameter gives a ratio about 0.4, consistent for particles of all sizes and suggests Rh particles formed a pseudo-hemispherical shape at the silica film surface.

Shown in **Figure 45** are representative particle histograms (particle count vs. d_p(nm)) for 0.5, 1.0 ML, and 2.0 ML model catalyst surfaces. Shown in the inset of 45 is a representative STM images for the 0.5 ML Rh/SiO_2 surface. Histogram data can be analyzed to determine the average particle size $<d_p>$ and standard deviation (σ) for the as-prepared samples. Shown in **Figure 45** is the average Rh particle diameter (nm) vs. Θ_{Rh}, obtained from particle histograms collected from STM images of Rh/SiO_2 samples of varying Rh coverage (Θ_{Rh}), over the Θ_{Rh} = 0.25 ML - 4.0 ML coverage range. As the data illustrate, mean particle size of the Rh particles (bright spots in the image) and σ increase as a function of Rh coverage. The largest change in particle size occurs between 0.25 ML and 1.0 ML Θ_{Rh} coverages, which corresponds to a change from 1.0 to 2.9 nm diameter particles, respectively. Particle heights measured from the Rh/SiO_2 surfaces indicate an aspect ratio (h/d_p) of approximately 0.4, consistent for particles of all sizes, and suggest Rh particles form a pseudo-hemispherical shape at the silica film surface. As further characterization data and analyses will demonstrate, **Figure 45**(d) can provide a relation between average particle size and Θ_{Rh} of model surfaces used for elevated pressure kinetic studies.

Based on the calibrated particle height and diameter, a geometric estimate of the total surface sites of the UHV prepared sample (pre-reaction) can be calculated based on the equation for the spherical cap surface, $A = 2\pi rh$ for the Rh coverages in **Figures 44**, assuming a surface atom density of 1.6 x 1015 atoms/cm2 (Rh(111) surface atom density). Also calculated are the active site density assuming less-densely packed facets for the Rh particles (Rh(100) = 1.45×10^{15} atoms/cm^2 and Rh(110) = 9.8×10^{14}

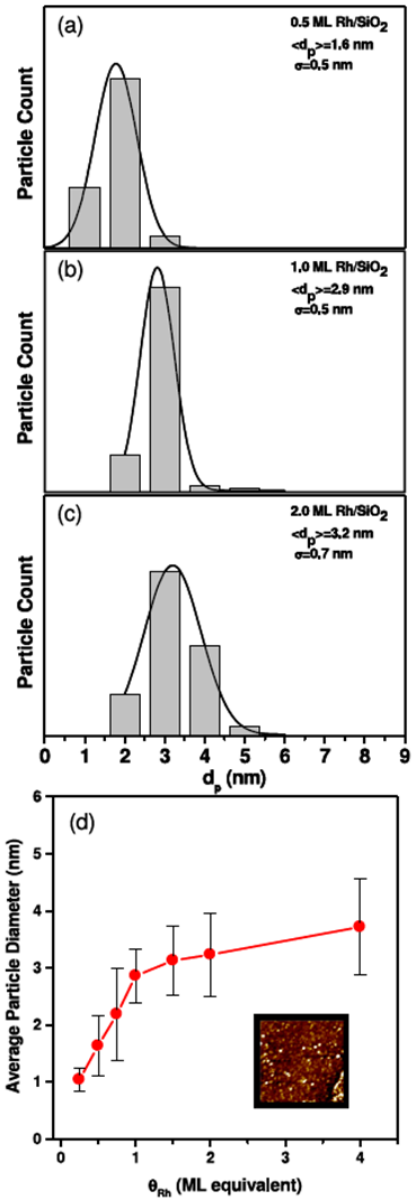

Figure 45. Particle histogram data for various Rh ML coverages on SiO_2. (a)-(c). Particle histogram data (Particle Count vs. d_p(nm)) for 0.5, 1.0 ML, and 2.0 ML Rh/SiO_2 surfaces, respectively. Average particle diameter $<d_p>$ and standard deviation of the distribution are reported for each coverage. Inset: Representative STM image of the 0.5 ML Rh/SiO_2 surface (Image size: 50nm x 50 nm). (d). Average particle diameter (nm) vs. θ_{Rh} (ML) obtained from histogram data for 0.25 ML to 4.0 ML Rh/SiO_2 samples. Error bars represent standard deviation as determined from particle histogram data at each θ_{Rh}.[10]

atoms/cm^2). The result of this calculation is shown in **Figure 40** (▲ symbol). Also displayed in **Figure 40** are the mean particle diameter (in Å, ■ symbol) and standard deviation (error bars) calculated from the histogram data obtained from the θ_{Rh} = 0.1 ML through 4 ML images, along with the minimum and maximum particles sizes observed for each coverage (---- dotted lines). As the data illustrates, the mean diameter of the particles as measured by STM increases from d_p = 10 Å at 0.1 ML Rh to d_p = 35 Å for 4 ML Rh coverages, with an increasing spread in particle size as Rh coverage increases. It should be reiterated that STM images were taken on ultra thin (1 ML, 3 Å) SiO_2 films to achieve sufficient conductivity for imaging, whereas CO TDS and reactivity measurements were obtained on thicker (5 ML, 15 Å) SiO_2 films. While it is unclear whether there exists substantial differences in the nucleation and growth or behavior of Rh particles with respect to SiO_2 film thickness, these data provide the best means at present to image particle sizes on similarly grown samples, and will be used in our discussion.

Rh Coverage Dependent Reactivity Measurements

Shown in **Figure 46** are reactivity measurements [molecules CO_2 formed/sec vs. 1000/T(K)] obtained from a series of Rh/SiO_2 model catalyst samples with varying Rh coverage (θ_{Rh} = 0.25 through 10 ML) using a (1/10) O_2/CO gas mixture, along with data obtained from the Rh(111) single crystal. As the data illustrate, increasing Rh coverages results in an increased rate of CO_2 formation as expected. Temperature dependence shows Arrhenius behavior for the temperatures and coverages studied, exhibiting an activation energy of E_a = 100 - 110 kJ/mol for all coverages studied. This value is in

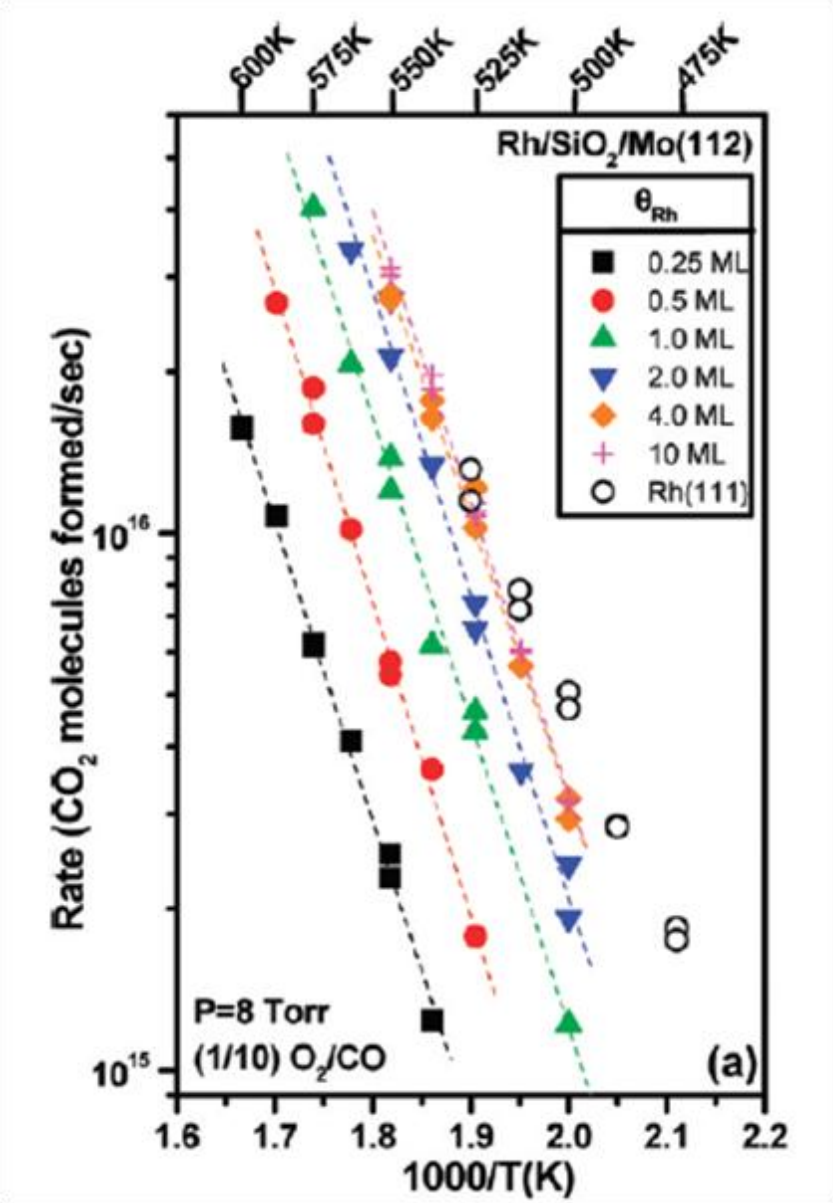

Figure 46. CO_2 reaction rate data vs. 1000/T(K), for various Rh coverages on SiO_2. (■) 0.25 ML; (●) 0.5 ML; (▲) 1.0 ML; (▼) 2.0 ML; (♦) 4.0 ML; (+) 10 ML. CO_2 reaction rate data obtained over Rh(111) (○), conducted under the same reaction conditions. Typical error in reactivity measurements, based on replicate measurements, is ±10%.[12]

good agreement with the consensus of literature values (E_a = 100 - 120 kJ/mol) obtained on Rh single crystals and technical catalysts.[66,67,69,70] This observation strongly suggests that, similar to Rh(111) surfaces, under the conditions (P, T, O_2/CO ratios) of **Figure 46**, the reaction rate is limited by CO desorption (~ CO binding energy). This is a key point, which we believe indicates that under the (1/10) O_2/CO gas mixture conditions, the active portion of the Rh particle surface is primarily dominated by CO species, such that CO desorption remains the rate limiting step for reaction. Experiments conducted with the (1/10) O_2/CO mixture under the conditions shown in the figure, demonstrated repeatable behavior (i.e. samples could be run repeatably throughout the temperatures ranges with negligible changes to the measured reaction rate). Replicate measurements displayed for several of the conditions in the figure demonstrate the repeatability of the measured reaction rate upon repeated reaction. In other words, reactions can be run a number of times throughout the linear reactivity range, with repeated measurements producing similar TOF values within expected error. This suggests that, whatever oxidation and/or sintering is occurring after exposure to high pressure reaction conditions (after exposure to O_2/CO gas mixture and heating to reaction temperature), does not appear to substantially affect the reaction rate (CO2 molecules produced/sec). Although, it should be noted that changes in particle morphology could occur upon exposure of Rh particles to reaction mixture prior to reaction. As will be discussed shortly, deactivation occurred with respect to activity as the temperature and or O_2 partial pressure of the gas mixture increased to a critical point (T > 600 K with (1/1) O_2/CO).

Catalytic activity is typically defined in terms of TOF (molecules CO_2 produced per site per second). CO oxidation on Rh single crystal and technical catalyst surfaces under similar CO dominant conditions has been shown to exhibit structure insensitive kinetics.[66,67,69-71,182] Thus, a plot of the $Rh/SiO_2/Mo(112)$ and Rh(111) data of **Figure 46** in terms of TOF will be coincident for a structure insensitive reaction. The $Rh/SiO_2/Mo(112)$ and Rh(111) reactivity data of **Figure 46** can be utilized to obtain an estimate of the number of active sites present on the Rh/SiO_2 as a function of Rh coverage. Since the Rh(111) reactivity data in **Figure 46** has been obtained on a single crystal sample (Rh(111) surface density 1.6×10^{15} atoms/cm^2, single crystal area = 1.5 cm^2 front and back), $Rh/SiO_2/Mo(112)$ data can be normalized to the Rh(111) single crystal data to obtain estimates of the number of active Rh sites. This exercise is visualized in **Figure 47**, which is an Arrhenius plot of the data of Figure 46 in terms of TOF, where $Rh/SiO_2/Mo(112)$ reactivity data for the various coverages has been normalized by an appropriate number of sites such that the plots are normalized to the Rh(111) single crystal data (linear least squares fit). The number of sites obtained from normalization are shown in the figure for the coverages (θ_{Rh} = 0.25 through 10 ML). The calculated activation energy obtained from normalization of all the Rh particle and Rh(111) single crystal data (dotted line) is $E_a = 100 \pm 3$ kJ/mol. Based on repeated measurements on samples with an identical Rh coverage, we estimate that the value obtained by this method has an error ± 20% to the quantitative value reported. As one would expect, the number of active Rh sites increases with increasing Rh coverage, and

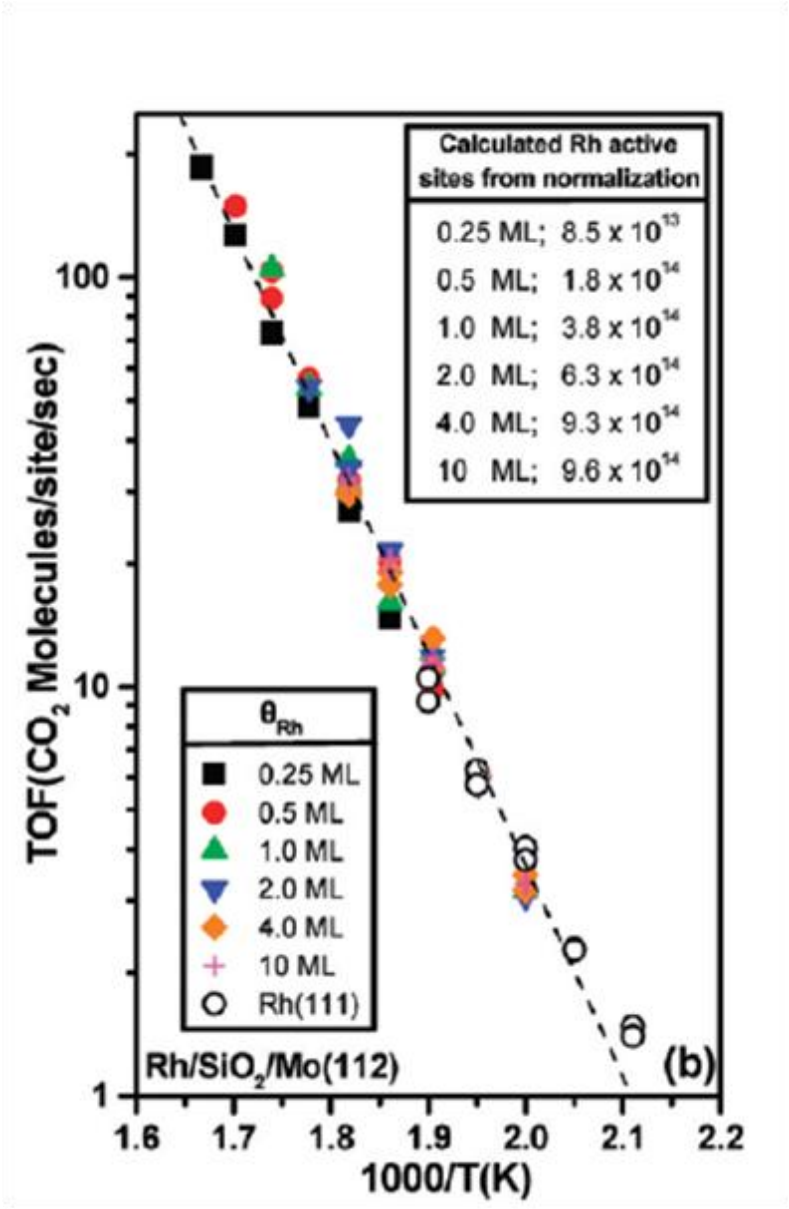

Figure 47. CO_2 reaction rate (molecules/s) normalized to Rh(111) to obtain a rate in terms of CO_2 molecules/site/s. (■) 0.25 ML; (●) 0.5 ML; (▲) 1.0 ML; (▼) 2.0 ML; (♦) 4.0 ML; (+) 10 ML; (○) Rh(111). Each set of Rh coverage reaction data was linear best fit to the Rh(111) reaction data. The calculated activation energy obtained from normalization of all the Rh particle and Rh(111) single crystal data (dotted line) is E_a = 100 ± 3 kJ/mol. Typical error in reactivity measurements, based on replicate measurements, is ±10%.[12]

approaches the number of sites present on one side of our Rh(111) sample (1.2 x 10^{15} sites). (Note: Rh particles are deposited on only one side of the SiO_2/Mo(112) sample).

O_2/CO Gas Mixture Dependent Reactivity Measurements

Reactivity measurements were conducted using various gas mixture compositions (O_2/CO) to investigate the (O_2/CO) dependencies of the CO_2 oxidation reaction on the Rh/SiO_2 catalyst surfaces. Shown in **Figure 48** are reactivity measurements (TOF vs. 1000/T(K)) obtained on Rh/SiO_2/Mo(112) samples (with a constant Rh coverage of θ_{Rh} = 0.25 ML) and comparable Rh(111) single crystal for various gas mixtures (1/1, 1/2, 1/5, and 1/10 O_2/CO). Particle data are normalized to the number of sites calculated from the data of **Figure 47** for θ_{Rh} = 0.25 ML equivalent sample (N = 8.5 x 10^{13} active Rh sites). As **Figure 48** illustrates, the data exhibit similar (O_2/CO) dependencies (positive order in O_2, negative order in CO) as seen on the Rh single crystal data and previous[66,67,69-71,182] technical catalyst studies, as evidenced by increase in reaction rate as a function of increased O_2 partial pressure. Activation energies for the (1/10) through the (1/1) O_2/CO gas mixtures exhibit similar reaction activation energies between E = 100 - 110 kJ/mol, suggesting that, under these conditions, the reaction rate is still primarily dictated by the rate limiting step of CO desorption under these particular elevated pressure conditions. Furthermore, when normalizing data for the (1/10) to (1/2) gas mixtures by the number of Rh sites obtained from **Figure 47**, TOF data agree very well with data obtained on the Rh(111) single crystal. Likewise, Rh(111) single crystal data obtained at (1/1) O_2/CO exhibit TOF values consistent with previous studies.[182] Out of the four gas mixtures employed in

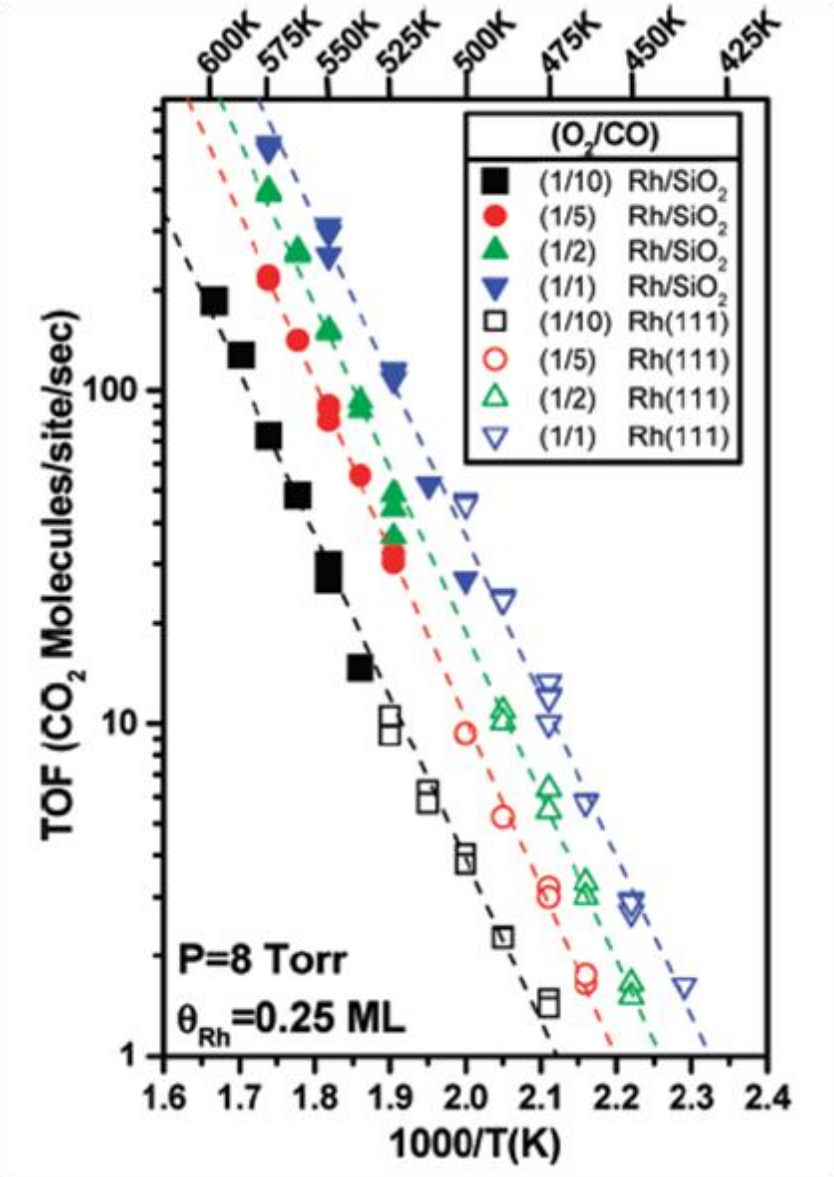

Figure 48. CO_2 reaction rate data (molecules/site/s) vs. 1000/T(K) for various O_2/CO gas mixture over 0.25ML Rh SiO_2. (■) (1/10) O_2/CO; (●) (1/5) O_2/CO; (▲) (1/2) O_2/CO (▼) (1/1) O_2/CO. Shown as open symbols are corresponding reaction data taken on Rh(111) single crystal sample: (□) (1/10) O_2/CO; (○) (1/5) O_2/CO; (Δ) (1/2) O_2/CO (▽) (1/1) O_2/CO. Particle data is normalized using the number of site estimate obtained for θ_{Rh} = 0.25 ML coverage in Figure 1. Typical error in reactivity measurements, based on replicate measurements, is ±10%.[12]

Figure 48, the Rh particle data for the (1/1) O_2/CO mixture (though still exhibiting fair agreement) showed a slight deviation from the Rh(111) single crystal data. TOF values over the Rh/SiO_2 surface under these reaction conditions showed TOF slightly lower than would be expected for the normalization, suggesting the number of Rh active sites are less than that calculated in **Figure 47** for the (1/10) O_2/CO gas mixture. This is consistent with (a) a reduction in the number of active Rh sites available for reaction or (b) a decreased activity in the active site(s) on the Rh particle. First, sintering due to thermal/pressure treatment could involve the reduction of number of active sites at higher O_2/CO ratios and temperatures. Several studies on model surfaces have demonstrated that Rh particles can exhibit agglomeration, dispersion and morphology/shape effects on a variety of supports [theoretical[228], (MgO)[229], (TiO_2)[33,207-209], (Al_2O_3)[224]] as a result of gas ambients (CO, O_2) and/or thermal treatments. For the specific case of Rh/SiO_2, ISS/XPS experiments by Kohl et. al. have demonstrated thermally induced agglomeration of Rh particles deposited on a Rh/SiO_2/Mo films under UHV conditions.[206] Additional work by Knözinger and coworkers[205] have also shown similar behavior for the Rh/SiO_2 surface. Particle sintering of Rh/SiO_2 samples, at high temperatures and O_2/CO ratios, could be a contributor to the slightly lower reaction rates observed for the (1/1) O_2/CO measurements of **Figure 48**.

A second possibility could be the increased oxidation of Rh particles, especially if particles or particle surface(s) are completely oxidized to bulk Rh oxide (Rh_2O_3). While current debate surrounds the nature of reactivity of Pt group metal surface oxides[72,181,183,184] compared to chemisorbed oxygen phases, it is generally accepted and

observed that *bulk* oxides of Rh are less reactive than chemisorbed oxygen surfaces for CO oxidation reactions.[182,183] Bulk oxidation of small Rh particles, or rough particle surfaces, could result in lower reaction rates flkjhor (O_2/CO) ≥ 1 mixtures. It has been shown in previous studies that in O_2 and O_2/CO environments, Rh particles can undergo changes in oxidation state and morphology. Electron microscopy and diffraction studies by Rupprechter et. al.[199] of alumina supported Rh particles have shown that while little change in particle morphology occurs upon annealing in vacuum to T = 725 K, annealing particles in 1 bar O_2 at T = 575 K showed thin oxide formation on the particle surfaces; heating to T = 675-725 K resulted in an increased thickness of oxide surrounding the metallic particle core. Reduction of oxidized particles (1 bar H_2) at low temp T = 525 K produced polycrystalline particles and Rh/Rh_2O_3 layers particle surfaces; increasing reduction treatment to T = 725 K resulted in more fully reduced particles. Dudin et. al. examined changes in particle morphology and oxidation states of Rh/MgO systems (Rh particles and films) upon exposure to O atom plasma (P ~ 10^{-6} mbar; T = 450 - 500 K) and hydrogen reduction (P ~ 5 x 10^{-6} mbar, T ~ 490 K). Rh particles were found to be rather heterogeneous with respect to oxidation state (even within the same particle), indicating that the nature of an oxidized catalyst surface can be quite heterogeneous, despite identical oxidation conditions.[210] Oxidation and reduction treatments can also alter the surface morphology of Rh single crystal and technical catalyst surfaces.[117,230] EXAFS studies of bulk Rh/Al_2O_3 catalysts during elevated pressure CO oxidation reactions by Newton et. al. have shown that Rh particles can rapidly oxidize at room temperature upon exposure to O_2. However, during reaction

conditions, the O_2/CO gas feed ratio plays an important role in the oxidative state of the particles. For ratios O_2/CO < 1 and T > 450 K, particles are largely metallic; under oxygen rich conditions, an oxide Rh phase dominates the catalyst surface. Under both reducing and oxidizing conditions, 100% conversion of the O_2/CO gas feed can still be achieved, indicating both surfaces can be active for CO oxidation.[231]

Studies on supported Pd systems offer additional data for comparison. Penner et. al.[232] have demonstrated oxidation of Pd particles on Al_2O_3(0001) to PdO (small particles) and a thin PdO film (on large particles) under high (25 Torr) O_2 pressures and moderate temperatures (T ~ 400 K). Experiments conducted by Hayek and coworkers[233,234] demonstrate using SAED and HR-TEM that under P = 1 bar O_2, T = 673 K conditions, Pd/SiO_2 particles disperse and form a PdO phase, with PdO growth occurring on top of Pd particles. [233] Reduction in pure CO (P ~ 10 mbar at T = 525 K) was required to achieve reduced particles. Recent studies of well defined Pd particles (created by organometallic decomposition) supported on MgO powders have allowed for FTIR investigations under ambient O_2/CO reaction conditions near 150°C.[235] These results indicated that, under CO rich gas mixtures (O_2/CO < 2), adsorbed CO can be observed on Pd particles via FTIR indicating a CO rich surface; under oxygen rich mixtures (O_2/CO > 2), CO IR features are not observed, indicating a CO deficient surface.

To further investigate the changes in rate measurements observed for high oxygen ratios on Rh nanoparticles, additional experiments were run at higher temperatures using an oxygen-rich (1/1) O_2/CO mixture, in an attempt to probe reaction

conditions which result in further oxidation of Rh particles. Shown in **Figures 49** are a series of measurements conducted on 0.25 ML Rh/SiO_2/Mo(112) samples. In panel (a), Rh reactivity measurements show repeatable behavior over the linear range, with repeated TOF values within measurement error. As the reaction temperature is increased to T = 600 K, the reaction rate begins to roll over and subsequent reactions (denoted by numeric order) at high temperatures begin to exhibit decreasing reaction rates. To further investigate this effect, an identical sample (0.25 ML Rh/SiO_2/Mo(112)) was prepared and reactions run in a similar fashion, as shown in **Figure 50**. Reactions were repeatable over the linear CO inhibited range as shown in **Figure 49**. A reaction (1) was then immediately run at high temperature (T = 650 K), followed by a reaction (2) at T = 525 K. As the data illustrates, the reactivity of the sample has decreased. Furthermore, the reactivity of this experiment at T = 650 K is higher than the T = 650 K measurements of **Figure 49**; this is consistent with deactivation due to reaction conditions at these higher temperatures. The **Figure 50** sample is then heated in P = 8.0 Torr pure CO (red arrow) at T = 525 K and a reaction (3) is run again on the sample at T = 525 K; as the results show nearly ~80 - 90% of the reactivity was reclaimed due to the CO reduction treatment. These results indicate that the Rh particles undergo deactivation at sufficiently high temperatures and oxidizing conditions. The reclamation of catalytic activity, upon reduction in pure CO, suggests that a substantial portion of deactivation is due in part to particle oxidation. For the case of θ_{Rh} = 0.25 ML Rh particles, this point appears to occur at T > 600 K for (1/1) O_2/CO mixtures; deactivation conditions could be expected to differ for different Rh coverages. These observations are qualitatively

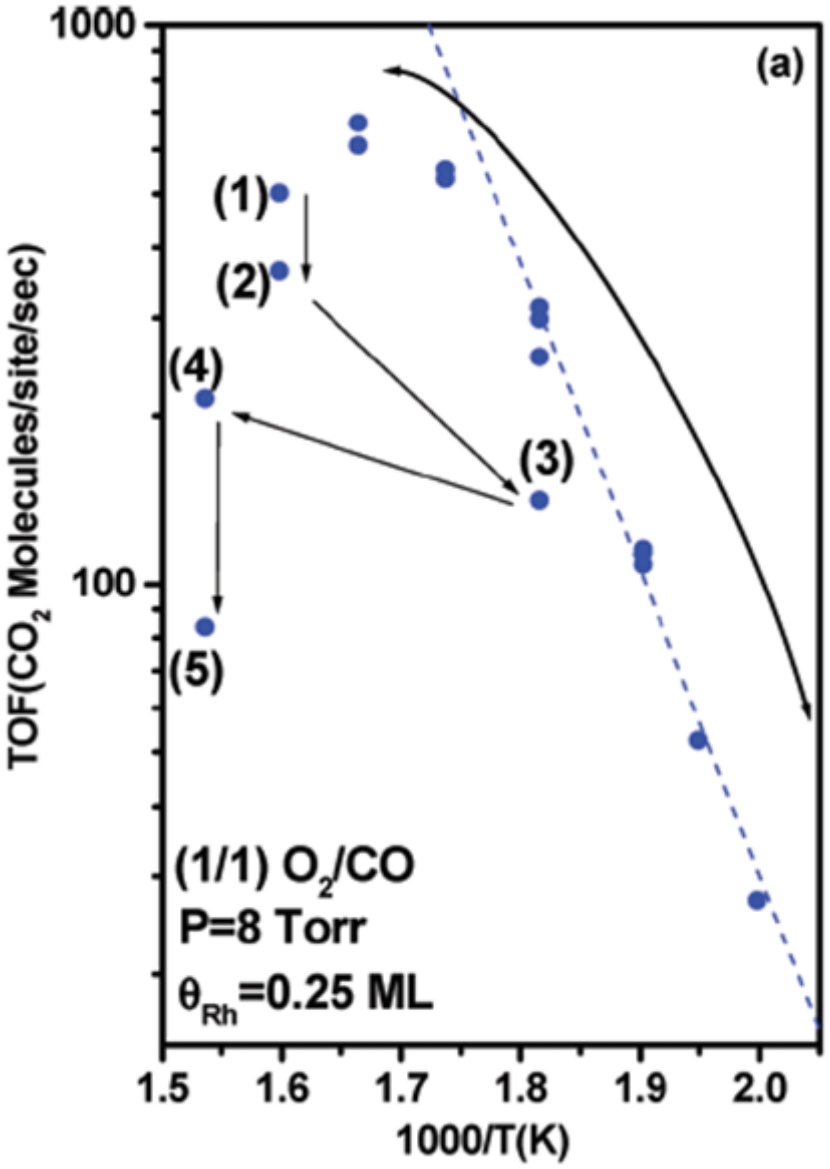

Figure 49. High temperature reactions run over 0.25ML Rh with (1/1) O_2/CO. Deactivation at higher temperatures run in sequential order (1-5). TOF normalized to number of Rh sites obtained from 1/10 O_2/CO experiments over θ_{Rh} = 0.25 ML.[12]

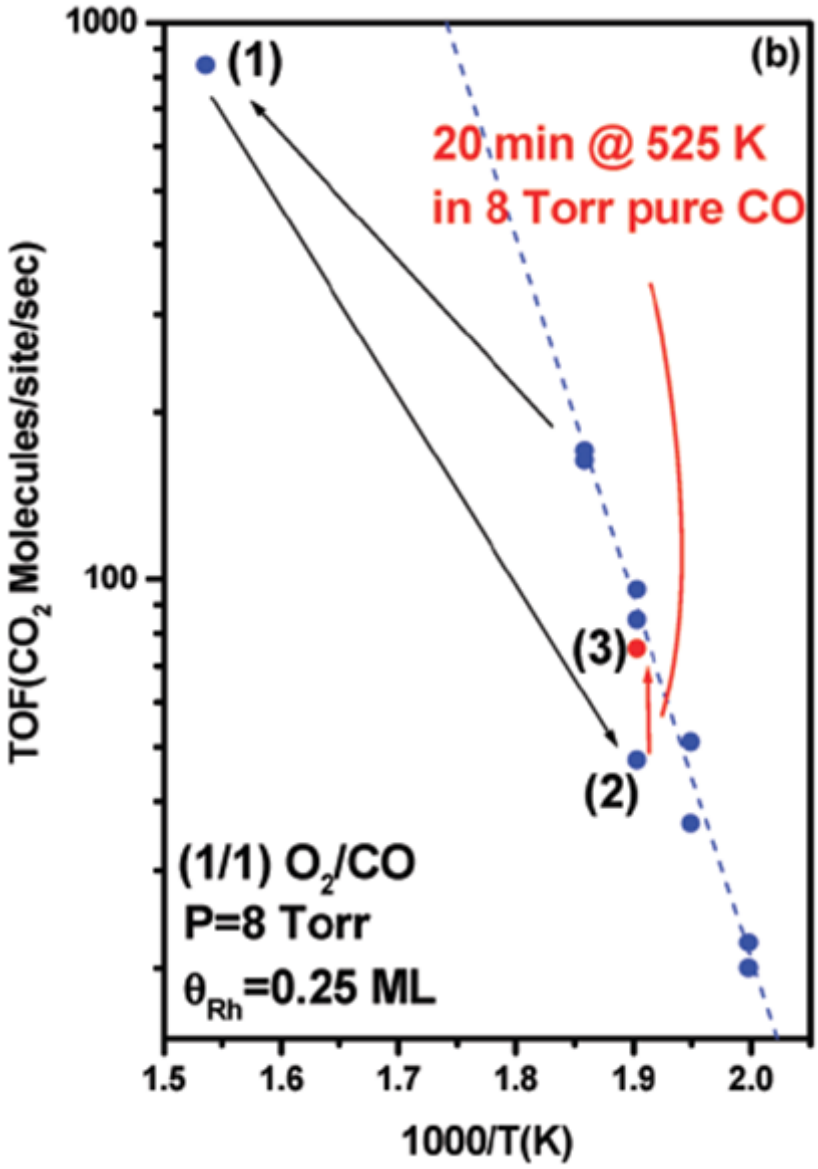

Figure 50. θ_{Rh} = 0.25ML $Rh/SiO_2/Mo(112)$ sample run with (1/1) O_2/CO mixtures. Deactivation at higher temperatures run in sequential order (1)-(3). Between (2) and (3) a 20 min reduction in P = 8.0 Torr pure CO at T = 525 K is conducted. TOF normalized to number of Rh sites obtained from (1/10) O_2/CO experiments over θ_{Rh} = 0.25 ML.[12]

consistent with previous oxidation (under oxygen rich, moderate/high temperature environments) and reduction (under CO/H_2 reducing environments) observed on Pd[232,233] and Rh particle samples[199,210], discussed earlier.

Under steady-state pressure and temperature conditions which produce CO rich surfaces (such as the 1/10 O_2/CO reaction conditions employed in most of our measurements), substantial deactivation of the particles due to oxidation appears to be minimal or not detectable. Once the surface CO coverage decreases at higher temperatures, particle oxidation can occur more easily under reaction conditions. Whether the deactivation of Rh particles shown in **Figure 49** is due to surface or bulk oxidation (or a mixture) of the Rh particles cannot be conclusively ascertained from this data. It is plausible that such a high temperature treatment could have resulted in complete (bulk) oxidation of the Rh particles. Work on Pt-group metals currently underway may shed further light on this oxidation deactivation. Pt and Pd particles, metals more resistant to bulk oxidation, may exhibit oxidation induced deactivation at higher temperatures and/or O_2 pressure conditions.

Comparison Between TDS, STM, CO Oxidation

Shown in **Figure 40** is a plot of number of Rh active sites per cm^2 as calculated from the TDS measurements, STM, and reactivity data. As the data of **Figure 40** illustrate, Rh site measurements from both CO-TDS and reactivity measurement techniques show fairly good agreement, with both approaching the value for the Rh(111) surface (1.6×10^{15} atoms/cm^2), as one would expect. Estimates across the coverage ranges studied by both methods agree quite well, within a factor of 2 over the Rh

coverage range. For STM, this method appears to predict a higher number of sites than the reaction measurements. STM estimates using Rh(111) surface atom density slightly overestimates the number of active sites present on the Rh/SiO_2 surface. Estimates employing Rh(100) and Rh(110) surface atom densities (facets more characteristic of smaller particles) begin to approach the reactivity and TDS data to provide better agreement, though are still overall slightly higher. We speculate that this slight disagreement likely arises from the simplifying assumptions associated with the geometric STM estimation method. CO TDS and CO reactivity measurements show good agreement with one another. This could be due to particle morphology changes (agglomeration or sintering) which could occur upon exposure to reactive gas mixture and heating of the Rh/SiO_2 sample, as has been observed in other Rh model catalyst studies discussed previously, as the STM images are taken immediately after Rh deposition at T = 300 K. Despite these differences, it is surprising to observe that site estimates derived from all three methods fall roughly within a factor of ~3 of one another, and track well with increasing Rh coverage.

It is clear from the data of **Figure 40** that better agreement is achieved between the site estimates from reactivity and TPD measurements. This is could be due to the fact that COTDS and CO reactivity measurements provide a more direct measure of CO adsorption sites on the Rh particles, whereas the STM estimates arise from a geometric argument containing several simplifying assumptions. One could also speculate that this agreement results from the similar temperature treatments on the TPD (heating to T = 700 K) and reactivity measurements (heating to T = 600 K). However, the differing

environments of these two methods (reactivity measurements, P = 8.0 Torr; TPD measurements, P = 10^{-7} - 10^{-6} Torr) makes conclusive statements on this difficult at present, in light of the dispersion/agglomeration behavior observed in previous Rh particle studies discussed earlier.

Taken together, we interpret these results to indicate that careful reactivity experiments conducted under rich CO gas mixtures can provide a reasonable method to measure Rh active sites for CO oxidation from TOF values. The results demonstrate that Rh/SiO_2 model catalysts can be effectively employed to gain both quantitative and qualitative insights into reaction kinetics at elevated pressures. This indicates that the method of **Figure 47** can be used to characterize Rh/SiO_2 samples for use in surface sensitive reactions, reactions whose selectivity and activity are a function of particle size and morphology.

Summary

In summary, an initial study of CO oxidation activity on $Rh/SiO_2/Mo(112)$ catalyst surfaces prepared and studied in situ under relevant temperature and elevated pressure conditions has been presented. Reactivity was studied primarily under CO rich reaction mixtures to investigate reaction kinetics. Our primary conclusions, under the experimental conditions investigated, are as follows:

Results demonstrate that CO oxidation reaction on $Rh/SiO_2/Mo(112)$ model catalyst samples exhibit similar O_2/CO dependencies (negative in CO, positive in O_2), activation energies, and TOF values as observed in previous studies on Rh surfaces, under reaction conditions used. To the best of our knowledge, this is the first attempt to

directly compare elevated pressure CO oxidation reaction kinetics on Rh model catalyst surfaces to Rh single crystal surfaces (prepared entirely in situ in UHV) under identical reaction and reactor conditions. The tandem use of model catalyst surfaces and well-defined single crystal surfaces under identical reaction conditions can provide useful insights into behavior of model catalyst surfaces.

Estimates of Rh active sites based on reaction rates under CO dominant conditions (1/10) O_2/CO are in good agreement with estimates obtained from TPD measurements. STM images obtained for Rh particles deposited on ultra thin SiO_2 film at T = 300 K provide estimates in active sites within a factor of ~3 of reactivity and TPD measurements. The good agreement of the TPD and reactivity measurements, and the broad agreement of all three methods indicate that CO oxidation measurements, run under CO-rich conditions, can provide a reasonable estimate of the number of active sites present on a Rh model catalyst sample. Such characterization will be useful for future studies of particle and structure dependent reactions on model catalyst surfaces.

Sample deactivation, consistent with oxidation, begins to occur at higher temperatures (T > 600 K) and O_2/CO ratios > (1/1) for θ_{Rh} = 0 .25 ML. Particle reactivity can be partially recovered by reduction in pure CO.

Ethylene Hydroformylation

The C_2H_4+CO+H_2 system presents an interesting probe reaction to investigate a surface reaction (CO insertion into adsorbed R-C_2H_5 alkyl groups) whose selectivity, surface adsorbates, and surface morphology can all potentially depend on the initial Rh particle size and the reactant gas conditions. In the present study[236], we aim to gain

insights into the structure-activity relationships of the $CO+C_2H_4+H_2$ reaction on oxide supported Rh nanoparticle surfaces. Our primary goal is to understand the structure-activity relationships of the CO insertion pathway during C_2H_4 hydroformylation, the underlying reasons driving these structure-activity relationships, and the role of elevated pressure reactant gas in altering the morphology and surface adsorbates present on supported Rh NPs. To accomplish this task we employ well-defined Rh/SiO_2 silica model catalyst surfaces[10,12] to conduct reaction and spectroscopic measurements at elevated pressures (near atm). These surfaces enable careful study of the reactivity and selectivity as a function of Rh particle size; complementary spectroscopic investigations under ambient gas and reaction conditions (polarization modulation infrared adsorption spectroscopy, PM-IRAS) enable insights into Rh particle morphology and the state of surface bound CO under reaction conditions as a function of particles size.

Characterization of Rh/SiO_2 dispersion under UHV and near atmospheric pressures

Details of Rh/SiO_2 STM particle size, active site characterization[12], and percentage of undercoordinated atoms[51] have been discussed in detail in previous investigations. In **Figure 51**(a), we present fraction of undercoordinated atom surface sites (≤ C7 coordinated sites[49]) as a function of Rh particle size based on hard sphere counting models and STM particle size distribution data[51]. C_4H_{10} hydrogenolysis ($C_4H_{10}+H_2 \rightarrow CH_4$, C_2H_6, C_3H_8) is a well-studied, structure sensitive reaction[117,237], which we employ here as a probe reaction to correlate STM measurements of Rh particle size at UHV pressures with reactivity measurements at elevated pressures on Rh/SiO_2 surfaces. As shown in previous studies, C_2H_6 selectivity from C_4H_{10} hydrogenolysis is

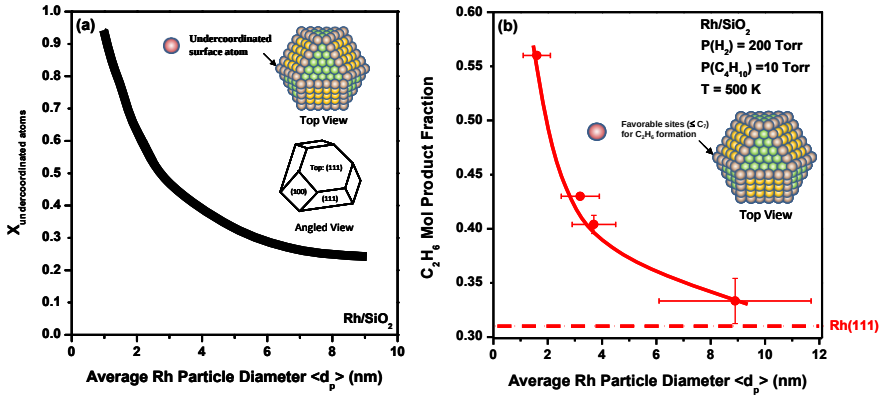

Figure 51. Rh/SiO_2 particle size characterization using hard sphere counting models and C_4H_{10} hydrogenolysis. (a): Estimates of undercoordinated Rh surfaces sites ($\leq C_7$ coordinated surface atoms) from simple hard sphere counting models (truncated cubooctahedron particles, see inset example). (b): C_2H_6 mol. fraction from C_4H_{10} hydrogenolysis probe reactions as a function of particle size. Reaction conditions: (T=500 K, P=210 Torr, P_{H_2}:$P_{C_4H_{10}}$=20, low conversion < 2%). Red dashed line shows C_2H_6 mol fraction obtained on a Rh(111) surface under identical conditions.[236]

known to be highly favored on undercoordinated surface atoms on Rh metal surfaces.[117,237] Since the percentage of undercoordinated atoms increases rapidly as NP size decreases below dp < 5 nm[49], this reaction will provide a qualitative probe of particle dispersion under near atm pressures on Rh/SiO_2 surfaces. Shown in **Figure 51**(b) is a plot of C_2H_6 product mol fraction (●) versus average Rh particle size (nm) (Reaction conditions: T=500 K, P=210 Torr, H_2 :C_4H_{10} = 20:1). As shown, C_2H_6 product mol fraction sharply increases as average Rh particle size is decreased below d_p < 5 nm, exhibiting good correlation between undercoordinated Rh site estimates from STM data based on hard-sphere models. Additionally, overall C_4H_{10} TOF and C_2H_6 selectivity vs. particle size behavior (not shown) exhibit good agreement with expectations from technical catalyst studies.[117] These characterization results serve to illustrate two key points: (1) Rh particle size estimates obtained via STM measurements correlate well with elevated pressure kinetic measurements of a well-defined probe reaction and (2) reactivity data which will contrast with the Rh particle size dependence observed under $C_2H_4/CO/H_2$ reaction environments, where the reactant gas will play a role in altering surface morphology and binding of adsorbed reactants.

C_2H_4 Hydroformylation Reactivity Data

Shown in **Figure 52**(a) is a plot of propionaldehyde TOF versus average Rh particle size, under standard $C_2H_4/CO/H_2$ reaction conditions at T=500 K. All reactivity measurements were obtained on freshly prepared Rh/SiO_2 surfaces, to avoid convoluting the data with deactivation effects. Reactivity of a Rh(111) single crystal surface, under identical conditions, is shown by the dotted line. As the data illustrates, a particle size

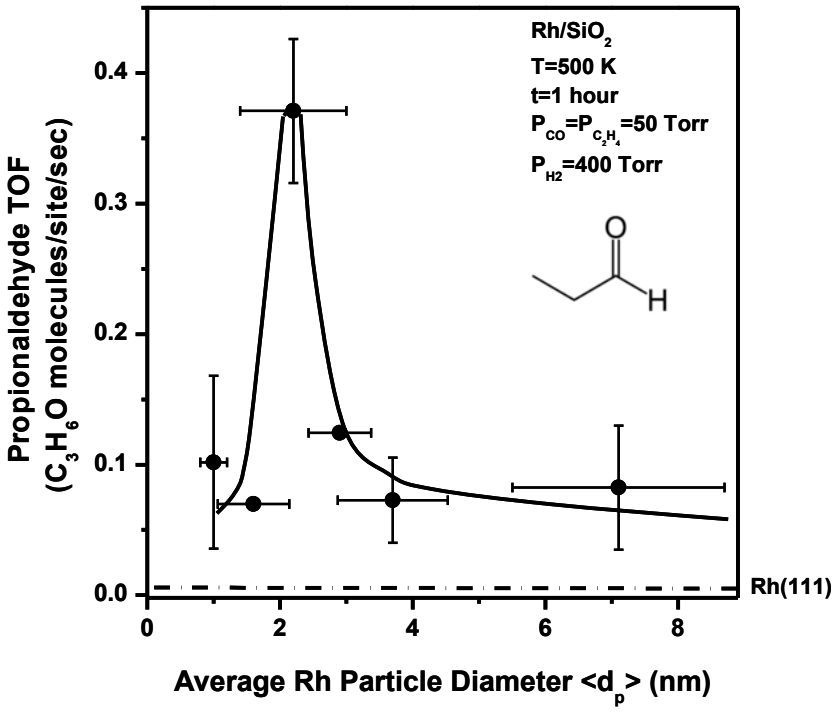

Figure 52. Propionaldehyde formation rate (TOF) vs. Rh particle size. Reaction conditions: 50 Torr CO : 50 Torr C_2H_4 : 400 Torr H_2 at T = 500 K for 1 hour. $\pm\sigma_y$ error bars represent error of repeated reactivity measurements, $\pm\sigma_x$ error bars represent the sigma of the particle size diameter of the Rh particle distribution as determined from STM measurements[24]. Smooth line present to guide the eye.[236]

effect is observed, with a maximum in propionaldehyde TOF (**Figure 52**, (●)) occurring near an average Rh particle diameter of ~ 2.5 nm. C_2H_6 production (not shown) exhibited a rather monotonic behavior until 2.5 nm, at which point a sharp increase in ethane formation is observed; C_2H_6 production for the smallest particle size studied (1.6 nm), showed lower C_2H_6 formation. Overall, Rh/SiO_2 surfaces show nearly an order of magnitude increase in propanal formation when compared to Rh(111) surface (dotted line). Additional products present in the product distribution included C4- hydrocarbon products and small amounts of CH4, C3-, and C5- hydrocarbon products. Additional kinetic measurements investigating the partial pressure and temperature dependencies will be presented in a complementary manuscript.[236]

CO PM-IRAS Measurements on Rh/SiO_2 Surfaces

To understand the effects of elevated pressure gases on Rh/SiO_2 surface morphology, we begin by examining pure CO infrared on Rh/SiO_2 as a function of Rh particle size. Shown in **Figures 53**(a) - (c) are low to elevated pressure CO PM-IRAS measurements obtained on various Rh/SiO_2 surfaces at T= 400 K, as a function of initial Rh particle size (<dp> = 1.6, 2.9, and 3.7 nm). As the data illustrates, low pressure CO IRAS measurements ($P < 5 \times 10^{-6}$ Torr) exhibit CO vibrational features consistent with linear and bridging bound CO on Rh particles, as have been observed on previous CO IRAS studies on planar[10,223,224] and bulk[85,277] supported Rh surfaces. As P_{CO} is increased at or above $P = 5 \times 10^{-6}$ Torr CO, two additional features (~2100 cm^{-1} and ~2040 cm^{-1}) become apparent. These features, which do not exhibit the dipole - dipole coupling shifts with CO pressure known to occur for linear bound CO, are consistent with

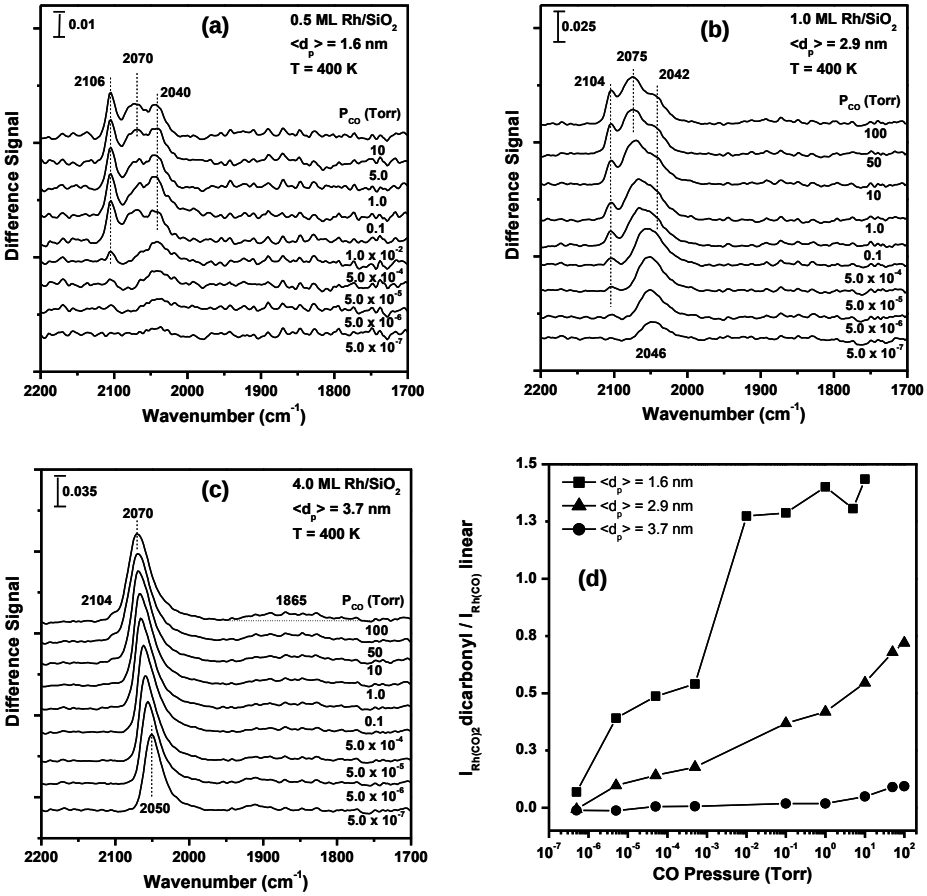

Figure 53. CO PM-IRAS on various Rh particle sizes deposited on SiO_2. (a)-(c): CO PM-IRAS measurements obtained on Rh/SiO_2 surfaces as a function of average Rh particle size ($<d_p>$ = 1.6, 2.9, and 3.7 nm) from low to elevated CO pressures. Spectra obtained sequentially from low to high CO pressure. Scale bar denotes relative scale between figures. (d) : Ratio of the $Rh(CO)_2$ ν_{CO} stretching intensity to the linear bound ν_{CO} stretching intensity ($I_{Rh(CO)_{2,sym}}/I_{Rh(CO)_{linear}}$) as a function of pressure (Torr) from the data of (a)-(c).[236]

Rh gem-dicarbonyl υCO features ($Rh(CO)_2$, asymmetric, 2020 - 2035 cm^{-1}, and symmetric, ~2090 - 2100 cm^{-1} stretching modes), which have been observed on supported Rh catalysts.[31,32,83-87, 220,238] Appearance of these IR stretching modes indicate disruption and dispersion of the as-prepared Rh particles by elevated pressures of CO. Shifts in υ_{CO} of the linearly bound CO species with increasing P_{CO} (e.g. linear υ_{CO} from 2046 cm^{-1} to 2075 cm^{-1} in **Figure 53**(b)) are consistent with well-known dipole coupling effects. **Figure 53**(d) is a qualitative plot to help visualize the particle size effect of Rh dispersion under elevated CO pressures. This graph plots the intensity of the Ilinear/Idicarbonyl, (symmetric) ratio vs. pressure for initial Rh particle sizes. Clearly, a much lower disruptive effect is observed for larger particles (dp > 4 nm) under the pure CO conditions probed in **Figure 53**. This observation is qualitatively consistent with previous studies of supported Rh particles on $TiO_2(110)$[33,225] and infrared studies of Rh/Al_2O_3 supported catalysts.[84,86]

Temperature dependent CO PM-IRAS data were also obtained under P_{CO} = 1 Torr pressure for the same Rh particle sizes ($<d_p>$ = 1.6 nm, 2.9 nm, and 3.7 nm). As the data of **Figure 54** illustrate, increasing temperature results in a decrease in $Rh(CO)_2$ υ_{CO} features for Rh particles. This observation is consistent with previous studies of supported Rh surfaces under CO environments, which show agglomeration of $Rh(CO)_2$ under increasing temperatures.[84,85,239] Additionally, this observation is consistent with IRAS studies of Rh NPs supported on planar oxide supports, which demonstrate that at temperatures above T ~ 300 K, Rh atoms can have sufficient mobility to allow dispersed species to agglomerate to form larger Rh particles.[223-225] Smaller particles appear to

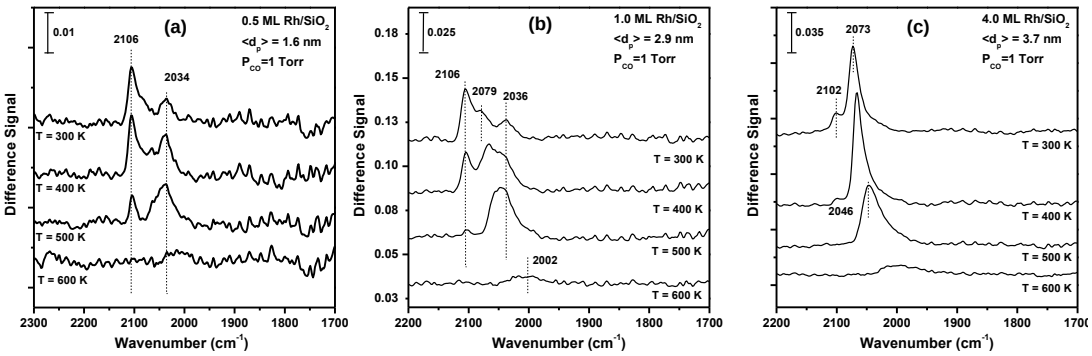

Figure 54. Temperature dependent CO-PM-IRAS on Rh/SiO_2. Shown in (a)-(c) are temperature dependent spectra obtained at P=1 Torr CO for Rh/SiO_2 surfaces (1.6, 2.9 and 3.7 nm). Each spectra obtained with 692 scans. Scale bar denotes relative scale between figures. P_{CO} = 1 Torr is introduced to the chamber at 300 K. Spectra are obtained, then the sample temperature is increased and held to take an infrared spectra in sequential order.[236]

maintain dispersed dicarbonyl features at higher temperatures. However, for every temperature (T = 300 K to 600 K) probed, the particle size which shows the clearest resistance to dispersion is $<d_p>$ larger than 4 nm, under the P_{CO} = 1 Torr conditions probed.

PM-IRAS Measurements Under $C_2H_4/CO/H_2$ Reaction Conditions

PM-IRAS measurements under reaction conditions (T = 500 K) were obtained as a function of Rh particle size (1.6, 2.9, and 3.7 nm Rh/SiO_2) and are shown in **Figure 55**. After rapid spectra (20 scans) at T = 300 K and T = 500 K, PM-IRAS measurements were continuously obtained under standard reaction conditions (identical to **Figure 52**) every 10 minutes. For the $<d_p>$ = 2.9 and 3.7 nm surfaces, under reaction conditions only a single prominent υ_{CO} IRAS feature is observed, one which is consistent with linearly bound CO on Rh. In contrast, IR spectra under reaction conditions on the 1.6 nm surface (particles associated with the decrease in propionaldehyde formation) exhibit *two* prominent υ_{CO} frequencies; one associated with linearly bound CO (2066 cm^{-1}) and a feature consistent (υCO = 2035 cm^{-1}) with a Rh carbonyl hydride species (Rh(CO)H) (υCO = 2020 - 2040 cm^{-1}).[32,87-90,238,240] This species has been observed under CO/H_2[32] and CO_2/H_2[88,90] reaction conditions on dispersed Rh technical catalyst surfaces. Additional PM-IRAS experiments (not shown) were conducted on 1.6 nm Rh/SiO_2 surfaces under CO (50 Torr) and CO/H_2 (50 Torr/400 Torr) environments. These spectra demonstrate the Rh(CO)H (υCO = 2035 cm^{-1}) feature is present and stable under CO/H_2 as well. PM-IRAS measurements obtained under pure CO conditions exhibit the linear and dicarbonyl species displayed in **Figure 53**. Efforts to identify IR signals

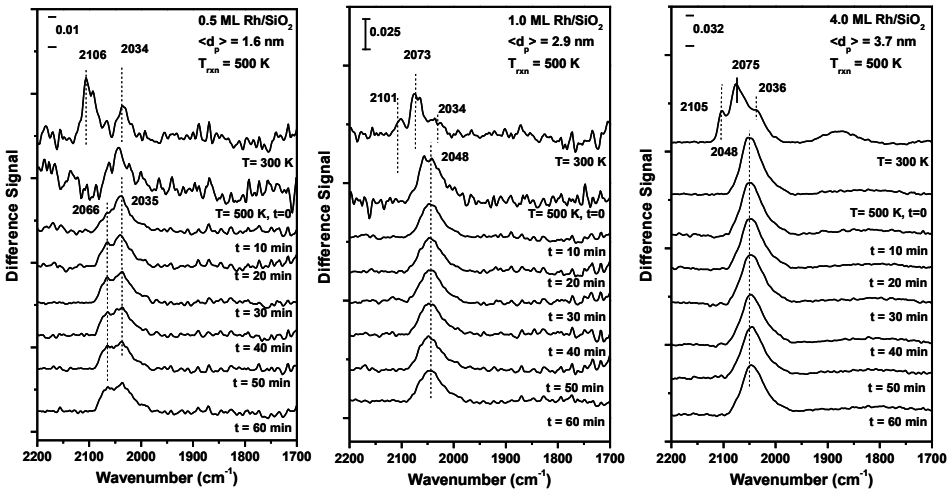

Figure 55. CO-PM-IRAS on Rh/SiO_2 under ethylene hydroformylation reaction conditions. Shown in (a)-(c) are a series of CO PM-IRAS measurements made on various Rh/SiO_2 surfaces under reaction conditions (50 Torr CO, 50 Torr C_2H_4, 400 Torr H_2). For each Rh particle size sample, reactant mixtures are introduced at T = 300 K and rapid IR scan (20 scans) is obtained at T = 300 K. Sample is then heated to T = 500 K and another rapid IR spectra is obtained (20 scans). Sample is then held at reaction temperature and PM-IRAS spectra (692 scans) are obtained every 10 minutes.[236]

associated with surface ethylene adsorbed species (e.g. ethylidene, ethylidyne) under reaction mixture conditions on the Rh/SiO_2 surfaces were unsuccessful. We suspect this is likely due to a combination of sensitivity issues and the low concentration of ethylene derived adsorbates on low Rh coverages.[51] Finally, background measurements on pure SiO_2 surfaces under reaction conditions ($C_2H_4/CO/H_2$) from T = 300 - 600 K exhibited no vibrational features.

To further understand the nature of Rh carbonyl species under reaction conditions (Rh(CO)H), we conducted additional experiments at a lower temperature (T = 400 K) under reaction conditions. Shown in **Figure 56** are PM-IRAS spectra taken in an identical procedure as **Figure 55**. As the data indicate, under T = 400 K conditions, $Rh(CO)_2$ dicarbonyl features are observed under reaction conditions for nearly an hour, though these features appear to slowly decrease, as evidence by the decrease in intensity of the $Rh(CO)_2$ symmetric stretching feature (υCO = 2105 cm^{-1}). If the reaction is allowed to continue for an additional hour (60 - 120 minutes), the spectra begin to resemble that observed at T = 500 K, a prominent linear bound CO feature and a Rh(CO)H hydride feature. A similar experiment conducted on a larger particle surface (2.9 nm) exhibited features associated with linear bound CO. The primary observations from the PM-IRAS studies indicate (1) correlation between particle size and Rh particle dispersion under pure CO conditions (d_p ~ 4 nm) and (2) correlation between the prominent appearance of Rh carbonyl hydride features (Rh(CO)H, υCO = 2035 cm^{-1}) and the decrease in propionaldehyde activity under reaction conditions as particle size is decreased below 2.5 nm.

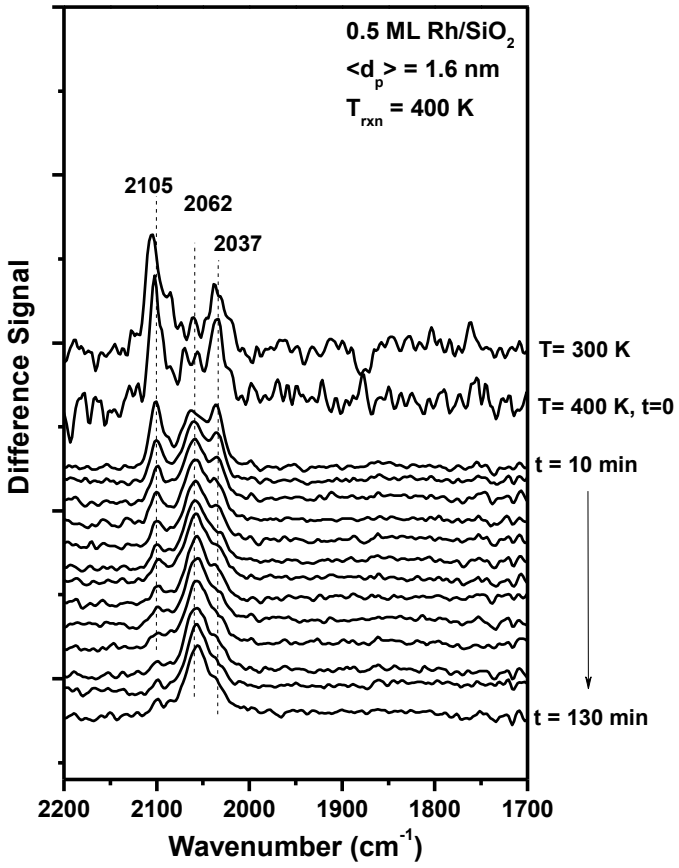

Figure 56. PM-IRAS on a 1.6 nm Rh/SiO_2 at T=400K. Shown in (a)-(c) are a series of CO PM-IRAS measurements made on various Rh/SiO_2 surfaces under reaction conditions (50 Torr CO, 50 Torr C_2H_4, 400 Torr H_2).[236] For each Rh particle size sample, reactant mixtures are introduced at T = 300 K and rapid IR scan (20 scans) is obtained at T = 300 K. Sample is then heated to T = 400 K and another rapid IR spectra is obtained (20 scans). Sample is then held at reaction temperature and PM-IRAS spectra (692 scans) are obtained every 10 minutes.

We begin with a discussion of the reactivity data of **Figure 52**, which demonstrate that the $C_2H_4/CO/H_2$ reaction is structure sensitive with respect to propionaldehyde (CO insertion) activity, exhibiting a maximum TOF near an average Rh particle size of ~ 2.5 nm. Thus, there appear to exist two regimes of particle activity (d < 2.5 nm and d > 2.5 nm), which will be discussed separately.

First, we begin by discussing the propionaldehyde activity of the samples as the particle size is decreased from the planar Rh(111) single crystal surface to the $<d_p>$ = 2.5 nm peak TOF. Upon comparison of the Rh(111) propionaldehyde TOF to the largest particle Rh/SiO_2 TOF ($<d_p>$ = 7.1 nm), we observe a nearly order of magnitude increase in propionaldehyde formation. It is also worthwhile to note that the propionaldehyde TOF observed on the Rh(111) surface (~5.4 x 10^{-3}) is similar in magnitude to a propionaldehyde TOF measurement (~1 x 10^{-2}) conducted over a Rh foil by Somorjai and co-workers[241,242], under similar reaction conditions. Two factors could contribute to the increased TOF: (1) increase in undercoordinated (non-terrace) Rh atoms on dispersed Rh/SiO2 surfaces going from the close-packed, planar Rh(111) surface to the 8 ML (7.1 nm) film and (2) presence of the SiO2 support. Intuitively (and as evidenced by the data of **Figure 51**), an increase in undercoordinated surface atoms occurs going from the close-packed, planar Rh(111) surface to the 8 ML (7.1 nm) film. However, the small increase in this concentration expected on such surfaces (~10% going from a Rh(111) surface to a 7.1 nm Rh/SiO_2 surface) seems small to completely account for the nearly order of magnitude difference in CO insertion reactivity. Indeed, in the case of C_4H_{10} hydrogenolysis, C_2H_6 product mol fraction (which is strongly dependent on

undercoordinated Rh atom sites) is essentially identical for the 7.1 nm (0.33) and Rh(111) surface (0.31) (**Figure 51**). Additionally, Rh/SiO_2 characterization measurements[12] demonstrate that the Rh site density on these two surfaces 7.1 nm (1.3 x 10^{15} sites/cm^2) and Rh(111) (1.6 x 10^{15} sites/cm^2), are essentially the same as well. Combined, these pieces of evidence suggest that the SiO_2 support plays an important role in the CO insertion reaction to form propionaldehyde. This idea is consistent with observations of previous studies[77] which indicate hydrogen present on the SiO_2 support may play a role in hydrogenating C_3H_5O acyl groups present on the Rh particle. It is noted that this step (acyl hydrogenation) has been thought to be the rate limiting step in propionaldehyde formation, under certain reaction conditions.[76]

As the Rh particle size is decreased from $<d_p>$ = 7.1 nm to 2.5 nm, a roughly ~5 fold increase in propionaldehyde production (CO insertion activity) is observed. This observation is consistent with the increase in undercoordinated (non-terrace) Rh surface sites expected (**Figure 51**) from this particle size decrease, which interestingly also exhibit a 5-fold increase in fraction of undercoordinated Rh surfaces sites over this size range. We consider this to be strong evidence that propionaldehyde formation occurs more favorably on undercoordinated (non-terrace) Rh^0 sites on Rh particles over the $<d_p>$ = 7.1 nm to $<d_p>$ = 2.5 nm size range. This observation is consistent with and corroborated by previous technical catalyst studies of C_2H_4 hydroformylation on cluster derived Rh supported catalysts, which show a similar relationship between dispersion and propionaldehyde TOF.[80,81]

However, in the second regime of reactivity (as particle size is decreased below <dp> = 2.5 nm), a decrease in propionaldehyde formation (CO insertion) is observed. PM-IRAS measurements in pure CO and under reaction conditions help provide information correlating CO insertion activity and CO surface species, as a function of Rh particle size. CO PM-IRAS measurements (**Figure 53**) show that oxidative disruption and dispersion of Rh particles to form highly dispersed $Rh(CO)_2$ can occur under increasing pure CO pressures. When experiments are conducted as a function of Rh particle size, it becomes readily apparent that in pure CO conditions, particles > 4 nm appear to exhibit a resistance to such oxidative dispersion, whereas particles below this size are dispersed more readily (**Figure 53**). Similar qualitative behavior has been observed on supported catalyst[83,84,86] and surface science studies[33,225] of supported Rh particles, which have demonstrated that larger catalyst loadings (likely associated with larger particles sizes) exhibit resistance to dispersion. Thus, the nature of Rh particle dispersion and CO surface adsorbates under elevated pressures, depend on both initial Rh particle size and CO pressure at a given temperature.

Under $C_2H_4/CO/H_2$ reaction conditions (**Figure 55**, T = 500 K) a similar trend is observed. For initial Rh particle sizes above 2.9 nm, PM-IRAS spectra exhibit a single, prominent CO infrared feature associated with linearly bound CO. However, for particles below < 2.9 nm, *two* prominent CO IR stretching frequencies are observed consistent with both linearly bound CO (2066 cm^{-1}) and Rh(CO)H carbonyl hydride species (~2035 cm^{-1}) (**Figure 55**). The key result of the PM-IRAS experiments is that the peak propionaldehyde reactivity is demarcated by differences in CO adsorbates

observed in the PM-IRAS spectra; below d_p ~ 2.9 nm, prominent features associated with Rh(CO)H and linear bound CO are observed. Above 2.9 nm, only a single, pronounced linear bound CO feature is observed. This shows that changes in Rh particle dispersion and/or changes in CO binding can occur for small Rh particles under reaction conditions at near atmospheric pressures. These data also indicate that surfaces characterized by the presence of Rh carbonyl hydride species appear to be less active for propionaldehyde formation than surfaces containing predominantly linear bound CO on contiguous Rh sites. This observation is consistent with findings on technical catalyst surfaces for C_2H_4 hydroformylation, which has suggested that CO bound to different Rh surface sites show different reactivities for CO insertion. In particular, transient transmission infrared spectroscopy by Chuang and co-workers has demonstrated that linear bound Rh is more reactive than CO bound to dispersed, dicarbonyl bound CO ($Rh(CO)_2$) or bridge bound CO.[77,78]

Taken together, the kinetic and spectroscopic data suggest that the observed particle size effect of CO insertion for ethylene hydroformylation on Rh/SiO_2 surfaces is driven by two factors: (1) promotion of CO insertion on undercoordinated (non-terrace) Rh surface sites as initial average Rh particle size is decreased to ~ 2.5 nm (2) decrease in propionaldehyde formation on small Rh particles, which correlates with the presence and formation of Rh carbonyl hydride species under reaction conditions as observed via PM-IRAS. Comparison with Rh(111) reactivity data suggests the SiO_2 support may play a role in the propionaldehyde formation on Rh/SiO_2.

One could speculate that CO bound to Rh(CO)H species could be less active for CO insertion for a number of reasons. First, electronic effects could play a role in affecting the insertion reactivity of CO bound to supported Rh(CO)H species. Rh inorganic complexes ($Rh(CO)HL_3$; L= ligand), with tailored ligand constituents, is the catalyst phase utilized in the homogenous catalytic process employed in industry for olefin hydroformylation.[75] As it is well known that ligand size and electronic character are critically important variables in determining product selectivity and activity in the homogenous process, it may be that supported Rh(CO)H species also require such ligands to activate the CO bound carbonyl species for CO insertion.

Second, if Rh(CO)H species are highly dispersed like $Rh(CO)_2$ species, geometric constraints could potentially inhibit CO insertion on supported Rh(CO)H species, due to Rh atom ensembles which may be required for such a multi-adsorbate reaction. However, some additional questions remain regarding the dispersity of the Rh/SiO_2 surfaces which produce Rh(CO)H. From previous studies of Rh particles under CO ambients with a multitude of analytical techniques (e.g, EXAFS[30], IR[83]), it is generally agreed that $Rh(CO)_2$ species are likely associated with highly dispersed Rh species (perhaps small clusters containing ~10's of Rh atoms[30]) present on the oxide support. However, the data regarding the dispersity of Rh(CO)H species remains less clear. STM studies of Rh/TiO_2 surfaces have demonstrated little Rh dispersion under pure H_2 environments[33], and interpretations of IR studies have suggested H_2 hinders oxidative disruption of Rh particles[32] or contributes to agglomeration of $Rh(CO)_2$ species to form larger Rh clusters at higher temperatures.[31] However, there certainly appears to

be a relationship between $Rh(CO)_2$ and Rh(CO)H, based on the PM-IRAS data under reaction conditions. First, $Rh(CO)_2$ features present under reaction conditions at T = 400 K (**Figure 56**) eventually exhibit features consistent with Rh(CO)H at long reaction times. Secondly, Rh particle dispersion under pure CO conditions (**Figure 53**) and the presence of the CO insertion reactivity maximum also occur around the same particle size (~2.5 - 3.5nm). The relation between $Rh(CO)_2$ and Rh(CO)H interconversion has also been explored in a previous surface science study of Rh/TiO_2 surfaces by Hayden et. al.[243] This study suggested that, under UHV conditions, $Rh(CO)_2$ and Rh(CO)H can interchange under CO and H_2 ambients, respectively. Additional IR studies of supported Rh catalysts have also shown a gradual transition from dicarbonyl IR features to carbonyl hydride features under CO/H_2 environments.[89] However, other investigators[31] have argued this is simply a transition from $Rh(CO)_2$ species to linearly bound CO on agglomerated Rh particles. As mentioned earlier, C_2H_6 formation (competing reaction pathway) under our reaction conditions also exhibited a sharp transition near the 2.5 nm particle size, showing a maximum C_2H_6 TOF between <dp> = 1.5 - 2.5 nm. Based on the known structure insensitive behavior of ethylene hydrogenation on Pt group metals[61], this observation is certainly consistent with an increased dispersion (increased number of active sites) associated with the optimum data point. Though it cannot be ruled out that this is simply an inherent change in activity of Rh(CO)H species for C_2H_4 hydrogenation. Thus, while the reactivity and spectroscopic data provide evidence suggesting that CO bound to Rh(CO)H is less active for the CO insertion reaction, the question of the dispersity of the Rh(CO)H surface under our reaction conditions, and

how it compares to the related $Rh(CO)_2$ dispersity remains open. Future measurements, which could measure particle size (e.g. HP-STM) or Rh-Rh coordination (e.g. EXAFS) under relevant $C_2H_4/CO/H_2$ reaction conditions employed in this study, would be helpful to answering such questions.

Summary

The structure activity behavior of the $C_2H_4/CO/H_2$ reaction was studied as a function of Rh particle size on Rh/SiO_2 model catalyst surfaces, with particular interest on the CO insertion reaction pathway. Kinetic measurements and PM-IRAS spectroscopic techniques were utilized under near atmospheric reaction conditions. Our primary conclusions are as follows:

Propionaldehyde (CO insertion) activity under reaction conditions (T = 500 K) showed an optimum Rh particle size of <dp> ~ 2.5 nm. Reactivity of Rh/SiO_2 surfaces to Rh(111) surfaces showed roughly an order of magnitude increase in TOF (**Figure 52**).

PM-IRAS measurements under pure CO conditions showed particle disruption and dispersion from low (5×10^{-7} Torr) to near atmospheric CO pressures, as evidenced by $Rh(CO)_2$ vibrational features (**Figure 53**). Oxidative disruption also exhibited a particle size dependence; particles above $<d_p> \sim 4$ nm appeared resistant to CO induced dispersion at elevated pressures; particles below 4 nm appeared more susceptible to this effect.

PM-IRAS under reaction conditions exhibited a particle size dependence in the types of ν_{CO} features observed on the surface (**Figure 55**). Rh particle sizes above (> 2.5 nm) the optimum propionaldehyde TOF exhibited only a single ν_{CO} associated with

linearly bound CO. Particle sizes below the optimal TOF (< 2.5 nm) exhibited ν_{CO} associated with both linearly bound CO and Rh carbonyl hydride CO. PM-IRAS on 1.6 nm particles under reaction conditions at lower temperatures (T = 400 K) exhibited linear and $Rh(CO)_2$ species; PM-IRAS obtained under extended reaction times at T= 400 K eventually produced spectra similar to Rh(CO)H, suggesting a relationship between $Rh(CO)_2$ and Rh(CO)H (**Figure 56**).

Combined, the kinetic and spectroscopic data suggest that the observed particle size effect of CO insertion for ethylene hydroformylation is driven by 2 factors: (1) promotion of CO insertion on undercoordinated Rh surface sites and (2) decrease in propionaldehyde formation on small Rh particles, which based on PM-IRAS measurements under reaction conditions, may be due to the formation of Rh carbonyl hydride species.

CHAPTER V

CONCLUSIONS

An investigation of oxide supported Pt and Rh nanoparticle model catalysts was conducted under both ultra high vacuum and elevated pressure conditions using an array of characterization techniques (e.g. TDS, IRAS). Pt(110) and Rh(111) single crystals were also evaluated in the same apparatus under identical conditions as the nanoparticles. The study was conducted for two reasons (i) to test the efficacy of utilizing a reaction rate as a quantitative probe of surface active sites (ii) to study structure activity relationships of heterogeneous model catalysts.

Nanoparticle samples were prepared in an UHV surface analysis chamber by the vapor deposition method. The UHV chamber allowed the creation ultra clean nanoparticles (i.e. nanoparticles in absence of residual contamination from processes such as solution deposition of inorganic metallic complexes). This permitted very accurate vibrational spectra of chemisorbed species to be obtained as surfaces are purely metallic. This is demonstrated in the CO-IRAS and CO-TDS measurements conducted on Pt/SiO_2 and Rh/SiO_2. Microscopy measurements from STM and ex-situ TEM were used to establish particle sizes and CO chemisorption was performed to obtain surface area measurements under low pressure conditions. Microscopy measurements reveal particle sizes between 1 - 6nm for Pt and Rh coverages between 1 - 6ML and exhibit a relatively narrow size distribution (0.5 - 1nm) for particles <3nm. CO chemisorption on the Pt particles revealed terrace ($\geq C_8$) and step sites ($\leq C_7$) in the desorption profile and

allowed the concentrations of each to be established on Pt nanoparticles as a function of size. Results demonstrate the most drastic change in undercoordinated atoms occurs between 1 - 4nm consistent with hard sphere model calculations. Since the excellent agreement of CO chemisorption with hard sphere models this type of analysis is universal for purely metallic FCC particles which grow spherical on a silica substrate. Such analysis can be extended to Rh/SiO_2 where the terrace and step sites could not be established in the CO desorption profile because CO interacts similarly on both sites. High pressure experiments further support this as demonstrated during high pressure structure sensitive reactions on Rh nanoparticles (during hydrogenolysis and ethylene hydroformylation) where the reaction rate increases similarly with the concentration of undercoordinated atoms.

Both single crystals and oxide supported particles were subjected to high pressure gases to conduct CO oxidation, n-heptane dehydrocyclization, and ethylene hydroformylation reactions. This was performed in-situ after surface preparation in vacuum by translating samples through a differentially pumped sliding seal coupled to a high pressure reaction cell. CO oxidation on Pt and Rh has proven to be structure insensitive under CO dominant conditions as the activation energies for all particles sizes tested held identical activation energies to single crystal samples within experimental error. Similar activation energies to technical catalysts were also observed. This has been the first comprehensive study on structure insensitive behavior of this reaction on nanoparticle model catalysts. The reaction rate from CO oxidation on Pt and Rh nanoparticles was further used to determine the concentration of active sites. These

results were obtained by normalizing the data to well-defined single crystals with a known surface atom density (i.e. Pt(110) and Rh(111)). Since surface area characterization under low pressure conditions (e.g. UHV) can be much different then that obtained under high pressure, the unique structure insensitivity of the CO oxidation allows a quantitative estimate of surface active sites under high pressure conditions. This surface area estimate was then used for obtaining a turn over frequency (TOF) for a reaction whose site concentration under elevated pressure conditions is unknown. For example, turn over frequencies (molecules/site/s) for both n-heptane dehydrocyclization to toluene and ethylene hydroformylation to propanal have been determined in this manner. The dehydrocyclization reaction is an interesting reaction because competing side reactions occur on the same reactions sites (e.g hydrogenolysis). The structure sensitivity (dehydrocyclization) was then extended to extract the concentration of undercoordinated atoms under high pressure reaction conditions. Results have demonstrated the reaction rate to scale similarly with the concentration of sites with $\leq C_7$ coordination. This indicates undercoordinated atoms are participating favorably in the reaction mechanism. For hydroformylation, the reaction was utilized to study the CO insertion into an ethyl intermediate. Interestingly, small Rh particles are further dispersed by CO. This phenomenon adversely affects the formation rate of propanal. PM-IRAS under reaction conditions showed evidence of a carbonyl hydride species under these conditions. This species is associated with the sudden decrease in reactivity when the particle size is changed <2nm. The SiO_2 substrate is also shown to have a

positive effect on both structure sensitive reactions as observed in the differences in rate measurements between large particles (>3nm) and single crystals.

The tandem use of single crystal &oxide supported clusters, structure sensitive & insensitive reactions, and high & low pressure characterization permitted structure activity relationships to be established under a range of conditions. This type of analysis avoids complications of using reference values from the extremely diverse conditions presented in the literature. The experiments offer a unique perspective as direct comparison between supported and unsupported Pt or Rh catalysts were conducted in the same apparatus. This allowed investigation of the material gap between supported nanoparticles and single crystals. Analysis also allowed study of high pressure reaction rates as an analytical probe of surface sites. These experiments open the door to future study of more complicated reactions on Pt and Rh model catalysts. For example, studying competitive adsorption processes by adding a second hydrocarbon to the n-heptane dehydrocyclization reaction at varying concentrations or similarly adding alkenes to the ethylene hydroformylation reactions. The controlled experiments will allow insight into reactions pathways by monitoring product selectivity. The model catalysts also provide a basis for studying more complicated materials such as alloying of Rh or Pt with a second metal. Overall, the results demonstrate the utility of model catalyst systems for studying structure activity relationships in heterogeneous catalysis and the efficacy of using the rate of a chemical reaction to obtain active site concentrations.

REFERENCES

1. Atkins, P. *Physical Chemistry*; W. H. Freeman: New York, 1998.
2. Somorjai, G. *Introduction to Surface Chemistry and Catalysis*; John Wiley & Sons, Inc.: Hoboken, NJ, 2010.
3. Kolasinski, K. *Surface Science*: *Foundations of Catalysis and Nanoscience*; John Wiley & Sons, Ltd.: West Sussex, England, 2008.
4. St. Clair, T.P.; Goodman, D.W. *Topics in Catal.* **2000**, 13, 5.
5. Goodman, D.W. *Chem. Rev.* **1995**, 9, 523.
6. Hoffman, F.M. *Surf. Sci. Rep.* **1983**, 3, 107.
7. Blackman, G.S.; Kao, C.T.; Bent, B.E.; Mate, C.M.; Van Hove, M.A.; Somorjai, G.A. *Surf. Sci.* **1988**, 207, 66.
8. Valden, M.; Lai, X.; Goodman, D.W. *Science* **1998**, 281, 1647.
9. Goodman, D.W. *J. Phys. Chem.* **1996**, 100, 13090.
10. McClure, S.M.; Lundwall, M.; Yang, F.; Zhou, Z.; Goodman, D.W. *J. Phys.: Cond. Matt.* **2009**, 21, 474223.
11. McClure, S.M.; Lundwall, M.; Zhou, Z.; Yang, F.; Goodman, D.W. *Catal. Lett*. **2009**, 133, 298.
12. McClure, S.M.; Lundwall, M.; Yang, F.; Zhou, Z.; Goodman, D.W. *J. Phys. Chem. C*. **2009**, 113, 9688.
13. Haq, S.; Raval, R. *Phys. Chem. Chem. Phys.* **2007**, 9, 3641.
14. Freund, H.J. *Topics in Catal.* **2008**, 48, 137.
15. Henry, C.R. *Surf. Sci. Rep.* **1998**, 31, 231.

16. Altman, E.I.; Gorte, R.J. *Surf. Sci.* **1986**, 172, 71.

17. Hensley, D.A.; Kesmodel, L.L. *J. Phys. Chem.* **1991**, 95, 1363.

18. Rainer, D.R.; Xu, C.; Holmblad, P.M.; Goodman, D.W. *J. Vac. Sci. Technol. A.* **1997**, 15, 1653.

19. Rainer, D.R.; Goodman, D.W. *J. Mol. Cat. A: Chem* **1998**, 131, 259.

20. Park, J.Y.; Aliaga, C.; Renzas, J. R.; Lee, H.; Somorjai, G.A. *Catal. Lett.* **2009**, 129, 1.

21. Grass, M.E.; Zhang, Y.; Butcher, D. R.; Park, J. Y.; Li, Y.; Bluhm, H.; Bratlie, K. M.; Zhang, T.; Somorjai, G. A. *Angew. Chem. Int. Ed.* **2008**, 47, 8893.

22. Baumer, M.; Freund, H.-J. *Prog. Surf. Sci.* **1999**, 61, 127.

23. Goodman, D.W. *J. Catal.* **2003**, 216, 213.

24. Rupprechter, G. *Catal. Today*. **2007**, 126, 3.

25. Poppa, H. *Catal. Rev.* **1993**, 35, 359.

26. Zafiris, G. S.; Gorte, R. J. *J. Catal.* **1993**, 140, 418.

27. Altman, E. I.; Gorte, R. J. *J. Catal.* **1988**, 110, 191.

28. Meusel, I.; Hoffmann, J.; Hartmann, J.; Libuda, J.; Freund, H. J. *J. Phys. Chem. B.* **2001**, 105, 3567.

29. Hayek, K.; Goller, H.; Penner, S.; Rupprechter, G.; Zimmermann, C. *Catal. Lett.* **2004**, 92, 1.

30. Van't Blik H. F. J.; Van Zon J.B.A.D.; Huizinga T.; Vis J. C.; Koningsberger D. C.; Prins R. *J. Phys. Chem.* **1983**, 87, 2264.

31. Basu, P.; Panatyotov, D.; Yates Jr., J.T. *J. Am. Chem. Soc.* **1988,** 110, 2074.

32. Solymosi, F.; Pásztor, M. *J. Phys. Chem.* **1986**, 90, 5312.

33. Berkó, A.; Solymosi, F. *J. Catal*. **1999**,183, 91.

34. Yang, W.S.; Jona, F. P.; Marcus, M. *Phys. Rev. B.* **1983**, 28, 2049.

35. Xu, X.; Goodman, D.W. *Catal. Lett.* **1994**, 24, 31.

36. Vattuone, L.; Savio, L.; Rocca, M. *Surf. Sci. Rep.* **2008**, 63, 101.

37. Gale, R. J.; Salmeron, M.; Somorjai, G.A. *Phys. Rev. Lett.* **1997**, 38, 1027.

38. Winkler, A.; Guo, X.; Siddiqui, H.R.; Hagans, P.L.; Yates, J.T. *Surf. Sci.* **1988**, 201, 419.

39. Savio, L.; Vattuone, L.; Rocca, M. *Phys. Rev. Lett.* **2001**, 87, 276101.

40. Vattuone, L.; Savio, L.; Rocca, M. *Phys. Rev. Lett.* **2003**, 90, 228302.

41. Knight, P.J.; Driver, S.M.; Woodruff, D.P. *Chem. Phys. Lett.* **1996**, 259, 503.

42. Karmazyn, A. D.; Fiorin, V.; King, D.A. *Surf. Sci.* **2003**, 547, 184.

43. Hirsimaki, M.; Suhonen, S.; Pere, J.; Valden, M.; Pessa, M. *Surf. Sci*. **1998**, 404, 187.

44. Kim, Y.K.; Morga, G.A. Jr.; Yates Jr., J.T. *Surf. Sci.* **2005**, 598, 14.

45. Gee, A. T.; Hayden, B.E.; Mormiche, C.; Kleyn, A.; Reidmuller, B. *J. Chem. Phys.* **2003**, 118, 3334.

46. Venables, J.A. *Surf. Sci.* **1994**, 299, 798.

47. Chambers, A. *Modern Vacuum Physics*; CRC Press LLC: Boca Raton, FL, 2005.

48. Usher, B.F. *App. Sur. Sci.* **1985**, 22, 506.

49. Van Hardeveld, R.; Hartog, F. *Surf. Sci.* **1969**, 15, 189.

50. Van Hove, M.A.; Somorjai, G.A. *Surf. Sci.* **1980**, 92, 489.

51. Xu, J.; Yates, J.T. *Surf. Sci.* **1995**, 327, 193.

52. Kose, R.; King, D.A. *Chem. Phys. Lett.* **1999**, 313, 1.

53. Lundwall, M.; McClure, S.M.; Goodman, D.W. *J. Phys. Chem. C.* **2010**, 114 7904.

54. Rioux, R.M.; Hsu, B.B.; Grass, M.E.; Song, H.; Somorjai, G.A. *Catal. Lett.* **2008**, 126, 10.

55. Cleveland, C.L.; Landman, U. *J. Chem. Phys.* **1991**, 94, 7376.

56. Chen, M.S.; Goodman, D.W. *J. Phys. Condes. Matt*. **2008**, 20, 264013.

57. Davis, S.M.; Zaera, F.; Somorjai, G.A. *J. Catal.* **1984**, 85, 206.

58. Davis, S.M.; Zaera, F.; Somorjai, G. A. *J. Catal.* **1982**, 77, 439.

59. Gillespie, W.D.; Herz, R.K.; Peterson, E.E.; Somorjai, G.A. *J. Catal.* **1981**, 70, 147.

60. Gao, F.; McClure, S.M.; Cai, Y.; Gath, K.K.; Wang, Y.; Chen, M.S.; Guo, Q.L.; Goodman, D.W. *Surf. Sci.* **2009**, 603, 65.

61. Zaera, F.; Somorjai, G.A. *J. Am. Chem. Soc.* **1984**, 106, 2288.

62. Gao, F.; Wang, Y.; Cai, Y.; *J. Phys. Chem. C.* **2009**, 113, 174.

63. Chen, P.; Kung, K.Y.; Shen, Y.R.; Somorjai, G.A. *Surf. Sci.* **2001**, 494, 289.

64. Davis, S.M.; Somorjai, G.A. *J. Catalysis* **1980**, 65, 78.

65. McCrea, K.R.; Somorjai, G.A. *J. Mol. Catal. A. Chem.* **2000**, 163, 43.

66. Goodman, D.W.; Peden, C.H.F. *J. Phys. Chem.* **1986**, 90, 4839.

67. Peden, C.H.F.; Goodman, D.W.; Blair, D.S.; Berlowitz, P.J.; Fisher, G. B.; Oh, S. H. *J. Phys. Chem.* **1988**, 92, 1563.

68. Oh, S. H.; Fisher, G. B.; Carpenter, J. E.; Goodman, D. W. *J. Catal.* **1986**, 100, 360.

69. Kiss, J. T.; Gonzalez, R.D. *J. Phys. Chem.* **1984**, 88, 898.

70. Cant, N.W.; Hicks, P.C.; Lennon, B.S. *J. Catal.* **1978**, 54, 372.

71. Oh, S. H.; Eickel, C. C. *J. Catal.* **1991**, 128, 526.

72. Hendriksen, B.L.M.; Frenken, J.W.M. *Phys. Rev. Lett.* **2002**, 89, 046101.

73. Mars, P.; Krevelen, DW.v. *Chem. Eng. Sci. Special Suppl.* **1954**, 3, 41.

74. Blakely, D.W.; Somorjai, G.A. *J. Catalysis* **1976**, 42, 181.

75. Kamer, P.C.J.; Reek, J.N.H.; Van Leeuwen, Piet W.N.M. *Rh Catalyzed Hydroformylation*; Van Leeuwen, Piet W.N.M., Claver, C., Eds.; Kluwer Academic Publishers: New York, 2002; 35.

76. Balakos, M. W.; Chuang, S.S.C. *J. Catal.* **1995**, 151, 253.

77. Chuang, S.S.C.; Stevens, Jr.; R.W.; Khatri, R. *Topics in Catal.* **2005**, 32, 225.

78. Chuang, S.S.C.; Pien, S.I. *J. Catal.* **1992**, 135, 618.

79. Chuang, S.S.C.; Krishnamurthy, R.; Tan, C. D. *Coll. Surf. A. Physicochem. Eng. Asp.* **1995**, 105, 35.

80. Hanaoka, T.; Arakawa, H.; Matsuzaki, T.; Sugi, Y.; Kanno, K.; Abe, Y. *Catal. Today* **2000**, 58, 271.

81. Huang, L.; Xu, Y.; Guo, W.; Liu, A.; Li, D.; Guo, X. *Catal. Lett.* **1995**, 32, 61.

82. Brown, N.F.; Barteau, M.A. *Langmuir* **1992**, 8, 862.

83. Cavanagh, R. R.; Yates Jr., J.T. *J. Chem. Phys.* **1981**, 74, 4150.

84. Solymosi, F.; Bánsági, T *J. Phys. Chem*. **1993**, 97, 10133.

85. McQuire, M.W.; McQuire, G.W.; Rochester, C.H. *J. Chem. Soc., Farad. Trans.* **1992**, 88, 1203.

86. Zaki, M. I.; Kunzmann, G.; Gates, B. C.; Knözinger, H. *J. Phys. Chem.* **1986**, 91,1486.

87. Yang, A. C.; Garland, C. W. *J. Phys. Chem.* **1957**, 61, 1504.

88. Henderson, M.A.; Worley, S. D. *J. Phys. Chem.* **1985**, 89, 1417.

89. Worley, S.D.; Mattson, G.A.; Caudill, R. *J. Phys. Chem.* **1983**, 87, 1671.

90. Solymosi, F.; Erdöhelyi, A.; Bánsági, T. *J. Catal.* **1981**, 68, 371.

91. Hablanian, M.H. *High-Vacuum Technology: A Practical Guide*; Marcel Dekker, Inc.: New York, 1997.

92. Szanyi, J.; Goodman, D. W. *Rev. Sci. Ins.* **1993**, 64, 2350.

93. Thompson, M.; Baker, M.D.; Christie, A.; Tyson, J.F. *Auger Electron Spectroscopy.* John Wiley and Sons, Chemical Analysis Vol. 74 **1985**.

94. Davis, L.E.; MacDonald, N.C.; Palmberg, P.W.; Riach, G.E.; Weber, R.E. *Handbook of Auger Electron Spectroscopy*; Physical Electronics Industries Inc.: Eden Prairie, MN, 1978.

95. Briggs, E. D.; Seah, M.P. *Practical Surface Analysis*; JohnWiley & Sons: New York, 1983.

96. Argile, C.; Rhead, G.E. *Surf. Sci. Rep.* **1989**, 10, 277.

97. Besenbacher, F. *Rep. Prog. Phys.* **1996**, 59, 1737.

98. Hamers, R. J. *Ann. Rev. Phys. Chem.* **1989**, 40, 531.

99. Nazin, G. V.; Wu, S. W.; Ho, W. *Proc. Nat. Acad. Sci.* **2005**,102, 8832.

100. Eigler, D. M.; Weiss, P. S.; Schweizer, E. K.; Lang, N. D. *Phys. Rev. Lett.* **1991**, 66, 1189.

101. Williams, D.B., Carter, C. B. *Transmission Electron Miscoscpy: A Textbook for Materials Science*; Springer: New York, 2004.

102. DeJong, A. M.; Niemantsverdriet, J.W. *Surf. Sci.* **1990**, 23, 355.

103. Redhead, P. A. *Vacuum* **1962**, 12, 203.

104. Mattson Instruments, *Cygnus 100 Infrared Spectrometer Operating Manual*; 1987.

105. Griffiths, P.R.; Haseth, J.A. *Fourier Transform Infrared Spectrometry*; John Wiley & Sons, Inc.: New York, 1986.

106. Blyholder, G. *J. Phys. Chem.* **1964**, 68.

107. Hollins, P. *Surf. Sci. Rep.* **1992**, 16.

108. Chen, M.S.; Santra, A. K.; Goodman, D. W., *Phys. Rev. B.* **2004**, 69, 155404.

109. Schroeder, T.; Giorgi, J.B.; Bäumer, M.; Freund, H.J. *Phys. Rev. B.* **2002**, 66, 165422.

110. Schroeder, T.; Adelt, M.; Richter, B.; Naschitzki, M.; Baumer, M.; Freund, H. J. *Surf. Rev. Lett.* **2000**, 7, 7.

111. Xu, X.; Goodman, D. W. *Appl. Phys. Lett.* **1992**, 61, 774.

112. Wang, H.; Tobin, R.G.; Lambert, D.K. *J. Chem. Phys.* **1994**, 101, 4277.

113. Chen, M. S.; Cai Y.; Yan Z.; Gath, K. K.; Axnanda S.; Goodman, D.W. *Surf. Sci.* **2007**, 601, 5326.

114. Black, F.M.; High, L.E.; Sigsby, J.E. *Water, Air, Soil Poll.* **1975**, 5, 53.

115. Purnell, H. *Gas Chromatography*; John Wiley & Sons, Inc.: New York, 1962.

116. Xu, X.; Vesecky, S.M.; Goodman, D.W. *Science* **1992**, 258, 788.

117. Kalakkad, D.; Anderson, S.L.; Logan, A.D.; Pena, J.; Braunschweig, E.J.; Peden, C.H.F.; Datye, A.K. *J. Phys. Chem.* **1993**, 97, 1437.

118. Coulter, K.; Xu, X.; Goodman, D.W. *J. Phys. Chem.* **1994**, 98, 1245.

119. Somorjai, G.A.; McCrea, K.R.; Zhu, J. *Topics in Catal.* **2002**, 18, 157.

120. Silvestre-Albero, J.; Rupprechter, G.; Freund, H.J. *J. Catal.* **2006**, 240, 58.

121. Kugler, E.L.; Boudart, M. *J. Catal.* **1979**, 59, 201.

122. Wei, T.; Wang, J.; Goodman, D.W. *J. Phys. Chem. C.* **2007**, 111, 8781.

123. Stoop, F.; Toolenaar, F.J.C.M.; Ponec, V. *J. Catal.* **1982**, 73, 50.

124. McClellan, M.R.; Gland, J.L.; McFeeley, F.R. *Surf. Sci.* **1981**, 112, 63.

125. Beebe, T.P.; Yates, J.T. *Surf. Sci.* **1986**, 173, L606.

126. Gross, E.; Asscher, M.; Lundwall, M.; Goodman, D.W. *J. Phys. Chem. C.* **2007**, 111, 16197-16201.

127. Morgan, A.E.; Somorjai, G.A. *Surf. Sci.* **1968**, 12, 405.

128. Morgan, A.E.; Somorjai, G.A. *J. Chem. Phys.* **1969**, 51, 3309.

129. Fair, J.; Madix, R.J. *J. Chem. Phys.* **1980**, 73, 3480.

130. Malik, I.J.; Brubaker, M.E.; Mohsin, S.B.; Trenary, M. *J. Chem. Phys.* **1987**, 87, 5554.

131. Starke, U.; Barbieri, A.; Materer, N.; Van Hove, M.A.; Somorjai, G.A. *Surf. Sci.* **1993**, 286, 1.

132. Cremer, P.S.; Su, X.; Shen, Y.R.; Somorjai, G.A. *J. Am. Chem. Soc.* **1996**, 118, 2942.

133. Stacchiola, D.; Kaltchev, M.; Wu, G.; Tysoe, W.T. *Surf. Sci.* **2000**, 470, L32.

134. Rioux, R.M.; Hoefelmeyer, J.D.; Grass, M.; Song, H.; Niesz, K.; Yang, P.; Somorjai, G.A. *Langmuir* **2008**, 24, 198.

135. Frank, M.; Baumer, M.; Kuhnemuth, R.; Freund, H. J. *J. Vac. Sci. Technol. A.* **2001**, 19, 1497.

136. Ainsworth, M.K.; McCoustra, M.R.S.; Chesters, M.A.; Sheppard, N.; De La Cruz, C. *Surf. Sci.* **1999**, 437, 9.

137. Besocke, K.; Krahl-Urban, B.; Wagner, H. *Surf. Sci.* **1977**, 68, 39.

138. Hammer, B.; Nielsen, O.H.; Norskov, J.K. *Catal. Lett.* **1997**, 46, 31.

139. Gracia, F.J.; Bollmann, L.; Wolf, E.E.; Miller, J.T.; Kropf, A. J. *J. Catal.* **2003**, 220, 382.

140. Hayden, B.E.; Kretzschmar, K.; Bradshaw, A.M.; Greenler, R.G. *Surf. Sci.* **1985**, 149, 394.

141. Luo, J.S.; Tobin, R.G.; Lambert, D.K.; Fisher, G.B.; DiMaggio, C.L. *J. Chem. Phys*. **1993**, 99, 1347.

142. Brandt, R.K.; Greenler, R.G. *Chem. Phys. Lett.* **1994**, 221, 219.

143. Wang, H.; Tobin, R.G.; Lambert, D.K.; Fisher, G.B.; DiMaggio, C.L. *J. Phys. Chem.* **1995**, 103, 2711.

144. Creighan, S.C.; Mukerji, R.J.; Bolina, A.S.; Lewis, D.W.; Brown, W.A. *Catal. Lett.* **2003**, 88, 39.

145. Mukerji, R.J.; Bolina, A.S.; Bown, W.A. *Surf. Sci.* **2003**, 527, 198.

146. McCabe, R.W.; Schmidt, L.D. *Surf. Sci.* **1977**, 66,101.

147. Ramachandran, A.S.; Anderson, S.L.; Dayte, A.K. *Ultramicroscopy* **1993**, 51, 282.

148. Lee, W.H.; Vanloon, K.R.; Petrova, V.; Woodhouse, J.B.; Loxton, C.M.; Masel, R.I. *J. Catal.* **1990**, 126, 658.

149. Shi, A-C.; Masel, R.I. *J. Catal.* **1989**, 120, 421.

150. Wang, T.; Lee, C.; Schmidt, L.D. *Surf. Sci.* **1985**, 163, 181.

151. Minors, J.H.; Gardner, P.; Woodruff, D.P. *Surf. Sci.* **2003**, 547, 355.

152. Greenler, R.G.; Burch, K.D.; Kretzschmar,K.; Klauser, R.; Bradshaw, A.M.; Hayden, B.E. *Surf. Sci.* **1985**, 152, 338.

153. Barth, R.; Pitchai, R; Anderson, R.L.; Verykios, X.E. *J. Catal.* **1989**, 116, 61.

154. De La Cruz, C.; Sheppard, N. *Spectrochimica Acta* **1994**, 50A, 271.

155. Fox, S.G.; Browne, V.M.; Hollins, P. *J. Elect. Spec. Rel. Phen.* **1990**, 54, 749.

156. Brandt, R.K.; Sorbello, R.S.; Greenler, R.G. *Surf. Sci.* **1992**, 271, 605.

157. Kappers, M.J.; Van Der Mass, J.H. *Catal. Lett.* **1991**, 10, 365.

158. Brandt, R.K.; Hughes, M.R.; Bourget, L.P.; Truszkowska, K.; Greenler, R.G. *Surf. Sci.* **1993**, 286, 15.

159. Eischens, R.P.; Francis, S.A.; Pliskin, W.A. *J. Phys. Chem.* **1956**, 60, 194.

160. Hammaker, R.M.; Francis, S.A.; Eischens, R.P. *Spectrochimica Acta* **1965**, 21, 1295.

161. Martin, R.; Gardner, P.; Bradshaw, A.M. *Surf. Sci.* **1995**, 342, 69.

162. Wang, P.; Slichter, C.P.; Sinfelt, J.H. *J. Phys. Chem.* **1985**, 89, 3606.

163. Beebe, T.P.; Yates, J.T. *J. Phys. Chem.* **1987**, 91, 254.

164. Chesters, M.A.; De La Cruz, C.; Gardner, P.; McCash, E.M.; Prentice, J.D.; Sheppard, N. *J. Elect. Spec. Rel. Phen.* **1990**, 54, 739.

165. Paul, D. K.; Beebe, T.P.; Uram, K.J.; Yates, J.T. *J. Am. Chem. Soc.* **1992**, 114, 1949.

166. Gumhalter, B.; Hermann, K.; Wandelt, K. *Vacuum* **1990**, 41, 1.

167. Ribeiro, F. H.; Schach Von Wittenau, A.E.; Bartholomew, C. H.; Somorjai, G.A., *Catal. Rev.* **1997**, 39, 49.

168. Wootsch, A.; Descorme, C.; Rousselet, S.; Duprez, D.; Templier, C. *Appl. Surf. Sci.* **2006**, 253, 1310.

169. Berlowitz, P. J.; Peden, C. H. F.; Goodman, D. W. *J. Phys. Chem.* **1988**, 92, 5213.

170. Cant, N. W. *J. Catal.* **1980**, 62, 173.

171. McCarthy, E.; Zahradnik, J.; Kuczynski, G.C.; Carberry, J. J. *J. Catal.* **1975**, 39, 29.

172. Akabuiro, E. C.; Verykios, X.E.; Lesnick, L. *Appl. Catal.* **1985**, 14, 215.

173. Atalik, B.; Under, D. *J. Catal.* **2006**, 241, 268.

174. Lundwall, M.; McClure, S.M.; Goodman, D.W. *in preparation,* **2010**.

175. Zhu, Y.; Schmidt, L.D. *Surf. Sci*. **1983**, 129, 107.

176. Freyer, N.; Kiskinova, M.; Pirug, G.; Bonzel, H. P. *Appl. Phys. A.* **1986**, 39, 209.

177. Engel, T.; Ertl, G. *Adv. Catal*. **1979**, 28, 1.

178. Hopstaken, M. J. P.; Niemantsverdriet, J. W. *J. Chem. Phys.* **2000**,113, 5457.

179. Nehasil, V.; Stará, I.; Matolín, V. *Surf. Sci.* **1996**, 352, 305.

180. Szabó, A.; Henderson, M. A.; J. T. Yates Jr. *J. Chem. Phys.***1992**, 96, 6191.

181. Hendriksen, B.L.M.; Bobaru, S.C.; Frenken, J.W.M. *Surf. Sci*. **2004**, 552, 229.

182. Gao, F.; Cai, Y.; Gath, K.K.; Wang, Y.; Chen, M.S.; Guo, Q.L.; Goodman, D.W. *J. Phys. Chem. C*. **2009**, 113, 182.

183. Gustafson, J.; Westerstroem, R.; Mikkelsen, A.; Torrelles, X.; Balmes, O.; Bovet, N.; Andersen, J. N.; Baddeley, C. J.; Lundgren, E. *Phys. Rev. B.* **2008**, 78, 045423.

184. Carlsson, P.A.; Zhdanov, V. P.; Skoglundh, M. *Phys. Chem. Chem. Phys.* **2006**, 8, 2703.

185. Garin, F.; Aeiyach, S.; Legare, P.; Maire, G.; *J. Catal.* **1982**, 77, 323.

186. Davis, S.M.; Zaera, F.; Somorjai, G.A. *J. Am. Chem. Soc.* **1983**, 104, 7453.

187. Zaera, F.; Godbey, D.; Somorjai, G.A. *J. Catal.* **1986**, 101, 73.

188. Herz, R.K.; Gillespie, W.D.; Peterson, E.E.; Somorjai, G.A. *J. Catal.* **1981**, 67, 371.

189. Biberian, J.P.; Somorjai, G.A. *App. Surf. Sci.* **1979**, 2, 352.

190. Yang, M.; Somorjai, G.A. *J. Am. Chem. Soc.* **2004**, 126, 7698.

191. Yang, M.; Chou, K.C.; Somorjai, G.A. *J. Phys. Chem. B.* **2004**, 108, 14766.

192. Muller, J.M.; Gault, F.G. *J. Catal.* **1972**, 24, 361.

193. Joyner, R.W.; Lang, B.; Somorjai, G.A. *J. Catal*. **1972**, 27, 405.

194. Pansoy-Hjelvik, M.E.; Schnabel, P.; Hemminger, J.C. *J. Phys. Chem. B.* **2000**, 104, 6554.

195. Teplyakov, A.V.; Gurevich, A.B.; Garland, E.R.; Bent, B.E. *Langmuir* **1998**, 14, 1337.

196. Teplyakov, A.V.; Bent, B.E. *J. Phys. Chem. B.* **1997**, 101, 9052.

197. Abon, M.; Billy, J.; Bertolini, J.C.; Tardy, B. *Surf. Sci.* **1986**, 167, L187.

198. Abon, M.; Billy, J.; Bertolini, J.C.; Tardy, B. *Surf. Sci.* **1986**, 167, 1.

199. Rupprechter, G.; Hayek, K.; Hofmeister, H. *J. Catal.* **1998**, 173, 409.

200. Belton, D.N.; Schmeig, S.J. *Surf. Sci.* **1988**, 202, 238.

201. Matolín, V.; Mašek, K.; Elyakhloufi, M.H., Gillet, E., *J. Catal.* **1993**, 143, 492.

202. Andersson, S.; Frank, M.; Sandell, A.; Giertz, A.; Brena, B.; Brühwiler, P.A.; Mårtensson, N.; Libuda, J.; Baümer, M.; Freund, H. J. *J. Chem. Phys.* **1998**, 108, 2967.

203. Frank, M.; Andersson, S.; Libuda, J.; Stempel, S.; Sandell, A.; Brena, B.; Giertz, A.; Brühwiler, P.A.; Bäumer, M.; Mårtensson, N.; Freund, H.J. *Chem. Phys. Lett.* **1997**, 279, 92.

204. Matolín, V.; Elyakhloufi, M.H.; Mašek, K.; Gillet, E. *Catal. Lett.* **1993**, 21, 175.

205. Labich, S.; Kohl, A.; Taglauer, E.; Knözinger, H. *J. Chem. Phys.* **1998**, 109, 2052.

206. Kohl, A.; Labich, S.; Taglauer, E.; Knözinger, H. *Surf. Sci.* **2000**, 454, 974.

207. Labich, S.; Taglauer, E.; Knözinger, H. *Topics in Catal.* **2001**, 14, 153.

208. Óvári, L.; Kiss, J. *App. Surf. Sci.* **2006**, 252, 8624.

209. Park, J.B.; Ratliff, J.S.; Ma, S.; Chen, D. A. *J. Phys. Chem. C.* **2007**, 111, 2165.

210. Dudin, P.; Barinov, A.; Gregoratti, L.; Scaini, D.; He, Y. B.; Over, H.; Kiskinova, M. *J. Phys. Chem. C.* **2008**, 112, 9040.

211. Zhang, Y.; Grass, M.E.; Kuhn, J.N.; Tao, F.; Habas, S.E.; Huang, W.; Yang, P.; Somorjai, G.A. *J. Am. Chem. Soc.* **2008**, 130, 5868.

212. Bowker, M.; Guo, Q.; Li, Y.; Joyner, R. W. *Catal. Lett.* **1993**, 18, 119.

213. Lundgren, E.; Gustafson, J.; Resta, A.; Weissenrieder, J.; Mikkelsen, A.; Andersen, J.N.; Köhler, L.; Kresse, G.; Klikovits, J.; Biederman, A.; Schmid, M.; Varga, P. *J. Elec. Spec. Rel. Phenom.* **2005**, 144, 367.

214. Jones, I.Z.; Bennett, R.A.; Bowker, M. *Surf. Sci*. **1999**, 439, 235.

215. Miners, J. H.; Cerasari, S.; Efstathiou, V.; Kim, M.; Woodruff, D. P. *J. Chem. Phys*. **2002**, 117, 885.

216. Schwartz, S.B.; Schmidt, L.D.; Fisher, G.B. *J. Phys. Chem*. **1986**, 90, 6194.

217. Leung, L-W.H.; Goodman, D.W. *Catal. Lett*. **1990**, 5, 353.

218. Linke, R.; Curulla, D.; Hopstaken, M. J. P.; Niemantsverdriet, J. W. *J. Chem. Phys.* **2001**, 115, 8209.

219. Rebholz, M.; Prins, R.; Kruse, N. *Surf. Sci. Lett.* **1991**, 259, L797.

220. Trautmann, S.; Baerns, M. *J. Catal.***1994**, 150, 335.

221. Fiorin, V.; McCoustra, M.R.S.; Chesters. M.A. *J. Phys. Chem. B.* **2003**, 107, 7058.

222. Nakamura, I.; Kobayashi, Y.; Hamada, H.; Fujitani, T. *Surf. Sci.* **2006**, 600, 3235.

223. Frank, M.; Kühnemuth, R.; Bäumer, M.; Freund, H.J. *Surf. Sci.* **2000**, 454, 968.

224. Frank, M.; Kühnemuth, R.; Bäumer, M.; Freund, H.J. *Surf. Sci.* **1999**, 427, 288.

225. Evans, J.; Hayden, B.; Mosselmans, F.; Murray, A. *Surf. Sci. Lett.* **1992**, 279, L159.

226. Anderson, J. A. *J. Chem Soc. Farad. Trans.* **1991**, 87, 3907.

227. Shanks, B. H.; Bailey, J. E *J. Catal.* **1988**, 110, 197.

228. Mittendorfer, F.; Seriani, N.; Dubay, O.; Kresse, G. *Phys. Rev. B.* **2007**, 76, 233413.

229. Nolte, P.;Stierle A.; Jin-Phillipp, N. Y.; Kasper, N.; Schulli, T. U.; Dosch, H. *Science* **2008**, 321, 1654.

230. Logan, A.D.; Sharoudi, K.; Datye, A.K. *J. Phys. Chem*. **1991**, 95, 5568.

231. Newton, M.A.; Dent, A.J.; Diaz-Moreno, S.; Fiddy, S.G.; Jyoti, B.; Evans, J. *Chem. Eur. J.* **2006**, 12, 1975.

232. Penner, S.; Bera, P.; Pedersen, S.; Ngo, L.T.; Harris, J.J.W.; Campbell, C. T., *J. Phys. Chem. B.* **2006**, 110, 24577.

233. Penner, S.; Wang, D.; Jenewein, B.; Gabasch, H.; Klötzer, B.; Knop-Gericke, A.; Schlögl, R.; Hayek, K. *J. Chem. Phys.* **2006**, 125, 094703.

234. Gabasch, H.; Knop-Gericke, A.; Schlögl, R.; Borasio, M.; Weilach, C.; Rupprecther, G.; Penner, S.; Jenewein, B.; Hayek, K.; Klötzer, B. *Phys. Chem. Chem. Phys.* **2007**, 9, 533.

235. Borchert, H.; Jürgens, B.; Zielasek, V.; Rupprechter, G.; Giorgio, S.; Henry, C.R.; Bäumer, M. *J. Catal.* **2007**, 247, 145.

236. McClure, S. M. ; Lundwall, M. J. ; Goodman, D.W. *Proc. Nat. Acad. Sci*. **2010**, submitted.

237. Bond, G.C.; Calhoun, J.; Hooper, A.D. *J. Chem. Soc., Faraday Trans.* **1996**, 92, 5117.

238. Yates Jr., J. T.; Duncan, T. M.; Worley, S. D.; Vaughn, R. W. *J. Chem. Phys.* **1979**, 70, 1219.

239. Solymosi, F.; Pásztor, M. *J. Phys. Chem.* **1985**, 89, 4789.

240. Solymosi, M.; Pásztor, M. *J. Catal.* **1987**, 104, 312.

241. Williams, K.J.; Boffa, A.B.; Lahtinen, J.; Salmeron, M.; Bell, A.T.; Somorjai, G.A. *Catal. Lett.* **1990**, 5, 385.

242. Williams, K.J.; Boffa, A.B.; Salmeron, M.; Bell, A.T.; Somorjai, G.A. *Catal. Lett.* **1991**, 11, 77.

243. Hayden, B.E.; King, A.; Newton, M.A. *Surf. Sci.* **1997**, 397, 306.

VITA

Name:	Matthew James Lundwall
Contact Address:	Department of Chemistry Texas A&M University P.O. Box 30012 College Station, Texas 77842-4719
Email Address:	Matt.Lundwall@ConocoPhillips.com
Education:	Ph.D., Chemistry, Texas A&M University 2010
	B.S., Chemistry, State University of New York at Stony Brook 2005
Current Position:	ConocoPhillips Associate Scientist, Surface and Thermal Analysis Division